Doctoral Thesis

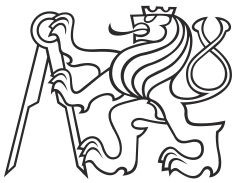

Czech Technical University in Prague

F3

Faculty of Electrical Engineering
Department of Cybernetics

Physics-Based Models for Robotic Soft Material Manipulation

Ing. Vladimír Petrík

Supervisor: Prof. Ing. Václav Hlaváč, CSc.
Supervisor–specialist: Ing. Vladimír Smutný, Ph.D.
Ph.D. programme: Electrical Engineering and Information Technology
Field of study: Artificial Intelligence and Biocybernetics
Prague, March 2018

Abstract

A robotic garment folding is studied in this thesis. A garment is a piece of soft material, which represents a rather wide class difficult to manipulate with a robot. The complexity lies in the high number of degrees of freedom of soft materials. Our objective is to obtain the accurately folded garment by designing a folding path according to a physics-based model.

A garment manipulation pipeline is described in the thesis beginning. The pipeline starts with an unknown garment located in a heap. It finishes with the folded garment. Different approaches for each task in the manipulation pipeline are surveyed. The thesis studies a single task from the pipeline in detail, i.e. the folding path generation. Existing approaches for the path generation are reviewed and their pros and cons are discussed.

We proposed three novel approaches for the folding path generation. The first proposed approach derives a circular path, which is an alternative to a state-of-the-art triangular path. We compared both approaches experimentally. The circular path outperformed the triangular path for real-life garments. The next two approaches employ more complicated physics-based models parametrized by the garment material properties. A model for one-dimensional strips is studied first. It is extended to more complicated shapes later. The path computation is based on the model states, which are in the static equilibrium. We demonstrated the accuracy of this approach experimentally while folding garments by a robot.

The proposed physics-based path generation methods require the material properties to be known. We proposed the estimation of the garment material properties during the folding. The estimation is formulated as an optimisation task. It is based on measurements of the garment shape provided by a laser range finder. The proposed algorithm improves the estimation iteratively and prevents the garment from slipping at the same time. We demonstrated the estimation procedure for garment strips of different materials.

Abstrakt

Tato práce studuje robotické skládání oblečení. Oblečení je z měkkého materiálu, který představuje poměrně širokou třídu obtížně manipulovatelnou robotem. Složitost spočívá ve vysokém počtu stupňů volnosti měkkých materiálů. Naším cílem je podle fyzikálního modelu navrhnout trajektorii pro robota tak, aby složené oblečení bylo geometricky dobře slícované.

Na začátku práce popisujeme sekvenci dovedností, které manipulují s oblečením. Sekvence začíná s neznámým kusem oblečení umístěným na hromadě a končí složeným oblečením. V práci popisujeme existující varianty jednotlivých dovedností. Jedna dovednost ze sekvence je studována víc do hloubky: generování trajektorie pro skládání oblečení. V práci ukazujeme existující přístupy pro generování trajektorie a diskutujeme jejich klady a zápory.

Navrhli jsme tři nové přístupy pro generování trajektorie pro skládání oblečení. První navrhovaný přístup odvozuje kruhovou trajektorii, která je alternativou k existující trojúhelníkové trajektorii. Experimentálně jsme porovnali oba přístupy a kruhová trajektorie překonala trojúhelníkovou pro reálné oblečení. Naše další dva přístupy používají složitější fyzikální modely, které jsou parametrizované vlastnostmi materiálu. Jeden je limitovaný na jednorozměrné proužky a druhý je jeho rozšířením pro složitější tvary. Generování trajektorie je založeno na výpočtu stavů modelů, které jsou ve statické rovnováze. Přesnost tohoto přístupu jsme experimentálně ověřili při skládání oblečení robotem.

Navrhované fyzikální metody generování trajektorie vyžadují, aby byly dopředu známé vlastnosti materiálu. V další částí práce jsme navrhli metodu pro odhad vlastností materiálu během procesu skládaní. Odhad je formulován jako optimalizační úloha, která je založena na tvaru látky měřeném laserovým dálkoměrem. Navrhovaný algoritmus iterativně upravuje odhad hodnoty parametru. Odhadování parametrů jsme demonstrovali pro různé materiály používané pro oblečení.

Acknowledgements

Foremost, I would like to express my sincere gratitude to my thesis supervisor prof. Václav Hlaváč for his support during my study and research and for his patience. Besides my supervisor, I would like to thank my two closest colleagues Vladimír Smutný and Pavel Krsek, who co-authored a majority of the research presented in this work. I would like to express my thanks to my colleagues at CMP with whom I had the pleasure of working with. Namely, I would like to thank Libor Wagner and Jakub Cmíral who assisted with the practical part of the experiments presented in the thesis. Furthermore, I would like to thank Jan Stria for his valuable advices and proofreading of my work.

I gratefully acknowledge projects FP7-288553 *CloPeMa* , the Technology Agency of the Czech Republic under Project TE01020197 Center Applied Cybernetics, the Grant Agency of the Czech Technical University in Prague, grant No. SGS15/203/OHK3/3T/13 and SGS18/205/OHK3/3T/37, RadioRoSo, part of project Echord++ [number FP7-ICT-601116], and the European Regional Development Fund under the project IMPACT (reg. no. CZ.02.1.01/0.0/0.0/15_003/0000468) for the financial support of my research.

Last but not least, I would like to thank my significant other Veronika for her support during my seemingly never ending work on my thesis.

Contents

Chapter 1

Introduction

With an increasing number of household robots available, there is a tendency to transfer human tasks to them. One of these tasks is a manipulation with soft materials. The examples of such materials are metallic wire, metal, kevlar or rubber sheet, fabric, or as in our case, garment. Humans manipulate soft materials intuitively while getting dressed, lacing their shoes, bending a piece of paper or folding a garment. However, these tasks remain challenging for robots. The difficulty lies in the high number of degrees of freedom the soft materials have. Several approaches were developed to solve this issue, and they are discussed in this thesis.

One particular soft-material-manipulation task is studied in detail in this thesis: a garment folding. The ability to fold a garment remains a challenging task due to various garment shapes and fabric materials. The folding consists of several independent folds performed in a sequence. In each fold, the robot grasps the garment at specific positions and follows a folding path. The folding path is not unique, and several approaches were proposed how to design it. The simplest approaches depend on the garment shape only. However, ignoring the material properties leads to an inaccurate fold. This inaccuracy increases with a number of folds and often results in a highly inaccurately folded garment. To increase the accuracy, the simulation of the garment can be used. The thesis shows the development of the folding path generation methods from the simplest purely-geometrical method, through simplified one-dimensional-physics-based method to the final shell-based solution.

1.1 Task Formulation

The robotic garment folding starts with a garment, which lies freely on a horizontal desk. The folding is specified by a folding line and grasping points (Fig. 1.1). The folding line represents the axis of symmetry for the start and final positions of the grasping points. The folding line is coincident with the folded state edge in a case of an infinitely flexible material. The goal of the robotic folding is to grasp the garment at the given points and follow the folding path. The examples of the grasping points and folding lines are shown in Fig. 1.1. Our goal is to design the folding path which results in an

expected folded state accurately and avoids the garment slipping on the desk at the same time.

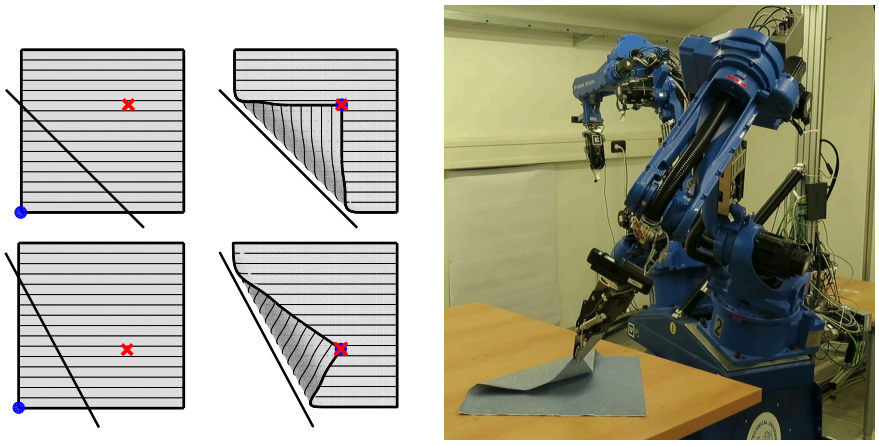

(a) Folding specification (b) Real folding

Figure 1.1: Different single arm folding scenarios for a square towel (a) and the real robotic folding (b). The start and the folded states are shown. Folding is specified by a folding line (black line) and by grasping points (blue circles). The final (red cross) and initial grasping points positions are symmetric with respect to the folding line.

1.2 Thesis Topic Selection, a Brief Personal Story

The interest of the *Center for Machine Perception* (*CMP*) group in the area of the soft material manipulation started with the project *Clothes Perception and Manipulation* (*CloPeMa*) in February 2012. The project was coordinated by *Centre for Research and Technology Hellas* from Thessaloniki. Four more institutions participated in the project: *Czech Technical University in Prague*, *University of Glasgow*, *Universita Degli Studi Di Genova*, and *Neovision s.r.o.*

The author of this thesis joined the *CloPeMa* project as a bachelor student in March 2012. He became amazed by the robotic technology and liked to combine it with his passion for algorithms and software development. He was also attracted by the challenge of designing a computer governing methods enabling operating robots in noisy, uncertain world. Researchers involved in *CloPeMa* project helped him a lot. They showed him both the beauty of the scientific endeavor and challenges hidden in engineering development. Let pick up from the longer list Vladimír Smutný, Pavel Krsek, and Václav Hlaváč.

The thesis author helped with the integration of the dual-arm robot designed in the project from commercial components (two Motoman 1400 industrial welding arms) into the Robotic Operating System. The entire dual-arm system enriched by cameras and other sensor is named *CloPeMa* testbed in this thesis.

He also helped with the calibration of the robot as described in the technical reports [Petrík and Smutný, 2014,Beneš et al., 2014,Šika et al., 2013]. Several small demos were implemented by the author for demonstration purposes (e.g. force compliance, garment/desk color segmentation demos). In the project life-time, the author implemented the robotic part of the state-of-the-art technique for the robotic garment folding and coauthored the paper [Stria et al., 2014]. While working on the project, we observed that the implemented technique does not fold the garment accurately enough. We decided to study the path generation method more thoroughly. By that time in January 2015, the *CloPeMa* project finished.

Although the *CloPeMa* project ends, we continue with our effort in the area of the garment folding. We designed several methods for the folding path generation and they are presented in this thesis. The *CloPeMa* robot was used in a new project *Radioactive Waste Robotic Sorter* which started in September 2016. Author contributed to the project by maintaining the software part of the robotic testbed.

1.3 Thesis Outline

Chapter 2 to 4 present the state-of-the-art in the domain related to the thesis. Chapter 5 to 9 present our original research in the robotic folding area. The thesis is concluded in Chapter 10.

Chapter 2 puts our folding path generation work into the wider scope of the garment manipulation pipeline. It reviews the state-of-the-art methods, which deal with the robotic garment manipulation. Chapter 3 shows existing methods for the folding path generation. Three methods were proposed in the literature: one geometrical method and two simulation based methods. The advantages and disadvantages of existing methods are discussed in the chapter. Chapter 4 reviews the methods for the physics-based garment simulation. This review is used later to choose an underlying physics-based model for the folding path generation method proposed by us.

The rest of the thesis describes the methods related to the path generation method which we proposed. Chapter 5 explains the purely geometrical path generation method. The proposed approach is compared experimentally with existing geometrical approach for the folding path generation. Chapter 6 introduces several relaxation techniques, which enlarge the folding working space and allow to fold the real size garments. Chapter 7 shows our physics-based method, which is limited to the narrow strip folding. The method is then generalized to the two-dimensional shapes in Chapter 8. The underlying physics of the methods is explained, and both cases (1D and 2D shapes) are experimentally verified. Chapter 9 describes the automatic estimation of the material properties of the physics-based models. The work described in this chapter allows the garment folding method to be fully autonomous and accurate at the same time.

1.4 Preview of the Scientific Contribution

The content of the thesis is based on material published in the following publications:

- Chapter 5 and Chapter 6:
  - Petrík, V., Smutný, V., Krsek, P., and Hlaváč, V. (2015). Robotic Garment Folding: Precision Improvement and Workspace Enlargement. In *Annu. Conf. Towards Autonomous Robotic Systems (TAROS)*, pages 204–215, Liverpool, United Kingdom.
- Chapter 7:
  - Petrík, V., Smutný, V., Krsek, P., and Hlaváč, V. (2016b). Physics-Based Model of Rectangular Garment for Robotic Folding. In *Proc. Int. Conf. on Intelligent Robots and Systems (IROS)*, pages 951–956, Daejeon, Korea,
  - Petrík, V., Smutný, V., Krsek, P., and Hlaváč, V. (2016a). Accuracy of Robotic Elastic Object Manipulation as a Function of Material Properties. In *Int. Workshop on Modelling and Simulation for Autonomous Systems (MESAS)*, pages 384–395, Rome, Italy.
- Chapter 8
  - Petrík, V., Smutný, V., Krsek, P., and Hlaváč, V. (2017). Single arm robotic garment folding path generation. *Advanced Robotics*, 31(24-24):1325–1337.
- Chapter 9
  - Petrík, V., Cmíral, J., Smutný, V., Krsek, P., and Hlaváč, V. (2018). Automatic Material Properties Estimation for the Physics-Based Robotic Garment Folding. In *Proc. Int. Conf. on Robotics and Automation (ICRA)*, Brisbane, Australia. (Accepted for publication).

1.4.1 Authorship

I hereby certify that the results presented in this thesis were achieved during my own research in cooperation with my thesis supervisor Václav Hlaváč, and in cooperation with Vladimír Smutný and Pavel Krsek. Furthermore, the results presented in Chapter 9 were achieved in cooperation with Jakub Cmíral.

1.4.2 Contributions to the Related Work

Chapter 2 puts the work of this thesis into the wider scope of the garment manipulation pipeline. The author of the thesis contributed to the following papers presented in Chapter 2:

- Stria, J., Průša, D., Hlaváč, V., Wagner, L., Petrík, V., Krsek, P., and Smutný, V. (2014). Garment perception and its folding using a dual-arm robot. In *Proc. Int. Conf. on Intelligent Robots and Systems (IROS)*, pages 61–67, Chicago, Illinois,
- Doumanoglou, A., Stria, J., Peleka, G., Mariolis, I., Petrík, V., Kargakos, A., Wagner, L., Hlaváč, V., Kim, T.-K., and Malassiotis, S. (2016). Folding Clothes Autonomously: A Complete Pipeline. *IEEE Transactions on Robotics*, 32(6):1461–1478,
- Stria, J., Petrík, V., and Hlaváč, V. (2017). Model-free Approach to Garments Unfolding Based on Detection of Folded Layers. In *Proc. Int. Conf. on Intelligent Robots and Systems (IROS)*, pages 3274–3280, Vancouver, Canada.

Chapter 2

Related Robotic Garment Manipulation Work

The variability of robotic tasks dealing with soft materials is large. For example, a robot can make a bed, do the laundry, put garments on hangers, etc. All these chores are worth solving, however, to specify boundary of the thesis, we limit our study to robotic garment folding.

2.1 Robotic Folding Pipeline

The ultimate goal of a *CloPeMa* -like robotic garment manipulation pipeline is to provide the folded garments stacked in one place. At the beginning of the pipeline, the garments are mixed in a heap. The garments are assumed to be dry. Such a starting scenario could be achieved by getting the garments out of the dryer using a robot. A single garment is isolated by a robot and manipulated until folded.

The earliest study in the robotic garment manipulation pipeline [Hamajima and Kakikura, 2000] split the pipeline into four tasks: (a) *isolating task*, (b) *unfolding and classification task*, (c) *folding task*, (d) *putting on specified place*. The paper [Hamajima and Kakikura, 2000] successfully solved *the isolating task* and fairly succeeded in solving *the unfolding and classification task*.

The whole pipeline was solved ten years later in work [Maitin-Shepard et al., 2010]. The authors used a PR2 robot (Fig. 2.1) to fold a single type of garment: towels. Their towel specialized approach was generalized to a wider range of garment types in works [Doumanoglou et al., 2016, Li et al., 2016b]. Both generalizations are able to fold various types of garments including a T-shirt, pants, or sweater. They follow the same pipeline as introduced by [Hamajima and Kakikura, 2000] with a small modification: *a flattening or ironing task* is added after *the unfolding task*. The modification ensures that the garment state satisfies the folding assumptions.

The works [Doumanoglou et al., 2016] and [Li et al., 2016b] differ in a way how the individual tasks of the pipeline are solved. Their solutions of the individual tasks are reviewed in the following sections together with other existing approaches. The *CloPeMa* folding pipeline is visualized in Fig. 2.2.

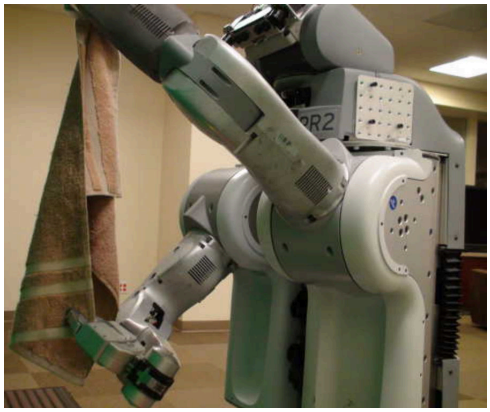

Figure 2.1: A PR2 robot unfolding a towel. Image is from [Maitin-Shepard et al., 2010]

(a) Isolating

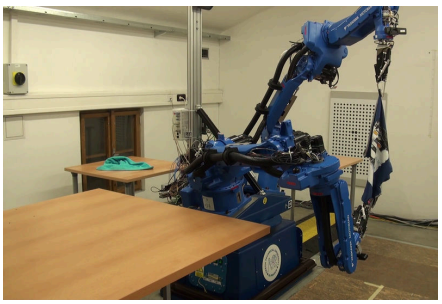

(b) Unfolding

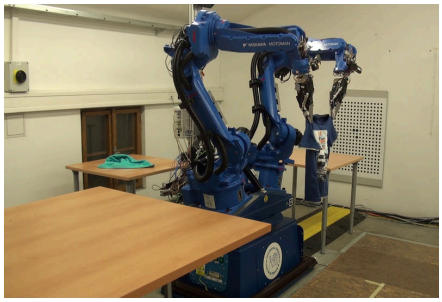

(c) Unfolded

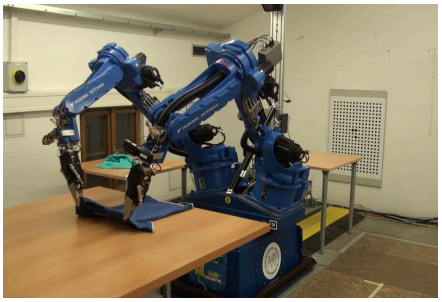

(d) Laying on table

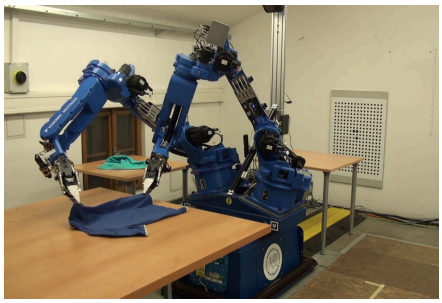

(e) Folding

(f) Folded

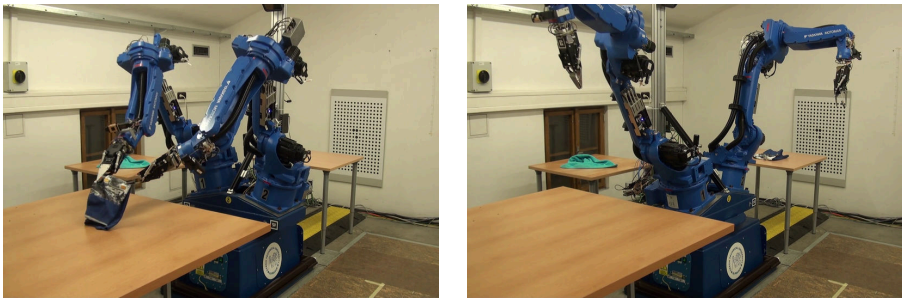

(g) Stacking (h) Stacked

Figure 2.2: The garment manipulation pipeline performed by a *CloPeMa* robot as described in [Doumanoglou et al., 2016]. The pipeline starts with a heap of garments. The robot isolates a single piece of garment and unfolds it in the air. The garment type recognition is done in the course of unfolding. The robot puts the garment on the table and performs the flattening which is however omitted in the visualization. The garment is then folded and stacked at the predefined location (another table in this case). The process continues iteratively until the last item from the heap is removed.

2.2 Single Garment Isolating Task

The isolating task separates a single piece of garment from the heap of garments. The garment is held by a robot gripper at the end of the task. There is no restriction on which part of the garment should be held by a gripper.

One of the first solutions [Hamajima and Kakikura, 2000] uses an RGB image to isolate a single garment. The authors used a recursive color segmentation. It is assumed that garments are distinguishable by color only and that the single garment has a unique color. The grasp point was selected to be in the middle of the largest obtained color region. The commonly used two-finger gripper is not capable of grasping the garments on an arbitrary location. For example, it will fail to grasp flat areas like the garment which lies spread on the table. To overcome this issue, the authors used a specially designed gripper to grasp the garment as visualised in Fig. 2.3. The gripper has a rotating wheel with tire mounted at the end of each finger. These rotating wheels take up the selected garment region between the fingers of the gripper.

Relaying on this special gripper is however limiting because it complicates the grasping for the other tasks in the pipeline (e.g. the folding). To overcome this limitation, other researchers combined the color and depth measurements to select an appropriate grasping point. For example, work [Ramisa et al., 2012] selects the highly wrinkled point. The authors proposed a *'wrinkledness'* measure, which prefers the easily graspable regions (e.g. pyramidal or conic structures). Another work [Maitin-Shepard et al., 2010] uses a discontinuity of depth measurement for the grasping point selection. The benchmark for the various grasping strategies was provided in work [Alenyà Ribas et al., 2012].

Figure 2.3: A schematic visualisation of the gripper designed to grasp the garment.

2.3 Unfolding and Classification

After the single garment isolating task is successfully performed, the robot holds a single piece of garment in the gripper. The isolating task makes no restriction on the grasped part of the garment. Thus the pose of the garment together with its type need to be recognized prior to the further manipulation.

A single garment type (a pullover) pose recognition [Kita and Kita, 2002] compares an RGB image of a real garment with a simulated model. The real garment is firstly segmented from the RGB image. The overlap between the segmented and simulated garment shapes is used to measure the similarity. The simulation utilizes the mass-spring model to compute the free hanging garment shapes for the different grasping points. The best match is used as a garment pose estimation. The work was extended [Kita et al., 2004] to provide 3D pose information about the grasping point for the second arm. Such information is necessary to unfold a garment by a dual-arm robot.

The recognition of the garment type and pose from a single view is difficult. Thus the classification is often performed in the course of unfolding or after the unfolding. The first unfolding approach [Osawa et al., 2007] does not require the garment type to be known in advance. However, in order to simplify visual tasks, the garments of unique colors and a clean background are assumed. The method is based on the corner detection algorithm. A dual-arm robot regrasps the garment until both grippers hold the garment corners. The garment type is recognized afterward based on the image matching technique. Similar approach is used for a towel unfolding [Maitin-Shepard et al., 2010]. The towel is regrasped until two corners of the same edge are held by a robot. The robot then untwists the gripper if necessary. The work was extended to handle various garment types in [Cusumano-Towner et al., 2011]. The method uses a hidden Markov model to estimate the pose and type through a specific sequence of actions and observations. The estimated values are used to bring the garment into the desired configuration.

In a series of works [Kita et al., 2009, Kita et al., 2010, Kita et al., 2011], Kita et al. use a reconstructed 3D point cloud and an animation software *Autodesk Maya* to evaluate the best match for the garment type and pose. The garment can be simulated inside the *Autodesk Maya* software. An active robotic manipulation was used to gain missing information for the underlying

simulated model. An appropriate robotic motion is selected automatically based on the measured data. The active manipulation terminates when the garment pose and type are recognized robustly.

The same animation software is used in work [Li et al., 2014]. The depth measurements and SIFT features computed from the simulation were used to train SVM classifier. Authors tested their pose and type recognition procedure on the real garments manipulated with a robot. The recognition procedure can be used for unfolding as demonstrated in [Li et al., 2015a]. The iterative regrasping is used to bring the garment into the desired unfolded configuration (Figs. 2.4 and 2.5).

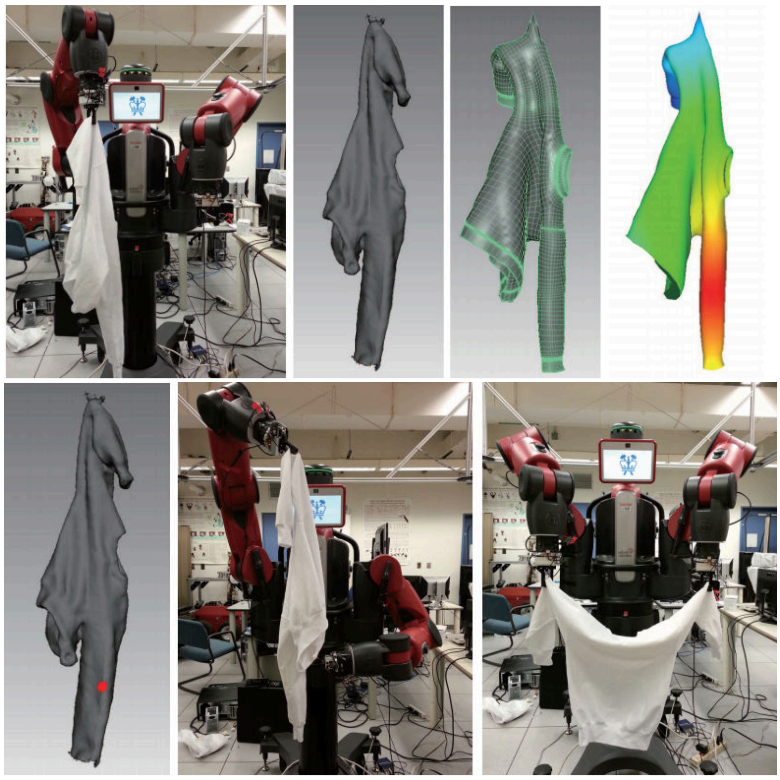

Figure 2.4: The unfolding of the hoodie with a baxter robot. The top row shows from left to right: the robot grasping the garment, reconstructed model, model matched in simulation, and the predicted mesh with Gaussian distribution distance. The bottom row shows from left to right: the predicted second grasping point, the regrasping step, and finally the unfolded garment. Images are from [Li et al., 2015a].

Another work on unfolding [Doumanoglou et al., 2014] uses a raw depth data and a random forest to recognize the type of a garment. Based on the type, the pair of grasping points is identified based on Hough forests. Grasping these points assures that the garment is unfolded by gravity naturally. The presented unfolding strategy requires a minimal number of robot movements in order to unfold the garment. The experimental results on the dual arm robot with a superior performance were shown in the paper.

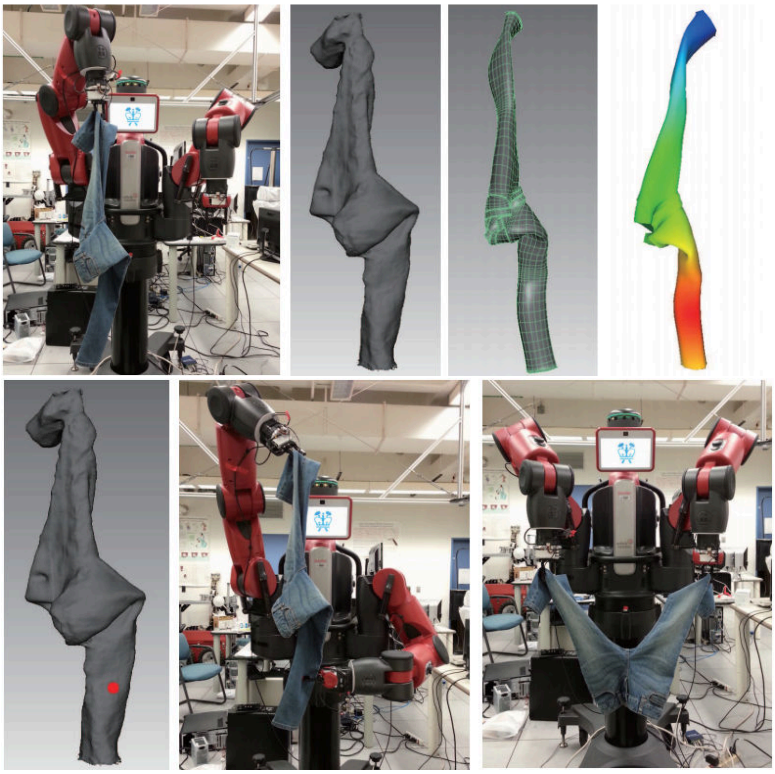

Figure 2.5: The unfolding of the jeans with a baxter robot. The top row shows from left to right: the robot grasping the garment, reconstructed model, model matched in simulation, and the predicted mesh with Gaussian distribution distance. The bottom row shows from left to right: the predicted second grasping point, the regrasping step, and finally the unfolded garment. Images are from [Li et al., 2015a].

Slightly different approach for unfolding was adopted in works [Yuba et al., 2015, Yuba et al., 2017]. Authors use two possible actions for the unfolding: a garment lifting and a pinch and slide motion. Robot selects the action automatically based on a partially observed Markov decision process. However, the method is presented for rectangular garments only.

Another approach [Triantafyllou et al., 2016] uses a support table desk for the unfolding. The garment is brought in an approximately planar configuration, where the garment is simply folded. This configuration is achieved by regrasping the garment in the air. After it is approximately planar, the garment is laid on the table. The template matching technique is utilized to detect the simply folded garment. The type recognition is determined in the course of the template matching. A robot lifts the garment afterward to bring it to its unfolded configuration.

The most recent work [Corona et al., 2017] uses the Convolutional Neural Network to identify the grasping points, which are used for the unfolding afterward. The network is trained both on real and simulated RGB images. The simulated images are rendered in *Autodesk Maya*.

Recently, there were attempts to perform classification task in advance of the unfolding. To simplify the classification task, an active manipulation is used in [Hu and Kita, 2015] to bring the garment into its limited shapes prior to classification. The limited shapes are characteristic poses of the garment obtained by predefined manipulation steps. After a few manipulation steps, there is a finite number of possible garment poses for the given garment type. Such an approach simplifies the final classification but relies on bringing the garment into its limited shape.

The more recent classification method [Sun et al., 2016a] uses the active manipulation too, but the method is iterative. The robot updates the garment pose until the confidence is sufficiently high. The method was integrated into the isolating task and was able to categorize highly wrinkled garments. The extension of this method [Sun et al., 2017] recognizes the category from a single shot in advance of the unfolding.

More comprehensive study on the visual grasp point localization, classification and state recognition was published in work [Jiménez, 2017].

2.4 Flattening and Ironing

The garment is held by two arms in an unfolded configuration after the unfolding task is performed. The robot puts the garment on the folding desk by pulling it over a table edge. Now, the garment lies on the table freely, and the robot grippers are empty. However, small wrinkles and partially folded parts could be present on the garment (Fig. 2.6). They need to be removed before the folding task to obtain the accurate folding result. This process is called flattening.

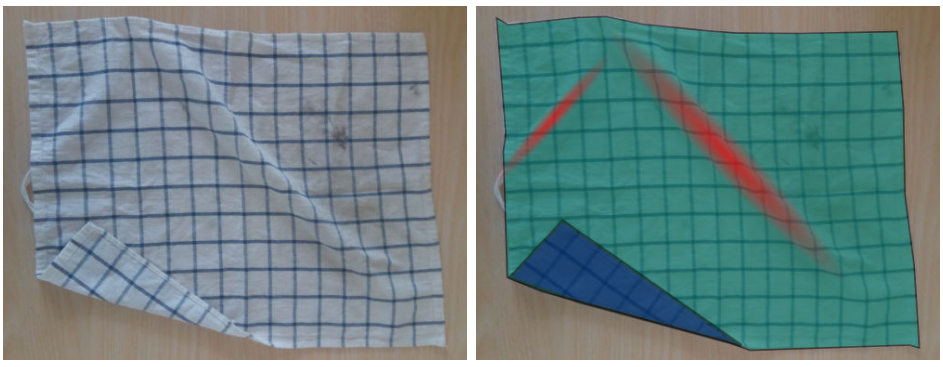

(a) Input image (b) Detected wrinkles and fold

Figure 2.6: The possible pose of the garment after it is laid by a robot on the table. Two phenomena are visible in the image (a): the wrinkles and the folded part of the garment. Image (b) shows the segmented garment in green color, two major wrinkles in red color, and the folded part of the garment in blue color. Both phenomena have to be removed prior to the folding task to obtain an accurate folding result.

Preliminary work on the flattening [Willimon et al., 2011] uses a single arm robot to pull the garment at various places on the outer boundary. The direction of pulling is computed to pull from the centroid of the garment. It removes the major wrinkles and authors considered a situation in which a part of the garment remains unfolded. The depth sensor is used to localize these unfolded parts, which are removed by a robotic arm afterward.

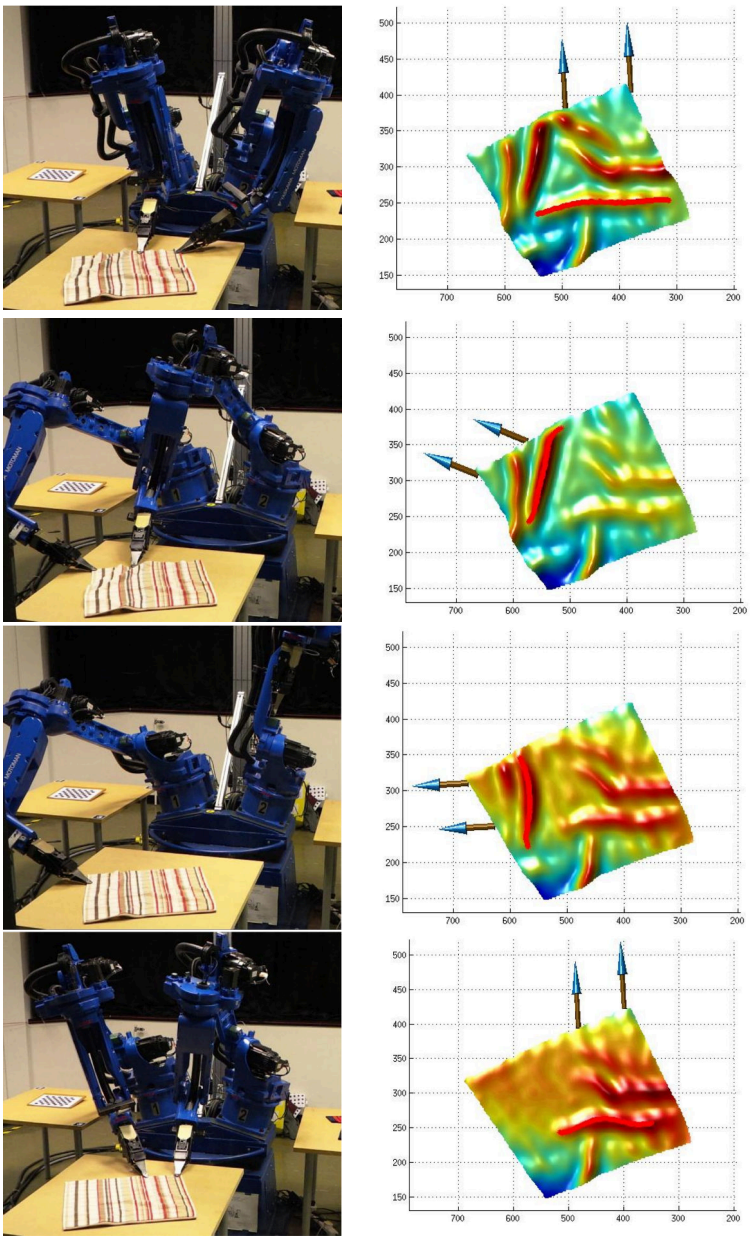

Figure 2.7: Flattening of a towel performed by *CloPeMa* robot. A real flattening (left) together with the reconstructed model and detected wrinkles (right) are shown. The arrows in the model suggest the direction of pulling for removing the largest wrinkle. In a third row, a single arm was used because following a dual arm path was not feasible. Images are from [Sun et al., 2015].

The wrinkles detection in a simulation [Sun et al., 2013] describes the detection of the largest wrinkle together with an estimation of the pulling force and its direction. The method operates on the 3D point cloud obtained from the simulation. The method itself is iterative. It is repeated until the garment is flat to the certain threshold. The same approach was used in a real robotic testbed in [Sun et al., 2015]. The largest wrinkle is detected on an accurate depth measurement obtained from a stereo reconstruction. Moreover, the method was extended to a dual arm robot, reducing the number of required iterations (Fig. 2.7).

Described methods perform flattening using the pulling operation only. The more advanced method [Li et al., 2016a] uses an iron to remove the wrinkles from a roughly flattened garment. The method estimates the regions which need to be pulled in prior of ironing and regions, which could be ironed directly. The ironing is then performed on the whole surface providing the flattened garment at the end.

Another method [Stria et al., 2017] focuses on the folded parts unfolding after the wrinkles were removed. The method does not use any garment model and performs the unfolding on the table iteratively. An RGB image and depth measurements from a Xtion sensor are combined to distinguish the top and the bottom layers of the folded garment. The task is formulated as a labeling problem and solved in an energy minimization framework. Two arms are then used to unfold the top layers: one arm performs the unfolding operation and the second arm holds the bottom layer to prevent the garment from slipping.

2.5 Folding

The folding task assumes that the garment is flattened and lies on the table freely. The garment type is already known from the unfolding and classification task. However, the pose of the garment is unknown.

The first method for the garment pose estimation [Miller et al., 2011] uses a parametrized skeletal model for every garment type. The optimization is performed to find the model and its parameters. The cost function of the optimization measures the distance from the model contour to a contour observed in an RGB image. The contour segmentation task is simplified by an assumption of the unique color background. The skeletal model which fits the best to the observation is used as the recognized type and the garment pose. With a known garment pose, a sequence of independent folds is planned as shown for a towel example in Fig. 2.8. The planned folds for other types of garments are shown in Fig. 2.9. This sequence is performed by a robot in an open loop manner as shown in work [Miller et al., 2012].

Instead of the open loop execution of the sequence of folds, the more robust version was proposed in [Stria et al., 2014]. Authors performed the garment pose detection after each fold. It improves the robustness since the garment can move on the folding surface during the robotic manipulation. Furthermore, a significant speed-up by a factor of several tens was achieved by using a

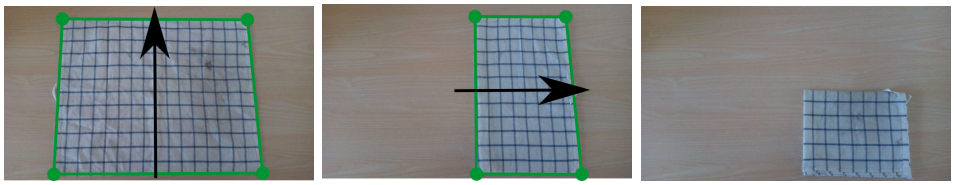

(a) First fold (b) Second fold (c) Result

Figure 2.8: The sequence of folds for a towel. The green polygon shows the fitted model. The oriented folding line (black) characterizes the individual folds.

polygonal model. The novel solution for the garment-table segmentation was also proposed in [Stria et al., 2014] in order to make garment folding possible on a regular table.

Each fold is characterized by a set of grasping points and an oriented line called the folding line. The folding line divides the garment into two parts. The successfully performed robotic fold ends with the one garment part placed on the top of the other part. In order to move the part of the garment, the robot grasps the garment at the grasping points and follows a folding path. The folding path is not unique and several approaches how to design it were proposed. Their analysis and design forms a core path of the thesis and are studied in the following chapters. The grasping points can be specified on the skeletal or polygonal model manually or automatically as described in [Miller et al., 2012]. The following theorem from work [Miller et al., 2012] is used: *A vertically hanging cloth polygon is immobilized when every convex vertex of the cloth at which the negative gravity vector does not point into the cloth polygon is fixed (i.e. be held by a gripper or be part of the baseline).* The theorem describes which parts of the garment need to be held by the grippers in order to keep the garment stable at a given configuration. The grasping points are assumed to be known in the rest of the thesis.

2.6 Putting on Specified Place

The garment putting on a specified place is a post-processing step. It is used to free the folding table and thus to prepare the testbed for the folding of the next garment. In our previous work, we have stacked the garments on a

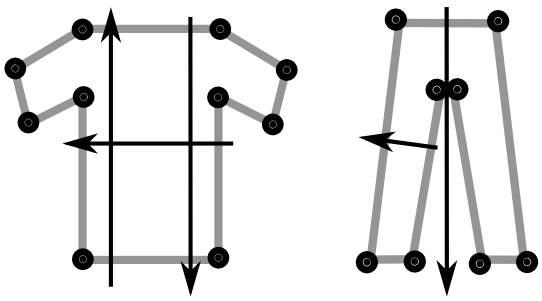

Figure 2.9: The planned folds for a t-shirt and pants.

separate table. Since the folding result is usually a rectangular shape, the stack is detected on the stacking table using an oriented bounding box fitting. Then, the robot moves the folded garment on the top of the stack.

2.7 Conclusion

A garment manipulation pipeline was briefly reviewed in this chapter. The first section divides the pipeline into individual tasks. The remaining part of the chapter reviewed various approaches how these tasks were solved in the literature. From all available tasks, we chose to study the folding path generation in more details. The next chapter reviews the existing approaches for the folding path generation. Chapter 5 to 8 present the folding path generation methods proposed by us.

Chapter 3

Related Folding Path Generation Methods

The previous chapter showed the pipeline which results in the folded garment at the end. It was demonstrated how the folding step is decomposed into the several independent folds. These folds are performed in a sequence resulting in the folded garment. In each fold, the robot grasps the garment and follows the folding path, which brings the garment into the desired state.

The existing approaches for the folding path generation could be split into two categories: purely geometrical algorithms and simulation-based algorithms. Both approaches are based on the underlying physics-based model. However, the model for geometrical path design is approximated in such a way that the resulting path depends on the garment shape only. The geometrical methods have an advantage of a low computation cost, but the result may be inaccurate due to the ignored material properties. The simulation-based methods are computationally more expensive and require the material properties to be known in advance, but the provided folding path results in an expected folded shape.

The beginning of this chapter formulates the folding path generation task and introduces the basic notations used in the rest of the thesis. The state-of-the-art path generation methods are describes afterward.

3.1 Formulation of the Folding Path Generation Task

It is assumed the garment pose and type was already recognized as described in Chapter 2. The set of the grasping points and the folding line is also assumed to be known. No other information about the garment is available. The goal is to design a path for the robotic grippers, which would result in the folded state as specified by the folding line. The formulation for the towel folding is visualized in Fig. 3.1.

The path describes the positions of the grasping points in time denoted as:

$$\boldsymbol{x}_g^i(\tau) = \left(x_g^i(\tau), \quad y_g^i(\tau), \quad z_g^i(\tau)\right)^\top , \qquad \tau \in (\tau_s, \tau_e\rangle \ , \tag{3.1}$$

where i represents the index of the grasping point, τ is a dimensionless monotonic function of time, and τ_s and τ_e represent the start and the end

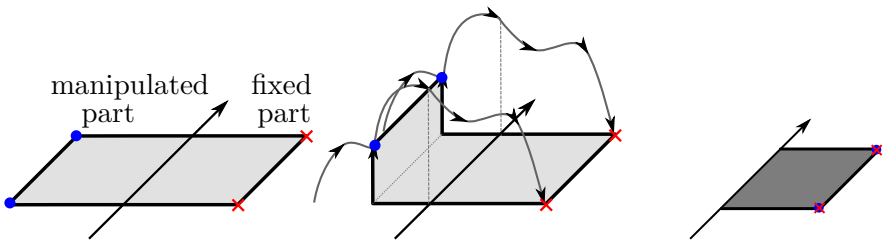

(a) Task specification (b) Folding path (c) Final state

Figure 3.1: The task formulation for the robotic folding path generation (a). The folding line (black line) and the grasping points (blue circles) are given. The folding line divides the garment into the manipulated and fixed part. The final grasping points positions (red cross) are computed from the given information. The goal is to design the folding path (b) whose following ensures the final state (c). In the final state, the grasping points coincide with the red crosses (final positions).

of the folding path, respectively. Note, that index i is omitted if there is a single grasping point. The positions $\boldsymbol{x}_g^i(\tau_s)$ and $\boldsymbol{x}_g^i(\tau_e)$ are symmetrical with respect to the folding line.

Let us denote the distance between the folding line and the point $\boldsymbol{x}_g^i(\tau_s)$ as d^i. Let assume without loss of generality that the grasping points are ordered in a descending order based on this distance, i.e. $d^1 \geq d^2 \geq \ldots$

All positions are specified with respect to a right-handed Cartesian coordinate system introduced in Fig. 3.2. The origin of the coordinate system lies in the intersection of the folding line and a line segment connecting the points: $\boldsymbol{x}_g^1(\tau_s)$ and $\boldsymbol{x}_g^1(\tau_e)$. The orientation of the coordinate system is determined as follow: The x-axis points towards the $\boldsymbol{x}_g^1(\tau_e)$, the y-axis coincides with the folding line, and the z-axis is perpendicular to the desk and points upward.

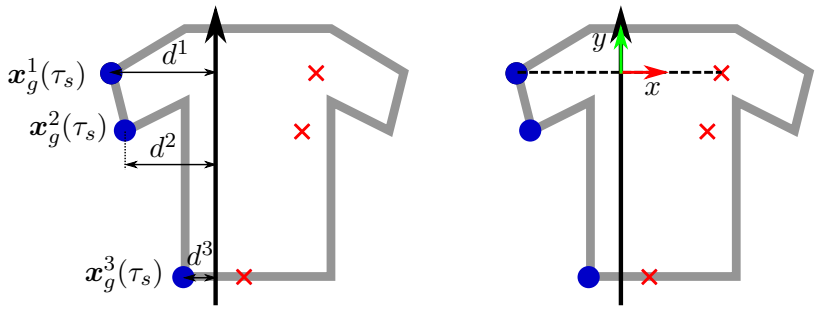

(a) Grasping points notation (b) Coordination system

Figure 3.2: The notation used for the grasping points (a) and the global coordinate system specification (b). The grasping points (blue circles) are ordered according to their initial distance to the folding line d^i. The coordinate system lies in the intersection of the folding line (black, solid) and the imaginary line (black, dashed) connecting the initial (blue circles) and final (red crosses) first grasping point positions.

The path generation is often divided into several phases. To distinguish them, we use symbols τ_{js} and τ_{je} for the start and the end of the *Phase j*, where j is the index of the phase. The phases are ordered in time, i.e. the folding path starts with *Phase 1*, is followed by *Phase 2*, etc. The following relations are assumed:

$$\tau_s = \tau_{1s} < \tau_{1e} = \tau_{2s} < \tau_{2e} = \ldots < \tau_{Ne} = \tau_e, \tag{3.2}$$

where N stands for the last phase.

3.2 Triangular Path

The first geometrical folding path generation method was presented in [van den Berg et al., 2010]. In the work of Berg et al. [van den Berg et al., 2010], the method is called *gravity based folding* since it relies on gravity. However, most of the methods presented in this thesis depends on gravity too. Thus, the path generated by [van den Berg et al., 2010] is called the *triangular path*.

3.2.1 Garment Model

The triangular path generation employs a polygonal garment model built on the following assumptions:

1. The garment is non-stretchable.
2. The garment has zero thickness.
3. The garment is subject to gravity.
4. The garment has no dynamics.
5. The garment has infinite friction with the surface on which it lies and with itself.
6. The garment has infinite flexibility.
7. If the garment is held by a number of grippers, and one or more grippers release the garment, no point of the garment will move upwards as a result of gravity and internal forces within the garment.

The first assumption uses an observation that the typical garments exhibit small to none extension when stretched by its own weight only. The garment is thus approximated by a non-stretchable model. Furthermore, one dimension (thickness) of the garment is significantly smaller than other two dimensions. The garment can be approximated by a zero-thickness model.

The garments behave dynamically in a real environment. However, in order to satisfy the fourth assumption, the robot can manipulate the garment slowly. With the slow robot motion, the effect of the garment dynamics is negligible.

The infinite friction was achieved by folding on a desk covered by a rough tablecloth in [van den Berg et al., 2010]. In subsequent sections, we analyze

the stability of the method when folding on a regular table where a garment can slip. Specially designed table should be avoided because of an intended usage of the folding robots. A household robot should be able to fold the garment on the table, which is commonly available in a household environment. Having a special table for every robotic task is undesirable.

The infinite flexibility assumption means that there is no energy stored in the bending, i.e. the garment does not resist to a bending deformation. The highly flexible garments represent only a subset of commonly used garments. On the other hand, this assumption allows us to use very simple model.

The last assumption of the triangular method is called the downward tendency assumption. According to [van den Berg et al., 2010], this assumption does not follow physics directly, but it matches the behavior of a reasonably shaped garment.

3.2.2 Folding path

During the motion, the state of the model can be divided into the vertical and horizontal part due to the infinite flexibility assumption (Fig. 3.3). The folding path is divided into two phases. In the first phase, the vertical part of the model is brought above the folding line. In the second phase, it is laid down on the fixed part of the garment. Both phases are shown in Fig. 3.3.

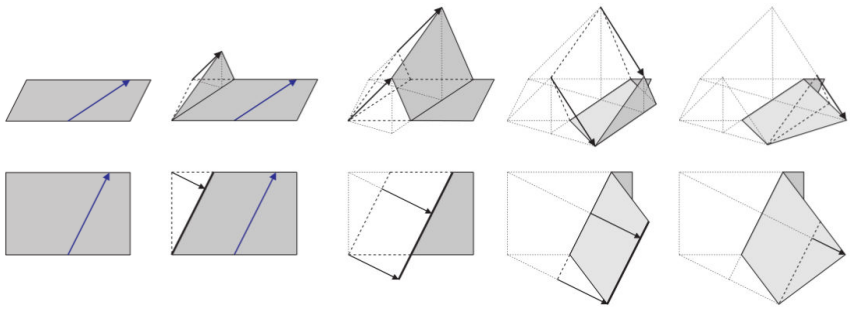

(a) Initial state (b) *Phase 1* (c) Phases boundary (d) *Phase 2* (e) End state

Figure 3.3: The triangular path visualization for a towel. The first row shows oblique view and the second row shows the top view. One fold performed by two grippers is shown. The state of the garment is separated into the vertical and horizontal part. The folding is divided into the two phases. At the end of the *Phase 1* the vertical part is above the folding line (blue line). At the end of the *Phase 2* the garment is folded. Images are from [van den Berg et al., 2010].

Phase 1

The robot lifts the garment in the first phase as visualized in Fig. 3.3. At the beginning of the *Phase 1*, only the first grasping point is being lifted (Fig. 3.3).

The i-th grasping point starts its motion at timestamp τ_{1s}^i computed as:

$$\tau_{1s}^i = \tau_{1e} - \frac{d^i}{d^1}\left(\tau_{1e} - \tau_{1s}\right). \tag{3.3}$$

The i-th grasping point ends its motion during the *Phase 2* at the timestamp:

$$\tau_{2e}^i = \tau_{2s} + \frac{d^i}{d^1}\left(\tau_{2e} - \tau_{2s}\right). \tag{3.4}$$

The timestamps with respect to the triangular path are visualised in Fig. 3.4.

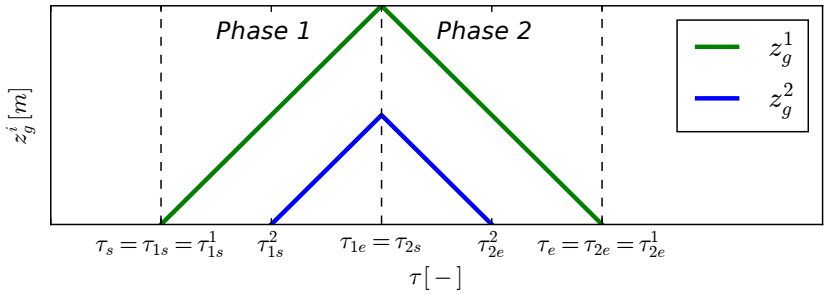

Figure 3.4: The visualization of the timestamps and the phases used for the triangular path computation. The individual phases are divided by black dashed lines. The triangular path shown here was computed for the towel folding scenario shown in Fig. 3.3. The span for the start and end of the folding is denoted $\langle \tau_s,\, \tau_e \rangle$, the span for the first phase is $\langle \tau_{1s},\, \tau_{1e} \rangle$ and for the second phase $\langle \tau_{2s},\, \tau_{2e} \rangle$. The start and end of the motion for the i-th grasping point is denoted $\left\langle \tau_{1s}^i,\, \tau_{2e}^i \right\rangle$, where subindex represents that motion starts in the first phase and ends in the second phase. The start and end of the motion are computed analytically from the initial distance between the grasping point and the folding line. The lines shown on the figure are parallel.

The position of the i-th grasping point in the *Phase 1* is:

$$\boldsymbol{x}_g^i(\tau) = \begin{cases} \boldsymbol{x}_g^i(\tau_{1s})\,, & \text{for } \tau \in \left\langle \tau_{1s},\, \tau_{1s}^i \right\rangle, \\ \boldsymbol{x}_g^i(\tau_{1s}) + \dfrac{\tau - \tau_{1s}^i}{\tau_{1e} - \tau_{1s}^i}\left(d^i,\quad 0,\quad d^i\right)^\top, & \text{for } \tau \in \left\langle \tau_{1s}^i,\, \tau_{1e} \right\rangle. \end{cases} \tag{3.5}$$

At the end of the *Phase 1*, the vertical part of the garment is above the folding line.

Phase 2

The robot puts the garment on the top of the fixed part in the *Phase 2*. The position of the i-th grasping point is computed as:

$$\boldsymbol{x}_g^i(\tau) = \begin{cases} \boldsymbol{x}_g^i(\tau_{2s}) + \dfrac{\tau - \tau_{2s}}{\tau_{2e}^i - \tau_{2s}}\left(d^i,\quad 0,\quad -d^i\right)^\top, & \text{for } \tau \in \left\langle \tau_{2s},\, \tau_{2e}^i \right\rangle, \\ \boldsymbol{x}_g^i(\tau_{2s}) + \left(d^i,\quad 0,\quad -d^i\right)^\top, & \text{for } \tau \in \left\langle \tau_{2e}^i,\, \tau_{2e} \right\rangle, \end{cases} \tag{3.6}$$

where $\boldsymbol{x}_g^i(\tau_{2s}) = \boldsymbol{x}_g^i(\tau_{1e})$ according to (3.2). The timestamp τ_{2e}^i represents the event after which the i-th grasping point remains static.

3.2.3 Triangular Path Assessment

The triangular path is optimal for the assumptions considered in Section 3.2.1 only. If the assumptions are met, the folding ends in the expected state as visualized in Fig. 3.5c. However, the real garments are neither infinitely flexible, nor there is infinite friction between the garment and the surface. As a consequence, the real garment folding with a triangular path can results in a state shown in Fig. 3.5d. It ends up slipped on the desk.

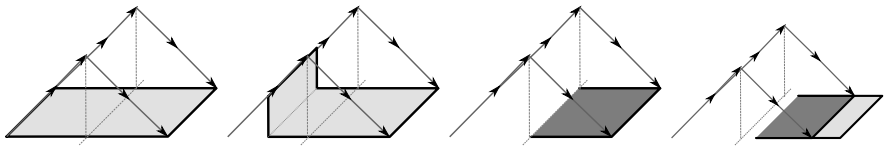

(a) Start state (b) Folding (c) Expected (d) Pushed

Figure 3.5: The triangular path based folding of the towel. One fold is shown, starting from the start state (a) and ending in the expected (c) or the pushed (d) state. The success of the folding depends mostly on the garment flexibility and the friction between the garment and the table surface.

Flexible garment, Finite friction. Firstly, let us consider the situation with a finite garment-table friction and an infinitely flexible garment. The flexible garment bends exactly as shown in Fig. 3.5b. There is no additional force acting in the direction of the gripper movement. The result would be the expected situation (Fig. 3.5c). The infinite friction assumption in case of the flexible garment is thus redundant.

Stiffer garment, Finite friction. In a case of the more realistic garment model, the triangular path folding results in different garment state as shown in Figs. 3.6 and 3.7. The garment is no longer infinitely flexible. Instead, there is a finite stiffness, which causes that the garment resists to bending deformation. This resistance results in a pushing force acting horizontally in x-axis direction.

At the beginning of the folding, the pushing force can result into two artifacts: (a) the garment slips on the desk in case the pushing force is larger than the frictional force, or (b) the wrinkle is created to cope with the force. The situation is visualised in Fig. 3.6.

At some point of the folding, the upper layer of the garment touches the lower layer Fig. 3.7. If the garment is not infinitely flexible, the touchdown point location is closer to the start state than desired. Again, the following situations could be distinguished: (a) the garment will slip on the desk; or (b) the upper layer will slide on the bottom layer, or (c) the upper layer will stretch, or (d) the layers will wrinkle, or (e) the combination of all cases

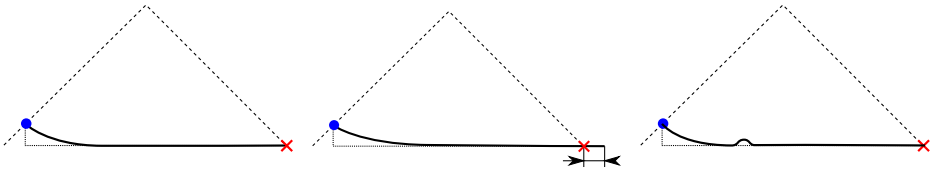

(a) Folding (b) Slippage (c) Wrinkle

Figure 3.6: The beginning of the stiffer garment folding with the triangular path (a). The cut in the plane $y = 0$ is shown for the towel folding scenario (Fig. 3.5). The dotted line represents the model of an infinitely flexible garment. The garment resistance to bend can result in the garment slipping (b) or in the wrinkle development (c).

above. While folding on a regular table, we observed the situation (a) is the most common. It results in the pushed garment state as shown in Fig. 3.5d.

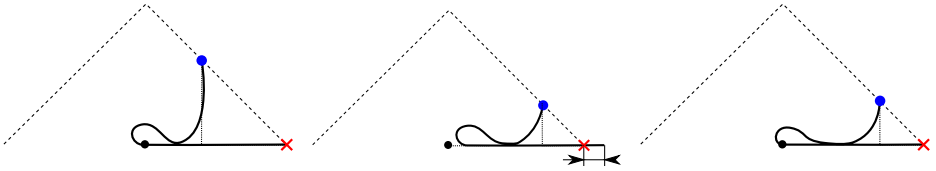

(a) Layers touching (b) Slipping (c) Sliding

Figure 3.7: The folding of the garment after the upper layer touches the lower layer in case of the triangular path. The figure (a) shows the garment state in which the layers touch each other for the first time. The black dot shows the position of the folding line. Following the triangular path after this point can result for example in: (b) the garment slipping on the desk or (c) the upper layer sliding on the bottom layer. Only in the last case, the folding would be accurate. However, predicting the outcome in presence of the friction is a difficult problem.

3.3 Dynamic Folding

The simulation-based path generation methods rely on the underlying garment model parametrized by a set of properties. The examples of this properties are bending stiffness, elasticity, friction between garment parts, etc. Different garment simulation methods employ different properties. The first simulation-based folding path generation was proposed by Yamakawa et al. in series of works [Yamakawa et al., 2010, Yamakawa et al., 2011a, Yamakawa et al., 2011b]. The authors proposed a strategy for dynamic garment folding in the air as shown in Fig. 3.8. The method requires a high-speed robot and a real-time control system.

The garment is modeled as a two-dimensional multi-link model. Individual links are inextensible and are connected by spherical joints. Such assumption results in a model described by algebraic equations. The garment model does not include the dynamical terms directly. Instead, they are approximated by

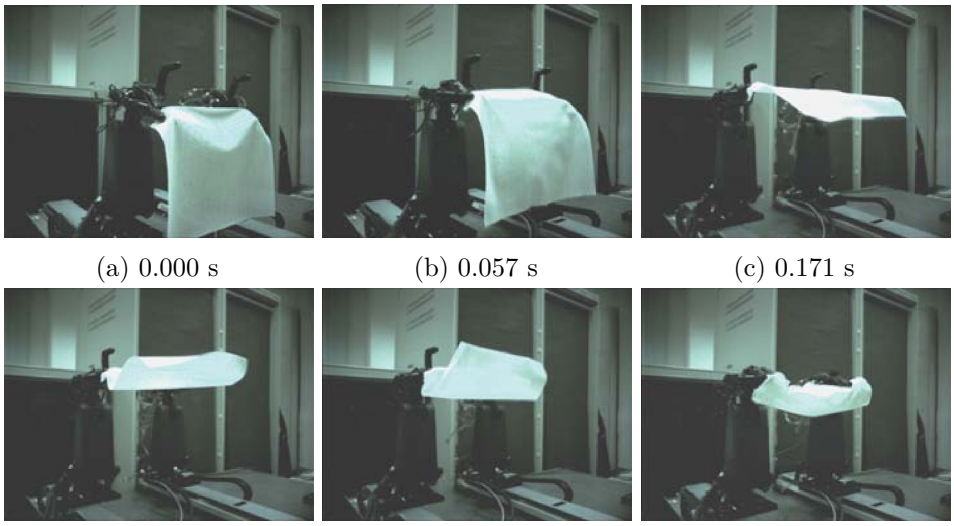

(a) 0.000 s (b) 0.057 s (c) 0.171 s

(d) 0.228 s (e) 0.285 s (f) 0.400 s

Figure 3.8: Dynamic towel folding visualization. The subcaptions shows the time from the start of the folding. The whole folding was completed in 0.4 s. Images are from [Yamakawa et al., 2011b].

a single parameter - a normalized time delay. The time delay describes the propagation of the movement in the garment model. The value of the time delay varies for different garments. In the experimental section, the authors estimated the time delay for the given garment.

Two robotic arms were used for the folding. Even the model can describe various shapes, the experiments and planning were performed for rectangular garments only. Moreover, the motion of both arms was assumed to be equal. Based on these assumptions, authors planned a trajectory, which in simulation results in the motion visualized in Fig. 3.8. The same trajectory was then used for real garment folding. Furthermore, the time at which the moving part of the garment should be grasped was computed from the simulation.

A dynamic towel folding experiments were performed in [Yamakawa et al., 2011b]. The authors report 100 % success rate of the garment deformation which results in the folded shape. However, the success rate of grasping predicted by the simulation was 30 % only. Authors proposed to use visual feedback in order to increase the overall success rate.

The folding described by Yamakawa et al. differs from our task formulation because it folds the garment in the air dynamically. The practical implementation of the method is also difficult because the method relies on a high-speed robot. The following section shows a method, which is closer to our formulation.

3.4 Predictive Simulation and Trajectory Optimization

Another folding procedure [Li et al., 2015b] follows the folding formulation introduced in Chapter 1. Authors estimated the material properties and then performed the folding in a simulation virtually. The folding path was then perturbed until the virtual folding was accurate enough. The path was performed by a real robot afterward.

3.4.1 Garment Model

Li et al. used an animation software *Autodesk Maya* for the garment model simulation. The simulator represents the garment by a mass-spring network. This representation is called *nCloth* in the *Maya* simulator. The model consists of n particles connected by springs with a specific stiffness. The physics of such simulation is straightforward but according to [Bender et al., 2015] there are some significant drawbacks:

- The simulated garment behavior depends on the spring network structure.
- It can be difficult to tune the spring constants to get the real garment behavior.

On the other hand, the *nCloth* simulation is effective, thus often used in computer graphics or animation software. The simulation allows to set following material properties: *stretch and compression resistance*, *bend resistance*, *bend angle dropoff*, *shear resistance*, *restitution angle and tension*, *rigidity*, and *deform resistance*. Such properties allow simulating various effects including elasticity, hysteresis, or bending.

From all available properties, authors of [Li et al., 2015b] observed that the *shear resistance* affects the simulation in the most significant way. The other properties were fixed to its default values provided by *Maya* simulator. Only the *shear resistance* was adjusted to tune the simulated model. The following steps were used for tuning:

- One extremum of the garment is manually picked and hanged under the gravity.
- The total length of hanged garment is measured and denoted by symbol l_1.
- The garment is then laid on the table slowly. The total length of laying garment l_2 is measured.
- The shear resistance fraction is computed: $(l_1 - l_2)/l_2$.
- The *shear resistance* of the simulation is then tuned until the simulated shear resistance fraction is identical to the measured one.

In other words, the relative extension of the garment under its own weight was used for the *shear resistance* estimation.

The garment folding is performed on a desk. The friction between the garment and the desk surface influences the folding path too. Authors performed one more experiment to estimate the friction coefficient. One side of the table was lifted until the freely laid garment started to slide. The inclination angle of the table was measured at that moment. The simulated friction was set such that the minimum inclination angle required for the garment sliding was equal in the simulation and reality. Both properties were measured by the authors manually before the folding.

3.4.2 Folding Path

Li et al. represent the folding path by a Bézier curve [Bartels et al., 1987]:

$$\boldsymbol{x}_g^i(\tau) = \sum_{k=0}^{n} B_k^n(u)\, \boldsymbol{P}_k^i, \quad u = \frac{\tau - \tau_s}{\tau_e - \tau_s}, \quad \tau \in (\tau_s,\, \tau_e\rangle\ , \tag{3.7}$$

where $B_k^n(u)$ represents the Bernstein basis function, and $\boldsymbol{P}_k^i$ are Bézier curve control points for the i-th grasping point. Four control points per arm were used in [Li et al., 2015b]. The first and the last control points correspond to the known start and end position of the grasping point:

$$\boldsymbol{P}_0^i = \boldsymbol{x}_g^i(\tau_s), \quad \boldsymbol{P}_3^i = \boldsymbol{x}_g^i(\tau_e)\,. \tag{3.8}$$

The remaining two control points are optimized to provide path which folds the garment accurately. The optimization starts with an initial folding path. The garment is folded virtually using the given path. The cost is then computed and minimized by perturbing the control points position. The cost is computed as a weighted combination of the path length and the dissimilarity, which measures the difference between the desired and the obtained garment shape.

The orientations of the grippers are not considered in the simulation. The single point of the garment is following the planned path. In real folding, the authors approximated the single point grasping by a small garment area grasping. The planned path is shown in Fig. 3.9.

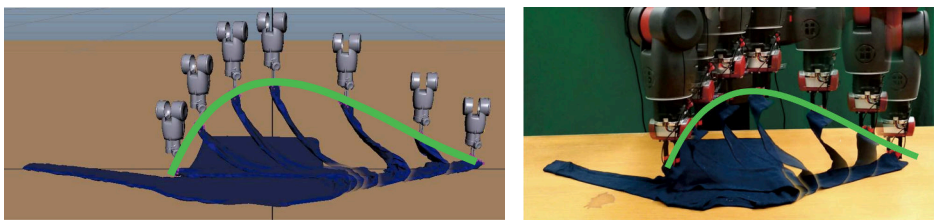

(a) Simulated folding (b) Real folding

Figure 3.9: The predictive simulation of the folding. The figure shows a planned path performed both, in simulation and real folding. A Baxter robot was used for robotic folding. Images are from [Li et al., 2015b].

This approach for the folding path generation was used to fold various garment materials. However, authors observed that the folding of the denim

material is less stable than other tested materials. It can be attributed to the fact that the shear resistance is relatively large for the denim and that bending resistance was not fine-tuned in the model. In our work, we employ different model of the garment which takes the bending resistance into account. The next chapter provides an overview of the physics-based garment simulation methods.

Chapter 4

Physics-Based Simulation of Garment Behavior

The simulation methods used by the path generation method shown in the previous chapter are fast to compute and often used in computer graphics. They provide visually plausible results but, on the other hand, the accuracy when compared to the real garment was not deeply studied. The overview of garment models for the computer graphics purposes was provided in [Baraff and Witkin, 1998, Bender et al., 2015]. More computationally expensive models were designed to provide more accurate results. They are based on physics-based modeling.

The physics-based simulation was studied on two scales [Dixit and Mali, 2013]:

- yarn scale,
- macromechanical scale.

The yarn-scale simulation studies individual fibers or yarns, of which the fabric is created. The yarn mechanical properties are considered together with an interaction between yarns. The interaction involves the contact modeling, the internal friction modeling, or the yarns connection pattern modeling.

The fabric is considered to be a continuous medium in the macromechanical scale. The garment simulation at the macromechanical scale is based on continuum mechanics, and individual yarns affect the mechanical properties of the fabric continua. Both scales are visualised in Fig. 4.1.

4.1 Yarn Models

Yarn-based simulation models the yarns of the fabric explicitly. Several models exist, each making different assumptions about the individual yarn properties. The first model was proposed in [Peirce, 1937], where the fabric was simulated purely geometrically. The yarns were considered to be infinitely flexible and inextensible with a circular cross-section. The model was used to simulate woven fabric. Because the geometric model in [Peirce, 1937] is too complex for the computation, the simpler model was proposed in [Kawabata et al., 1973]. Authors model the biaxial, uniaxial, and shear deformation

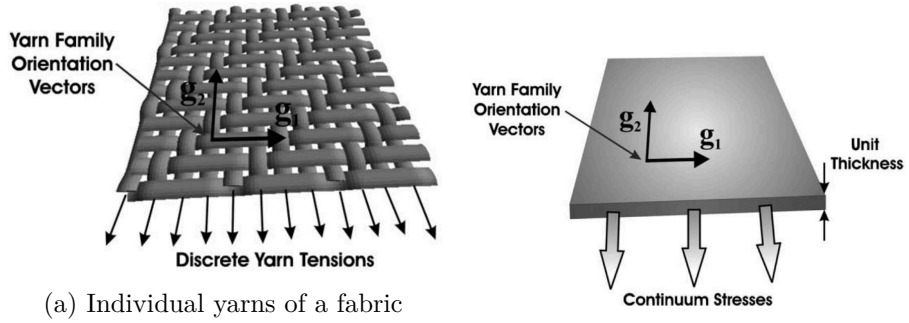

(a) Individual yarns of a fabric structure

(b) Macro-mechanical approximation

Figure 4.1: Fabric approximation as an anisotropic continuum. Vectors $\boldsymbol{g}_1$ and $\boldsymbol{g}_2$ represents *weft* and *warp* yarns directions. Images are from [King et al., 2005].

behaviors of fabrics based on pin-joined truss geometry. Both works [Peirce, 1937, Kawabata et al., 1973] considered plain weave fabric with persistent yarns contacts (no yarn slippage). The extension to non-plain weave fabrics was provided in work [Potluri et al., 2000].

The methods showed above considered the structure and geometry of the yarns pattern only. The more advance method [Zeng et al., 2006] was shown for plain weave fabric (*Kevlar*), where the inter-yarn friction was modeled. The individual yarns were modeled as cylindrical rods.

In series of papers [Kaldor et al., 2008, Kaldor et al., 2010, Kaldor, 2011], another yarn-scale simulation was proposed. The authors model the knitted garment behavior based on the individual yarns modeled as inextensible rods. The yarn-yarn contact was considered together with velocity filter for the friction approximation. The visual comparison of modeled and real knitted fabrics was conducted for various knitting patterns showing visually good match (Fig. 4.2).

The more efficient method for yarn-scale simulation was shown in [Cirio et al., 2014]. Authors implemented yarn-yarn contact, which is able to represent inter-yarn sliding efficiently. Simple force model was used to simulate friction and shear effects. The GPU parallel time integration was proposed to speed-up the simulation. The nonlinear fabric behavior was simulated, but the results were not compared with real fabric yet.

The yarn based simulation is physically accurate, but it is computationally expensive. Typical fabrics consist of many yarns per centimeter, which limits the simulation to small fabric samples only. To make it tractable, the simulation of the friction and contacts is often approximated, which affects the accuracy. Furthermore, estimation of the properties of individual yarns is a nontrivial task as well. These disadvantages lead to the lower scale simulation known as a macromechanic-based continuum simulation.

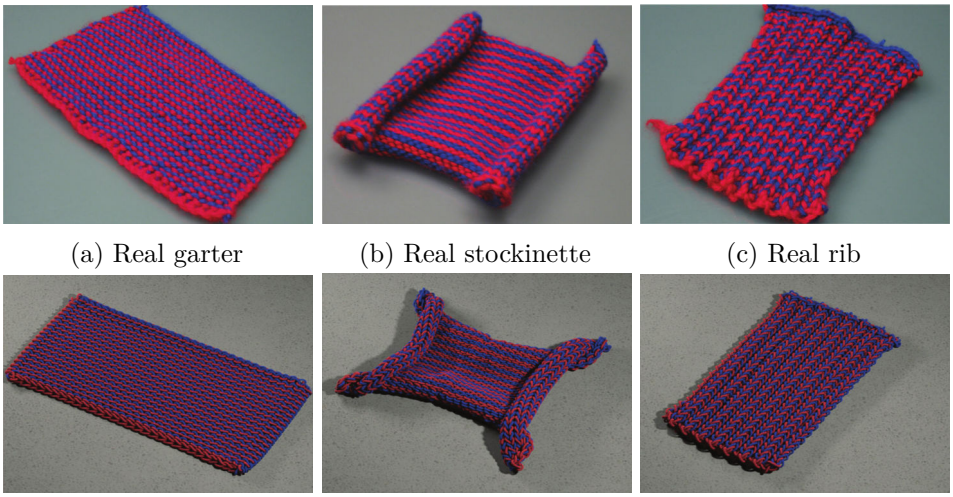

(a) Real garter (b) Real stockinette (c) Real rib

(d) Simulated garter (e) Simulated stockinette (f) Simulated rib

Figure 4.2: Visual comparison of the real (top) and simulated (bottom) knitted garments. A garter, stockinette, and rib patterns are compared. Images are from [Kaldor, 2011].

4.2 Macromechanical Models

The macromechanical model of fabric is a result of homogenization of the individual yarns. The fabric is modeled as a continuous medium with mechanical properties. Individual yarns and their interaction affect these properties, often resulting in a nonlinear relationship between macromechanical properties. For woven fabric, the undeformed yarns pattern is orthogonal and the orientations of the yarns are called *weft* and *warp* (Fig. 4.1).

The macromechanical properties of the fabric could be derived from yarns properties as shown in [King et al., 2005]. The yarn was assumed to be linearly elastic with linear bending resistance. The interactions of the yarns were modeled by a non-linear '*interference spring*'. Authors claimed, the approximation is sufficient since only a planar analysis was conducted. No yarn slippage was considered in the work. Based on these assumptions, the finite element model was derived. The developed model requires 24 constitutive properties to be defined. Many experiments were performed to show the validity of the model for the plain weave planar fabric modeling. The *Kevlar S706* material was used in the experiments. The model was then extended to account for yarn slippage in [Parsons et al., 2010] and in [Parsons et al., 2013]. All these methods were derived considering the yarns properties and their interactions. It led to complicated models, which consist of 24 properties at least. To reduce the number of required properties, several researchers used simpler model of the fabric continua and used shell elements for the garment behavior prediction.

In work [Collier et al., 1991], the nonlinear shell finite element method was used for a drape shape prediction of fabric. Authors compared an isotropic

and orthotropic linear elasticity and reported that the orthotropic is more appropriate for weaved fabric modeling. Another orthotropic linear elasticity model was proposed in series of works [Chen and Govindaraj, 1995, Chen and Govindaraj, 1996]. Authors used degenerated shell elements, where a 3D solid element degenerates into the shell surface element. A linear bending stiffness was assumed. Experiments indicated that the linear elastic model is an acceptable assumption for the fabric drape. However, the linear elasticity assumption is acceptable for a strain in a plane only. The linear bending stiffness, derived from continuum mechanics, is often invalid for fabrics due to its internal structure. A different bending stiffness model was studied in [Gan et al., 1995], where the bending stiffness was assumed to be independent of Young's moduli.

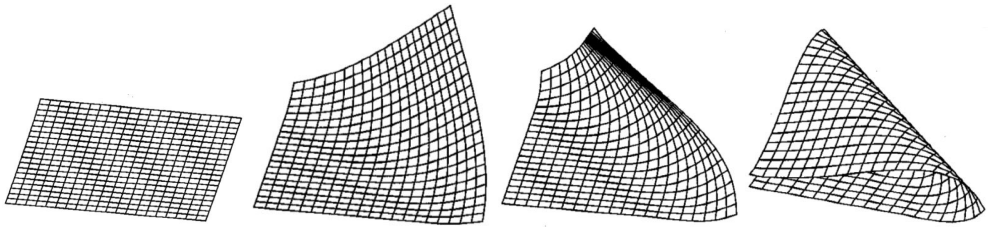

Figure 4.3: Diagonal folding of the rectangular garment described by a shell model. The folded shape was achieved by following a circular folding path. Images are from [Eischen et al., 1996].

Another shell formulation for fabric simulation was proposed in [Eischen et al., 1996]. Authors used shell theory and isotropic linear elasticity assumption. Nonlinear moment/curvature relationship with hysteresis was used in the simulation. Authors conducted experiments for manually folded fabrics. The resulting shape was compared with the prediction, and good agreement was found. The folding evolution is shown in Fig. 4.3.

Only a few of many existing approaches for fabric macromechanical simulation were mentioned in this section. The approaches differ in assumed model limitations. For example, several researchers studied non-orthotropic elasticity, hyperelasticity, or additional plasticity effects. A comprehensive reviews were done in works [Man, 2006, Williams, 2010, Dixit and Mali, 2013]. These reviews compare different fabric models approximations.

Chapter 5

Circular Path

Chapter 3 showed the state-of-the-art geometrical folding path, called the triangular path. It was demonstrated that the triangular path is not suitable for all garment materials. On the other hand, the simplicity of the geometrical path makes it easy to use. Thus we proposed another geometrical folding path as an alternative to the triangular path. The alternative is described at the beginning of this chapter, and both geometrical paths are compared experimentally afterwards.

5.1 Path Generation

We proposed the triangular path alternative in work [Petrík et al., 2015]. Instead of the infinite flexibility of the whole garment, the following simplified model is considered: It is assumed that the material itself is rigid and the flexibility is expected in the folding line only. Such assumption approximates some real-life garments satisfactory because:

- Multiple layers of the garment makes the garment stiffer.
- The periodical garment folding with the same folding line results into the internal garment structure deformation such that the folding line appeared to be flexible.

A circular folding path along the folding line is a natural consequence of the assumptions. The circular path preserves the constant distance between the grippers and the folding line. The planned circular path is shown in Fig. 5.1.

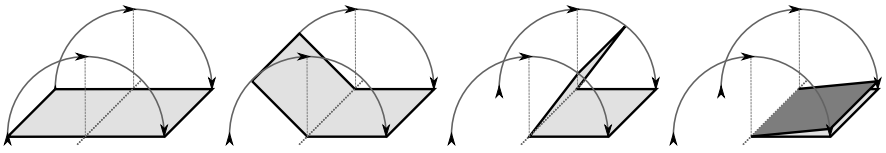

Figure 5.1: The circular folding path visualization. The simplified garment model, which assumes the rigid material with flexibility in the folding line only, is used.

The single phase is used for the circular path planning. The position of the i-th grasping point in the phase is computed as:

$$\boldsymbol{x}_g^i(\tau) = \boldsymbol{x}_g^i(\tau_s) + \left(d^i \cos\theta^i(\tau), \quad 0, \quad d^i \sin\theta^i(\tau)\right)^\top , \qquad \tau \in (\tau_s, \tau_e\rangle \ , \quad (5.1)$$

where

$$\theta^i(\tau) = \pi \left(1 - \frac{\tau - \tau_s}{\tau_e - \tau_s}\right) . \quad (5.2)$$

5.1.1 Path Assessment

The circular path has an advantage that the garment is not pushed during the folding. Therefore, the wrinkles are not developed during the folding too. On the other hand, the flexible garment has a tendency to bend under the gravity. It results in the force, pulling the garment towards the gripper position. Depending on the garment-table friction the garment will either slip or remains in the expected position. The visualization of the garment pulling is visualized in Fig. 5.2.

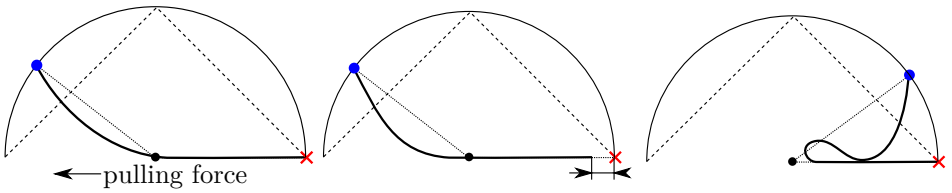

(a) Pulling (b) Slip (c) Layers touch

Figure 5.2: Circular path pulling force visualisation (a) together with the slipped state (b). The figure (c) shows the position of the first touch of the garment layers. The touch position is behind its expected position. The correction (layers sliding) is necessary to obtain an accurate result.

Another difference between triangular and circular path is the position of the first touch of the garment layers. In a case of circular path, the position of the touch is behind its expected position. The upper layer sliding on bottom layer is necessary to move the upper layer into its expected position.

5.1.2 Folding Path Boundaries

Both the infinitely flexible as well as the rigid materials are extreme models of the real world materials. The corresponding triangular and circular paths are thus limiting paths too. The folding path which folds the specific garment accurately lies mostly[1] in between these paths as shown in Fig. 5.3. The optimal path depends on the material properties, and it is studied in the following chapters. We observed that the upper bound path provides better folding results for tested real-life garments. In the experimental section, both paths are tested and compared in terms of the folding accuracy.

[1]The path can be above the circular path after the garment is lifted. It is the result of the real garment not being infinitely flexible in the folding line. The situation will be demonstrated in the following chapters.

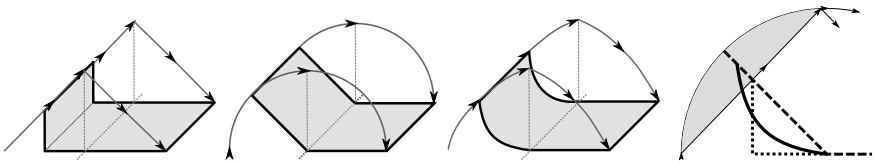

(a) Triangular (b) Circular (c) General (d) Side view

Figure 5.3: A general folding path bounded by triangular and circular path. The general folding path depends on the stiffness of the material. Figure (d) shows the paths state space (gray) for varying garment stiffness. The general garment state is visualized with a black solid curve, and the triangular and circular model state are shown dashed and dotted, respectively.

5.2 Trajectory from Path

The presented gravity based folding methods specify the grasping point positions unambiguously. On the other hand, the orientations of the grippers have not been discussed yet. In order to do that, we describe the robot and the grippers used to perform most of our experiments.

5.2.1 *CloPeMa* Robot

In our experiments, we mostly use the *CloPeMa* dual-arm robot [clo, 2015], which is shown in Fig. 5.4. The *CloPeMa* robot consists of two industrial welding robotic arms Yaskawa/Motoman MA1400 mounted on the rotating torso. Its grippers were specially designed for the garment manipulation [Thuy-Hong-Loan Le et al., 2013]. The grippers have a variable stiffness which facilitates the grasping of the garment from a non-deformable table. The grippers have two asymmetrical fingers. A thin finger is used to slide under the garment, while the second finger incorporates various sensors.

5.2.2 Grippers Orientation

The sliding capability of the grippers is used to grasp the garment from the desk before the folding path is followed. The grasping is shown in Fig. 5.5. The grasping of the garment limits the orientation of the gripper since the finger has to be aligned with the desk. For now, let us assume the gripper rotation around the desk normal is fixed such that gripper points towards the folding direction. This orientation is analyzed in a separate Chapter 6 later.

The orientation of the gripper while following the folding path is computed from the underlying garment model. The gripper finger is aligned with the model. In case of the triangular path, the grasped part of the model is vertical. Consequently, the orientation of the gripper is vertical too. For the circular path, the gripper points towards the folding line. In real robotic folding, the gripper needs to grasp the small part of the garment instead of the single point. An orientation of the gripper aligned with the garment

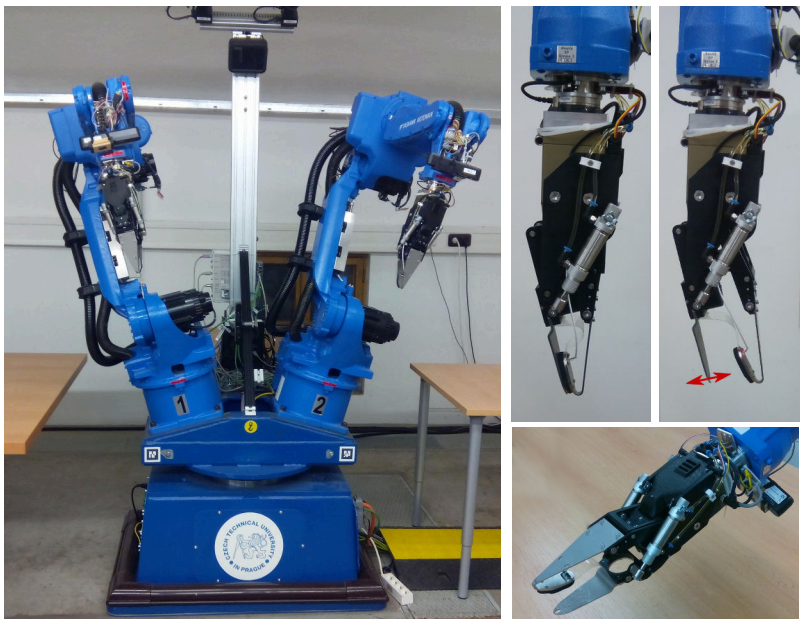

Figure 5.4: *CloPeMa* dual-arm robot with the grippers specially designed for the garment manipulation. The grippers are compliant in the direction shown in the top right figure. This compliance is used to reflect a small uncertainty in the table and the robot relative position.

model influences the garment state negligibly if the garment satisfy the model assumptions and if the grasping point is not held exactly at a single point.

5.2.3 Robot Trajectory

The path is represented in Cartesian coordinates by grasping points positions $\boldsymbol{x}_g^i(\tau)$ and corresponding grippers orientations $R^i(\tau)$. However, most of the robots are controlled in joint space. Inverse kinematics is used to transform the Cartesian coordinates into the joints positions. The inverse kinematics returns multiple robot configurations each satisfying the required Cartesian position. The collision-free configurations are selected to guarantee that configuration does not change for the whole folding path. It assures that the folding path is collision free and continuous in the joint space.

In the work [Petrík et al., 2015] we proposed the fold planning procedure operating in the joint space directly. It avoids the inverse kinematics computation and is generalizable to the redundant robot. However, the planning in joint space is slower than inverse kinematics computation for the *CloPeMa* robot. Thus, we use inverse kinematics for the experiments performed in this thesis.

The joint coordinates are sent to the robot controller at a specific time. The function τ is used to compute the timestamps of the path in joint space. The parameter τ parametrises the motion of the robot and is a nondecreasing function of time. Such a restriction assures the folding path is followed in a single direction. A linear function τ was used in our experiments assuring

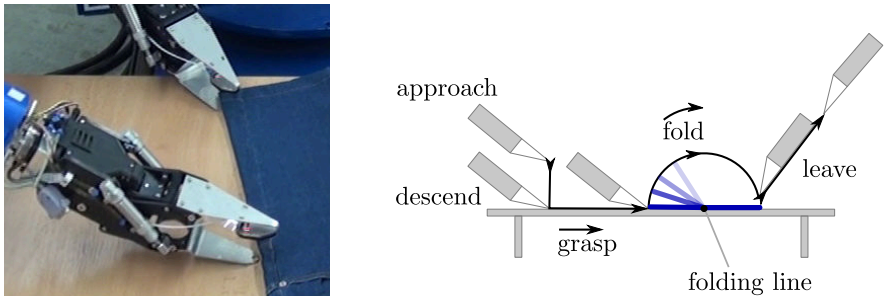

(a) Grasping (b) Folding steps

Figure 5.5: Grasping (a) and splitting the garment folding task into individual steps (b). The diagram (b) reads from its left side in time. The shown grippers (a) are in the middle of the grasping step (b). The grippers open after the approaching step and close when the grasping step finishes.

that the robot motion is slow to satisfy the garment model assumption, which neglects the dynamics of the garment.

5.3 Experiments

To compare the geometrical paths experimentally, we designed a folding path for two real-life garment types: jeans and dish-towel. The material used for both garments is relatively stiff. The folding line divides the garments into two equally sized parts as shown in Fig. 5.6. Thus, the garment edges of the bottom and upper layers should be aligned after the fold is performed. Due to the imprecise manipulation and the softness of the material, this is however, not true. The displacement of the non-grasped edge with respect to the expected grasping points position is measured as shown in Fig. 5.7. A melamine faced chipboard desk surface was used for all experiments.

(a) Jeans_1 (b) Jeans_2 (c) Dish-Towel

Figure 5.6: The garments used for the experiment shown in the start state. The folding line (black dashed line) divides the garments into two equally sized parts. The first and the second jeans differ in facing up or down only.

The results of the experiments for the tested garments are shown in Tab. 5.1. Each fold was performed five times. Based on these results, the circular folding

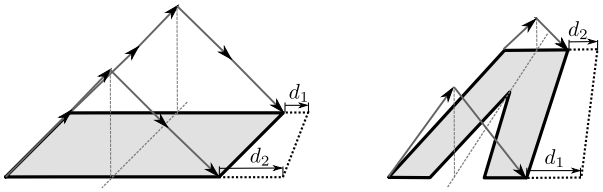

Figure 5.7: The measurement of the garment displacement after an inaccurate fold. The dotted line represents the garment pose after the fold is performed. The dotted line is not aligned with the starting garment pose due to the slipping of the garment. The displacements d_1 and d_2 are expected to be zero for the accurate fold.

outperformed the triangular one in terms of the accuracy. However, there are additional observations:

- The triangular path performs better for dish-towel than for the jeans. It is a consequence of fabrics used for the garments: the dish-towel is more flexible than jeans. The dish-towel properties better fit the triangular path garment model assumptions.
- For both paths, folding of the down-facing jeans performs worse than folding of the up-facing jeans. It might be attributed to the internal structure deformation caused by the periodic folding of the jeans in a single way. Thus, the down-facing jeans resists to the bending deformation more intensively.
- The circular path performs better for up-facing jeans than for the dish-towel. Again, it is because the jeans material is closer to the circular path garment model assumptions.

Based on these observations, we may expect that if we fold a soft towel then the triangular path will outperform the circular path.

	Triangular		Circular	
	mean	std	mean	std
Jeans_1 d_1	16.4	5.1	-1.8	1.8
Jeans_1 d_2	32.8	4.8	-0.8	1.8
Jeans_2 d_1	43.0	4.5	-19.0	5.6
Jeans_2 d_2	32.6	4.3	-6.0	0.7
Dish-Towel d_1	13.0	1.9	-3.6	3.4
Dish-Towel d_2	15.6	1.4	-10.4	2.2

Table 5.1: Displacement (in millimeters) of the garment after the fold is performed. The values are estimated from five folds per garment and per method. For jeans measurements, d_1 represents the leg opening offset and d_2 represents the waist offset (Fig. 5.7). Jeans_1 represent up facing jeans and Jeans_2 represent the down facing jeans (Fig. 5.6).

5.4 Conclusion

Two geometrical folding paths were compared in this chapter: the circular and triangular paths. It was shown, that both paths are suitable for different garment materials. We demonstrated that in the real robotic folding experiments. The pushing tendency of the triangular path and the pulling tendency of the circular path was predicted by the analysis as well as observed in the experiments. The accuracy of the folding is not satisfactory. Thus, we investigated better although more complicated models. They are described in the following chapters.

Chapter 6

Workspace Enlargement

This chapter analysis several techniques which are necessary to fold normal size garments with the *CloPeMa* robot. The techniques are used to enlarge the folding working space. The folding working space represents the positions where the folding task is feasible for a given robot. With multiple cooperating arms, the robot working space is rather limited. The limitation is caused by collisions, the kinematic constraints of joints, etc. An enlargement of the working space can be gained by relaxing the requirement of the fixed gripper orientation.

6.1 Relaxations

Azimuth relaxation. The first relaxation focuses on the grasping of the garment, which is performed in advance of the folding. The only grasping limitation is that the gripper lower finger must be aligned with the desk. The orientation of the gripper in the horizontal plane can be arbitrary within the interval limited by the garment contour as shown in Fig. 6.1a. This relaxation, named as the azimuth relaxation, is considered for the grasping phase only. During the fold, the relative orientation of the gripper and the held part of the garment has to be fixed not to crease the garment. Azimuth relaxation gives an additional degree of freedom per gripper.

Elevation relaxation. The orientation of the gripper can be relaxed along the folding path too. Instead of considering the fixed elevation angle (Fig. 6.1b), it could be relaxed slightly even for materials with low flexibility like jeans. The relaxation concerns the folding step only. For the grasping step, the elevation is determined by the allowed relative position of the table desk and the gripper.

With both relaxations considered, there are additional two degrees of freedom per arm in the fold planning task. The closed kinematic chain of the fold planning task for the *CloPeMa* robot is visualized in Fig. 6.2.

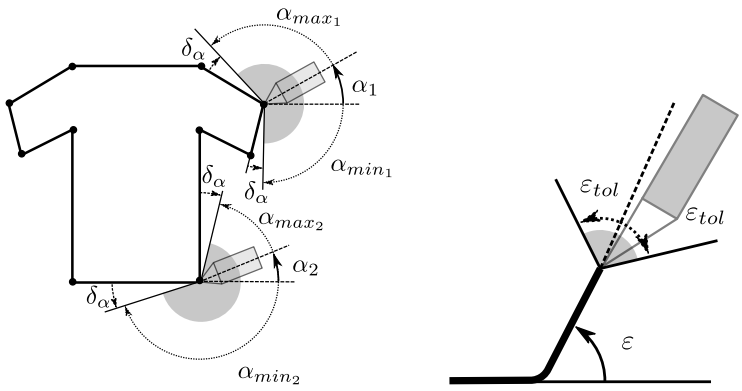

(a) Azimuth relaxation (b) Elevation relaxation

Figure 6.1: Gripper constraints relaxation. The left drawing shows the azimuth relaxation limited by the garment contour. The angular offset δ_α reflects the angular dimension of the gripper finger tip. The value is constant, and for the grippers mounted on the *CloPeMa* robot, it is set to 30°. The right drawing shows the elevation relaxation limited by constant angles which depend on the garment flexibility.

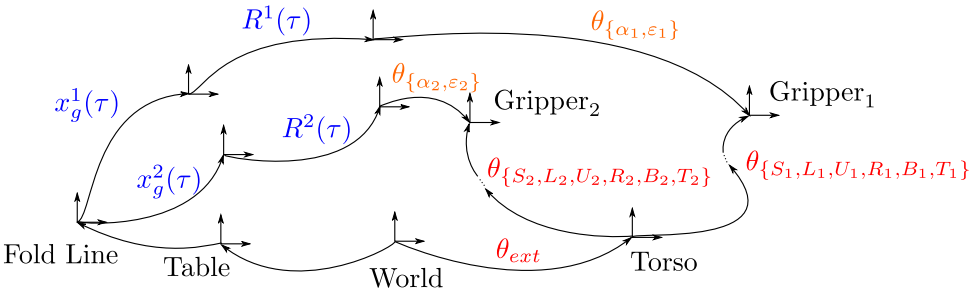

Figure 6.2: The closed kinematic chain of the *CloPeMa* robot for the fold planning task. Blue variables represent the position and parameters of the fold. They define a planning task. Red variables are individual joints of the robot. Orange color stands for the azimuth and elevation relaxations.

6.2 Workspace Enlargement Experiments

We performed a virtual experiment in order to quantify the workspace enlargement with the relaxed constraints. The relaxations together with all active joints being used for the planning should enlarge the working space of the robot. The towel folding scenario with varying towel position is simulated to examine the folding working space for the *CloPeMa* robot.

The multidimensional workspace hypervolume is difficult to evaluate numerically. For demonstration purposes, we have chosen to sample the working space along the x-axis while keeping other parameters constant. The scenario and the results are shown in Fig 6.3.

Three different cases were investigated, and in all cases, the elevation relaxation was enabled. The first case shows the working space for fixed torso axis and for relaxed azimuth constraint with limits visualized in Fig. 6.3a. In

the second case, the torso axis was relaxed, but the azimuth angle was fixed for both arms. Note, that the working space for the second case varies depending on the selected azimuth angles. From all the tested angles, we visualize the one producing the largest working space. The third case visualized the possible positions when all the relaxations were allowed (i.e. elevation, azimuth, torso).

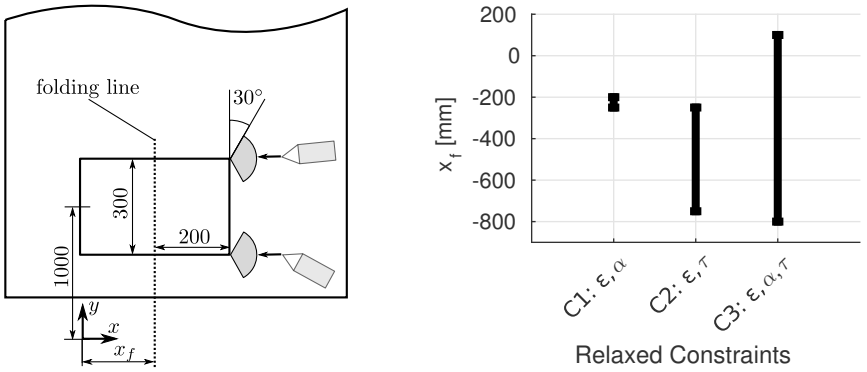

(a) Folding scenario (b) Succesfully planned fold positions

Figure 6.3: Workspace analysis experiment with the torso axis located in the origin (a). The dimensions used in the scenario are in millimeters. The fold was planned for varying garment position measured by the folding line position x_f. The range of x_f values was investigated under different relaxations (b). In the first case, the elevation and the azimuth were relaxed. In the second case, the elevation was relaxed and the torso motion was allowed. The last case considers the situation with all relaxations allowed.

Based on these results, it is clear that the space of possible towel locations is significantly larger when the relaxations are allowed. Asymmetrical results are caused by the fact that grasping and releasing positions of the gripper are not symmetrical. The reachable distance of the robot is thus larger in the direction of folding.

6.3 Conclusion

This chapter introduced several relaxations of the gripper orientation constraints, which result into the folding working place enlargement. These relaxations are necessary to fold the real sized garments with the *CloPeMa* robot. The introduced relaxations are not limited to the triangular or circular paths. They are used for the path planning in all methods presented in this thesis.

Chapter 7

Physics-Based Strip Folding Path

The state-of-the-art simulation-based folding path generation method [Li et al., 2015b] plan the optimal path by optimizing in the space of all possible paths. In our work [Petrík et al., 2016b], we performed optimization in the space of garment states only. To achieve that, we employ a physics-based model and find a static equilibrium in each state of the path. The boundary conditions are used to specify the folding constraints for each state individually. The underlying garment model and path generation method are described in this chapter.

The methods presented here are not restricted for analysing of the garment folding only. The model describes a wide range of materials, and it can be used in other fields as well. For example, similar model was used for the task of undersea pipes laying using the J-lay method [Wang et al., 2010] or for a pipeline installation and recovery in deepwater [Zeng et al., 2014].

7.1 Garment Model

We use macromechanical garment model to design a folding path for a garment. Our analysis starts with the simplifying assumptions:

1. The garment is rectangular.
2. The folding line is aligned with the garment edge.
3. Garment material is homogeneous and isotropic with constant bending stiffness.
4. Garment is thin with a constant thickness.
5. The dynamic effect of the garment motion is neglected.

The first two assumptions limit the possible folding scenarios significantly. On the other hand, they allow us to represents the garment as a one-dimensional string as shown in Fig. 7.1. The whole edge of the garment has to be grasped to be able to represent the garment as a string. However, our experiments show that replacement of the edge grasp by the two corner grasps does not decrease the folding accuracy for the regular towel. The one dimensional model of the real towel is shown in Fig. 7.2.

The third and fourth assumptions are used to derive equations for the garment model. The last assumption allows us to consider static equilibrium, which neglects the dynamics effect. The negligible dynamic effects are achieved by a slow robot motion during real folding.

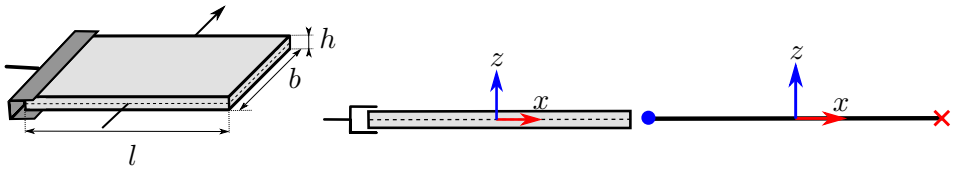

(a) 3D view (b) Side view (c) String representation

Figure 7.1: The rectangular garment with rectangular cross-section and dimensions l, b, and h. The folding line is shown in black (a). Consider slices of the garment which are perpendicular to the folding line. If the whole garment edge is grasped, then the shapes of the slices are equal. Thus, the shape of the garment can be deduced from the side view only (b). The thickness h of the garment is smaller than the length l. The state of the garment can be approximated by one dimensional string represented by a neutral axis (c). The neutral axis represents a middle surface of the garment, which is shown dashed in (a) and (b). The blue circle and red cross represents the start and final grasping point position.

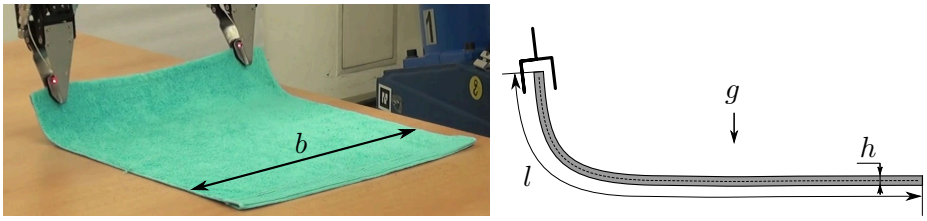

(a) Real towel folding (b) String representation of a towel

Figure 7.2: A one-dimensional representation of the garment. A towel, with dimensions l, b, and h, is grasped by two grippers of a robot (a). Its one-dimensional representation is shown in Fig. (b). Symbol g represents a gravitational acceleration and arrow shows the direction of the gravitational acceleration.

7.1.1 String Model

We start our model description with a derivation of equations, which describe the string model without contact. The contact modeling is considered in a separate Section 7.1.3 later.

Thin strings kinematics is described by *Euler-Bernoulli* beam theory [Timoshenko, 1953]. The theory assumes that the cross sections are not deformed and are perpendicular to the middle string. This assumption results in the strain changing linearly through the garment thickness. The model of the string is derived based on the equilibrium of forces acting on an element ds of the string. The element and the acting forces are shown in Fig. 7.3.

The following forces act on the string: A tension force $T(s)$ acting in a direction of a tangent to the string at the position s. A force perpendicular

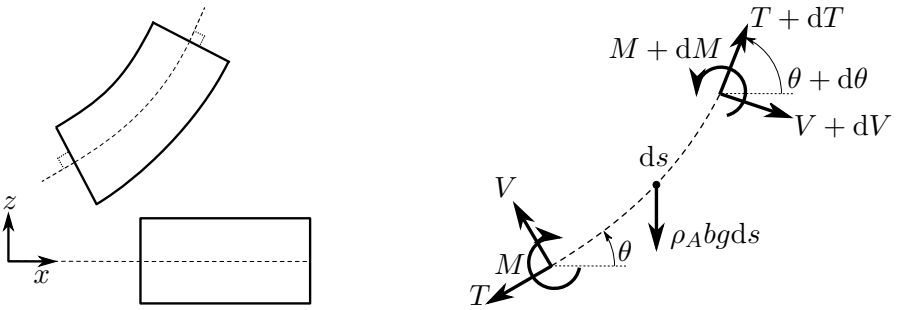

(a) Reference and deformed state (b) Forces acing on the element

Figure 7.3: The element of the string in a reference and deformed configuration (a). The cross-sections of the garment model remains straight and perpendicular to the neutral axis. The middle string length remains constant in the deformed configuration. One side of the garment is extended and the other is compressed. The strain changes linearly along the garment thickness. Figure (b) shows the forces acting on an infinitesimal element $\mathrm{d}s$. Symbol $T(s)$ represents tension force, $V(s)$ is shear force, $M(s)$ is moment, and $\theta(s)$ represents an angle between the tangent and the horizontal axis. The term $\rho_A\, b\, g\, \mathrm{d}s$ represents a gravitational force.

to tension force is called shear force and is denoted by symbol $V(s)$. The string bends under its own weight only. It results in a force $\rho_A\, b\, g\, \mathrm{d}s$, where b is the garment width, ρ_A stands for the material area density, and g is a gravitational acceleration. The angle between the tangent and the horizontal axis x is denoted by a symbol $\theta(s)$. It is assumed the string is inextensible, and that the moment/curvature relation obeys the *Euler-Bernoulli* theory. For the string in equilibrium, the sum of forces must be zero which leads to the following equations:

$$\frac{\mathrm{d}}{\mathrm{d}s}\left(T(s)\cos\theta(s) + V(s)\sin\theta(s)\right) = 0\,, \tag{7.1}$$

$$\frac{\mathrm{d}}{\mathrm{d}s}\left(T(s)\sin\theta(s) - V(s)\cos\theta(s)\right) = \rho_A\, b\, g\,. \tag{7.2}$$

Equation (7.1) represents that the change of horizontal force with respect to s is zero[1]. Equation (7.2) represents the same condition for the vertical forces. The sum of moments is zero in static equilibrium too:

$$M(s) + \mathrm{d}M(s) - V(s)\,\mathrm{d}s - M(s) = 0\,. \tag{7.3}$$

It leads to the relation between the shear force and the moment $M(s)$:

$$V(s) = \frac{\mathrm{d}M(s)}{\mathrm{d}s}\,. \tag{7.4}$$

The moment is computed according to *Euler-Bernoulli* theory. Consider a curved element as shown in Fig. 7.4. According to the *Euler-Bernoulli* theory, the cross-section remains straight in the deformed configuration. Thus, one

[1] It is equal to the condition that sum of all horizontal forces is zero.

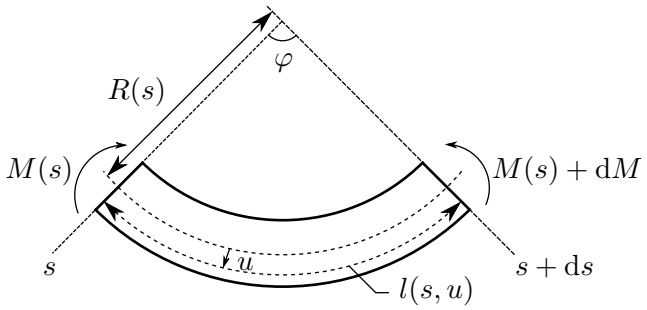

Figure 7.4: The element of a curved string at position s. Variable u represents the coordinate perpendicular to the neutral axis. The length of the element $l(u)$ changes with u linearly according to *Euler-Bernoulli* theory. The radius of curvature is denoted by symbol R.

site of the curved element is compressed while the opposite site is extended. Let us denote by symbol u the position on the element perpendicular to the neutral axis. The length of the element $l(s, u)$ for the radius of curvature $R(s)$ is computed as:

$$l(s, u) = \varphi(s)\,(R(s) + u) = \frac{R(s) + u}{R(s)}\,l(s, 0)\,, \tag{7.5}$$

where $l(s, 0)$ is the length of the neutral axis of the element, which is equal to the element rest state length because the string is inextensible. The strain of the element is computed as:

$$\varepsilon(s, u) = \frac{l(s, u) - l(s, 0)}{l(s, 0)} = \frac{u}{R(s)}\,. \tag{7.6}$$

We assume that stress/strain relation obeys Hooke's law:

$$\sigma(s, u) = E\,\varepsilon(s, u) = E\,\frac{u}{R(s)}\,, \tag{7.7}$$

where E stands for Young's modulus. The moment acting on the element is computed as:

$$M(s) = \int_A u\,\sigma(s, u)\,\mathrm{d}A = \frac{E}{R(s)}\int_A u^2 \mathrm{d}A = \frac{E\,I}{R(s)}\,, \tag{7.8}$$

where I is the second moment of the area of the string cross-section. For example, for the rectangular cross-section it equals to $I = bh^3/12$. This relations were derived for the continuous isotropic material without an internal structure. Neither E nor I have good meaning for the fabric materials. Thus, we introduce coefficient $K = E\,I$, which represents the bending stiffness of the material. According to [Sochi, 2016], the radius of curvature is related to the change of angle as:

$$\frac{1}{R(s)} = \frac{\mathrm{d}\theta(s)}{\mathrm{d}s}\,. \tag{7.9}$$

Combination of (7.4), (7.8), and (7.9) results in:

$$V(s) = K \frac{\mathrm{d}^2\theta(s)}{\mathrm{d}s^2} \,. \tag{7.10}$$

The set of equations (7.1, 7.2, 7.10) describing the contact free string depends on several material properties. The number of properties can be reduced by introducing new variables:

$$\tilde{M}(s) = \frac{M(s)}{\rho_A \, b \, g} \,, \quad \tilde{V}(s) = \frac{V(s)}{\rho_A \, b \, g} \,, \quad \tilde{T}(s) = \frac{T(s)}{\rho_A \, b \, g} \,. \tag{7.11}$$

By substituting (7.10) and (7.11) into (7.1) and (7.2), we obtain:

$$\frac{\mathrm{d}}{\mathrm{d}s} \left(\tilde{T}(s) \cos\theta(s) + \frac{1}{\eta} \frac{\mathrm{d}^2\theta(s)}{\mathrm{d}s^2} \sin\theta(s) \right) = 0 \,, \tag{7.12}$$

$$\frac{\mathrm{d}}{\mathrm{d}s} \left(\tilde{T}(s) \sin\theta(s) - \frac{1}{\eta} \frac{\mathrm{d}^2\theta(s)}{\mathrm{d}s^2} \cos\theta(s) \right) = 1 \,, \tag{7.13}$$

where $\eta = \frac{\rho_A \, b \, g}{K}$ is the weight to stiffness ratio. The substitution (7.11) can be used because the robot controls the grippers position independently of the force required. After the substitution, the model depends on the *weight-to-stiffness-ratio* only. If we need to know values of $M(s)$, $V(s)$ and $T(s)$, the constant K or ρ_A has to be measured in addition to η.

The following equations hold for the Cartesian position of the string elements:

$$\frac{\mathrm{d}x(s)}{\mathrm{d}s} = \cos\theta(s) \,, \qquad \frac{\mathrm{d}z(s)}{\mathrm{d}s} = \sin\theta(s) \,. \tag{7.14}$$

A system of the first order ordinary differential equations (ODE) is created from the higher order ODEs (7.12, 7.13, 7.14). A vector representing the state of the element is introduced:

$$\boldsymbol{q}(s) = \left[\theta(s), \;\; \tilde{M}(s), \;\; \tilde{V}(s), \;\; \tilde{T}(s), \;\; x(s), \;\; z(s) \right]^\top \,. \tag{7.15}$$

The system of the first order ODEs is:

$$\frac{\mathrm{d}\boldsymbol{q}(s)}{\mathrm{d}s} = \begin{bmatrix} \eta \, q_2 \\ q_3 \\ -\cos q_1 + \eta \, q_2 \, q_4 \\ \sin q_1 - \eta \, q_2 \, q_3 \\ \cos q_1 \\ \sin q_1 \end{bmatrix} \,, \tag{7.16}$$

where q_i is the i-th element of the vector $\boldsymbol{q}(s)$.

7.1.2 State of the String

Equation (7.16) describes the change of the element state with respect to the position on the string. The string state is determined by state of all its elements $\boldsymbol{q}(s)$, for $s \in \langle 0, l \rangle$, where l represents the string length. To find the state of the string we need to specify boundary conditions. The boundary condition fixes the state of the string at its boundary. We denote the boundaries as:

$$\boldsymbol{q}(0) = \boldsymbol{q}_1^- , \qquad \boldsymbol{q}(l) = \boldsymbol{q}^+ , \tag{7.17}$$

where superscript '$-$' denotes the left boundary condition and superscript '$+$' denotes the right boundary condition, similarly for other variables ($\tilde{T}^-, \theta^+$, etc.).

Finding the solution leads to a boundary value problem [Bellman and Kalaba, 1965]. We used an implementation described in [Kierzenka and Shampine, 2008] to solve it. Six first order ODEs (7.16) require six boundary conditions to be specified. The examples of string state for different boundary conditions are shown in Fig. 7.5.

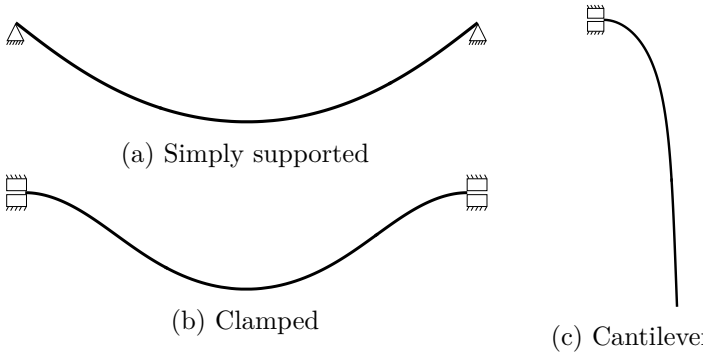

Figure 7.5: The examples of the string state for different boundary conditions. In the simply supported case (a), the both edges of 1 m long string are fixed at the specific position and rotated such that moments on the boundaries are zero. It was achieved by boundary conditions: $\tilde{M}^- = \tilde{M}^+ = 0$, $x^- = z^- = z^+ = 0$, $x^+ = 0.9$. In the clamped case (b), the fixed angles are required instead of zero moments, i.e. the first two conditions are changed to: $\theta^- = \theta^+ = 0$. The last case (c) shows the cantilever string which is fixed on one edge only according to boundary conditions: $x^- = z^- = 0$, $\theta^- = 0$, $\tilde{M}^+ = 0$, $\tilde{V}^+ = 0$, $\tilde{T}^+ = 0$. The last three terms assures that string hangs under its weight only, i.e. there is no addition force or moment on the boundary.

7.1.3 Effect of Contacts

Let us consider a scenario visualised in Fig. 7.6, where the string is held by a gripper at one side ($s = l$) and is supported by a folding surface on the other side ($s = 0$). It is assumed the folding surface is flat and horizontal. The string touches the surface for the first time at the touchdown point (TDP). The TDP divides string into two sections: The first section is contact free

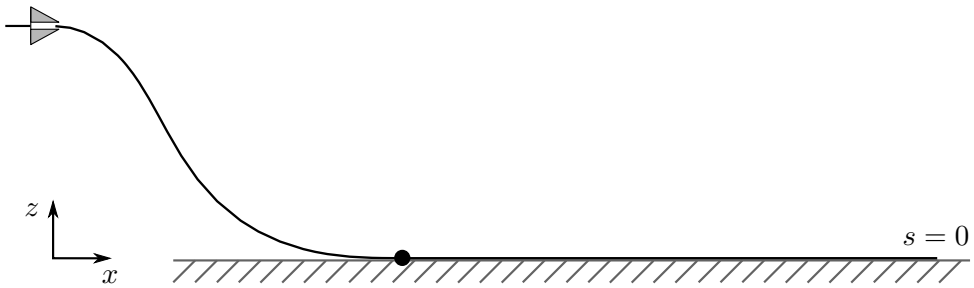

Figure 7.6: The string supported by a folding surface and held by a gripper at one side. The black dot shows the position of the first string/surface contact. This contact point is called touchdown point (TDP).

and described by equations (7.16). The second section lies on the surface, it is flat and horizontal.

The shape of the lying section is known. Thus, we can model the first section only and choose boundary conditions which consider the contact with the surface. For example, the angle at TDP equals to 180° and the moment is zero. However, the length of the section, which is contact free, is not known a priori. Since the solver requires known limits of integration, we reformulate the string model (7.16) into the dimensionless formulation. It is achieved by substitution $s = \varepsilon\, l$, where ε is a dimensionless position of the element. The length is then treated as an unknown variable. Because we add one unknown variable, we need to specify one more boundary condition. Therefore, we need 7 boundary conditions to find a state of the unknown length string. The state in Fig. 7.6 was generated with the boundary conditions:

$$\begin{aligned} &\theta^- = 180°, && \tilde{M}^- = 0, && \tilde{T}^- = 0, && z^- = 0, \\ &\theta^+ = 180°, && x^+ = 0, && z^+ = 0.25\,. \end{aligned}$$

In this scenario, the length of the contact free string was estimated to be $l_1 = 0.42$ m.

7.1.4 State of the Model

The model incorporates a contact of the garment with the desk and a contact of the garment with the garment itself. The garment is in the partial contact with the desk during the whole folding. The garment contact with itself occurs after the upper layer touches the lower layer of the garment. Considering these two contacts, we model the garment by four neighbouring sections. Two of these sections are hanging in air and are modeled according to dimensionless formulation of equations (7.16). The other sections are in contact, and they affect the boundary conditions of the strings in air. The state in which both contacts occur is shown in Fig. 7.7. The contact of the garment with the desk affects only the left boundary condition of the first string (i.e. $\boldsymbol{q}_1^-$). The contact between the garment layers affects the boundary conditions $\boldsymbol{q}_1^+$ and $\boldsymbol{q}_2^-$. The grasping by gripper affects the boundary conditions $\boldsymbol{q}_2^+$.

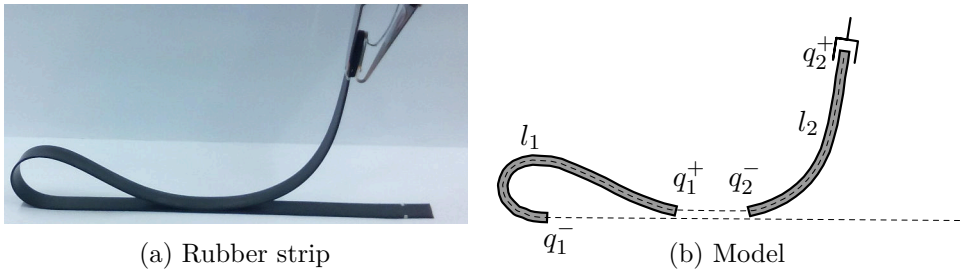

(a) Rubber strip (b) Model

Figure 7.7: The state of the model with both types of contacts: the contact between the garment and the folding surface, and between the garment itself. Figure (a) shows the real rubber while folding and figure (b) shows its model. Two strings with length l_1 and l_2 are used to represent this state. The effects of the contacts are incorporated into the strings boundary conditions $\boldsymbol{q}_i$.

Two garment state situations need to be distinguished while folding: The state, in which the contact between the lower and the upper layer does not exists (Fig. 7.6) and the state where it does (Fig. 7.7). In the former situation, only one string is modeled. In the latter case, two strings are used. Thus, the garment model consists of two strings, and individual states are distinguished by the boundary conditions. Fourteen conditions have to be specified in order to find a garment state. They restrict two times six first-order ODEs (7.16) and two unknown lengths of the strings.

7.2 Path Generation

The individual states of the model are determined by the boundary conditions. The boundary conditions specify the folding task by considering the restrictions of geometry and applied forces. For example, one of the conditions restricts the moment to be zero at the grasping point ($\tilde{M}_2^+ = 0$). It allows us to seek for the grasping point position only and to compute the orientation of the gripper afterwards according to the methodology described in Section 5.2.2.

While folding, four groups of states are distinguishable, and they correspond to the folding phases. The individual phases are shown in Fig. 7.8. The garment states during a single phase are determined by the constant boundary conditions except and one control variable $\delta_j(\tau)$. The control variable $\delta_j(\tau)$ parametrizes the robot motion and is a monotonic function of τ during the *Phase j*.

7.2.1 Folded State

Only the first string is modeled in the folded state. The boundary conditions ensure that the string is supported by the table at the beginning of the string and by the lower garment layer at the end of the string. The seven boundary conditions, which describe the folded state, are listed in the first column of Table 7.1. The individual rows of the table correspond to equations

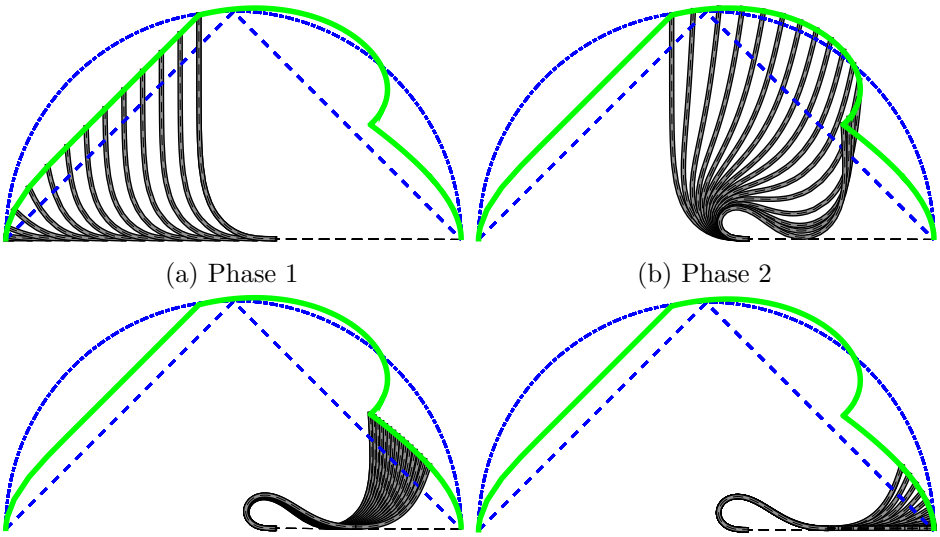

(a) Phase 1 (b) Phase 2

(c) Phase 3 (d) Phase 4

Figure 7.8: Individual folding phases and the garment states in the phases. First two phases (a, b) show the situation before the garment parts touch each other, i.e. there is only contact between the garment and the desk. Both types of contacts occur in the *Phase 3* (c) and *Phase 4* (d). The path planned according to the described model is shown in green color. The triangular and circular paths are shown in blue color.

representing the boundary conditions. For example, the first row for the first column of the table represents the boundary condition:

$$\theta_1^- = 180^\circ\,. \tag{7.18}$$

It means that the angle at the touchdown point is restricted to be 180° in the folded state. In the situations where only one string is used for the modeling, we use symbol | to indicate that the other string is not used. The symbol × represents that the value at the boundary is not constrained. For example, shear force V at both boundaries can be arbitrary because it represents the reaction force of the contact in the folded state. Note, that boundary conditions are specified in such a way that the folded garment layers overlay. The length l can be easily adjusted, if different folding is desired.

The constants $\frac{3h}{2}$ and $\frac{h}{2}$ appear because the string model represents a neutral axis. The neutral axis is in the middle of the string due to the assumption of constant density and the rectangular shape. The constant h is negligible unless multiple folds are stacked.

The boundary condition restricting the x-position of the string was derived from the inextensibility assumption. The following equation represents that the garment in the folded state is inextensible:

$$\left(\frac{l}{2} - x_1^-\right) + \left(\frac{l}{2} - x_1^+\right) + l_1 = l\,, \tag{7.19}$$

where the term $(\frac{l}{2} - x_1^-)$ represents length of the section which is in contact with the desk, and the term $(\frac{l}{2} - x_1^+)$ represents the length of the section

	Folded State	Phase 1	Phase 2	Phase 3	Phase 4
θ_1^-	$180°$	|	|	$180°$	|
$\tilde{M}_1^-$	0	|	|	0	|
$\tilde{V}_1^-$	$\times$	|	|	$\times$	|
$\tilde{T}_1^-$	0	|	|	$\times$	|
x_1^-	$l_1 - x_1^+$	|	|	$x_1^-(\tau_e)$	|
z_1^-	$\frac{h}{2}$	|	|	$\frac{h}{2}$	|
θ_1^+	0	|	|	0	|
$\tilde{M}_1^+$	$\times$	|	|	$\times$	|
$\tilde{V}_1^+$	$\times$	|	|	$\times$	|
$\tilde{T}_1^+$	$\times$	|	|	$\times$	|
x_1^+	$\times$	|	|	$\times$	|
z_1^+	$\frac{3h}{2}$	|	|	$\frac{3h}{2}$	|
θ_2^-	|	$180°$	$180°$	0	0
$\tilde{M}_2^-$	|	0	0	$\tilde{M}_1^+$	0
$\tilde{V}_2^-$	|	$\times$	$\boldsymbol{\delta_2(\tau)}$	$\tilde{V}_1^+ - \boldsymbol{\delta_3(\tau)}$	$\times$
$\tilde{T}_2^-$	|	0	$\times$	$\tilde{T}_1^+$	0
x_2^-	|	$l_2 - \frac{l}{2}$	$x_1^-(\tau_e)$	x_1^+	$\frac{l}{2} - l_2$
z_2^-	|	$\frac{h}{2}$	$\frac{h}{2}$	$\frac{3h}{2}$	$\frac{3h}{2}$
θ_2^+	|	$\times$	$\times$	$\times$	$\times$
$\tilde{M}_2^+$	|	0	0	0	0
$\tilde{V}_2^+$	|	$\times$	$\times$	$\times$	$\times$
$\tilde{T}_2^+$	|	$\times$	$\times$	$\times$	$\times$
x_2^+	|	$\times$	$\times$	$\times$	$\times$
z_2^+	|	$\times$	$\times$	$\times$	$\times$
l_1	$\times$	|	|	$\times$	|
l_2	|	$\boldsymbol{\delta_1(\tau)}$	$x_1^-(\tau_e) + \frac{l}{2}$	$x_1^-(\tau_e) - l_1 + \frac{l}{2}$	$\boldsymbol{\delta_4(\tau)}$

Table 7.1: The boundary conditions for the individual folding phases. The symbol $\times$ represents that variable is not constrained. The symbol | indicates that the string is not modelled. The symbol δ_i parametrizes the Phase i.

which in in contact with the garment lower layer. Rearranging Equation (7.19) results in the boundary condition:

$$x_1^- = l_1 - x_1^+ \,. \tag{7.20}$$

The folded states for different values of *weight-to-stiffness-ratio* are shown in Fig. 7.9

7.2.2 Folding Phases

In the *Phase 1*, the garment is lifted up until its touchdown point reaches the expected position, which was computed from the folded state. The *Phase 2* bends the garment until the contact between the garment layers occurs. In the first two phases, there is no contact between the garment layers and thus only the second string is modeled. The contact introduces another seven

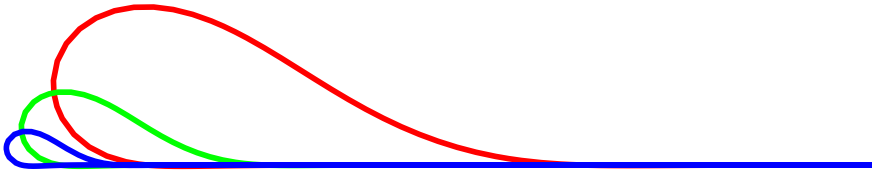

Figure 7.9: Folded states of 1 m long strip for different values of the *weight-to-stiffness-ratio* η. The red strip has stiffness $\eta = 10^3$, the green strip has stiffness $\eta = 10^4$, and the blue strip has stiffness $\eta = 10^5$.

conditions for the first string, and it is examined in the *Phase 3* and *Phase 4*. In the former case, there is one point contact only, and the point of the contact moves in the direction of folding. The point of the contact is rolling without sliding. At the end of the *Phase 3*, the first string reaches its final shape. In the *Phase 4*, the second string is put on the lower layer until its length is zero.

Some of the boundary conditions depend on the values computed in a specific phase. For example, the expected position of the touchdown point is determined by the folded garment state. The phases are thus solved in the mixed order. First, the folded state is solved followed by the phases solving in order: 1, 4, 3, 2. It ensures that all required values are known before solving the phase. The *Phase 3* and *Phase 4* are further solved backwards in time.

Phase 1. The garment path starts from a state, in which the garment lies on the desk and with the second string length equals to zero. The length of the string then increases linearly with time, which results in the garment lifting. During the lifting, the touchdown point is moving in the direction of folding. The lifting continues until the touchdown point reaches its final position, which was computed in advance based on the folded state of the garment. The variable δ_1 varies from 0 to $x_1^-(\tau_e) + \frac{l}{2}$, where τ_e represents the end of the folding and $x_1^-(\tau_e)$ is the boundary value of the folded state.

Phase 2. In *Phase 2*, the garment should rather bend than be lifted. The length of the lifted section is fixed. The shear force V_2^- controls *Phase 2*, as we observed it is increasing monotonically during this phase. The shear force is increasing until the upper layer touches the lower layer of the garment. The control variable δ_2 varies from value $V_2^-(\tau_{1e})$ to $V_1^-(\tau_{3s})$, where τ_{1e} represents the end of the *Phase 1* and τ_{3s} represents the start of the *Phase 3*. The value of $V_1^-(\tau_{3s})$ is known from the *Phase 3*.

Phase 3. In *Phase 3*, there is a point contact between the lower and the upper layer of the garment. The contact results in a discontinuity between the shear forces V_1^+ and V_2^-. The control variable δ_3 represents this discontinuity. The range of the control variable is from value $V_1^+(\tau_{4s}) - V_2^-(\tau_{4s})$ to 0. In *Phase 3*, only a single point of the upper layer is in the contact. The position of this point changes with the control variable.

Phase 4. The last phase represents the lowering of the garment. The first string reached its final state as modeled by the folded state (Section 7.2.1). The shape of the first string does not change in this phase. The control variable δ_4 represents the length of the second string varying from 0 to its maximal length computed as $\frac{l}{2} - x_1^+(\tau_e)$. The last state of this phase is equal to the folded garment state.

7.2.3 Folding Path

The previous sections describe how to obtain the garment state at the time τ. The folding path is computed from the obtained state directly:

$$\boldsymbol{x}_g(\tau) = \left(x_2^+(\tau), \quad y_g(\tau_s), \quad z_2^+(\tau)\right)^\top , \qquad \tau \in (\tau_s, \tau_e\rangle \ , \tag{7.21}$$

where $y_g(\tau_s)$ represents the constant grasping point position in y-axis direction.

The orientation of the gripper is aligned with the state of the grasped part of the garment. The angle of the gripper in xz-plane corresponds to the angle $\theta_2^+(\tau)$. The azimuth angle measured in a tangent plane of the grasping point is constant and is selected according to the azimuth relaxation technique described in Section 6.1. The folding paths for different values of η are visualized in Fig. 7.10.

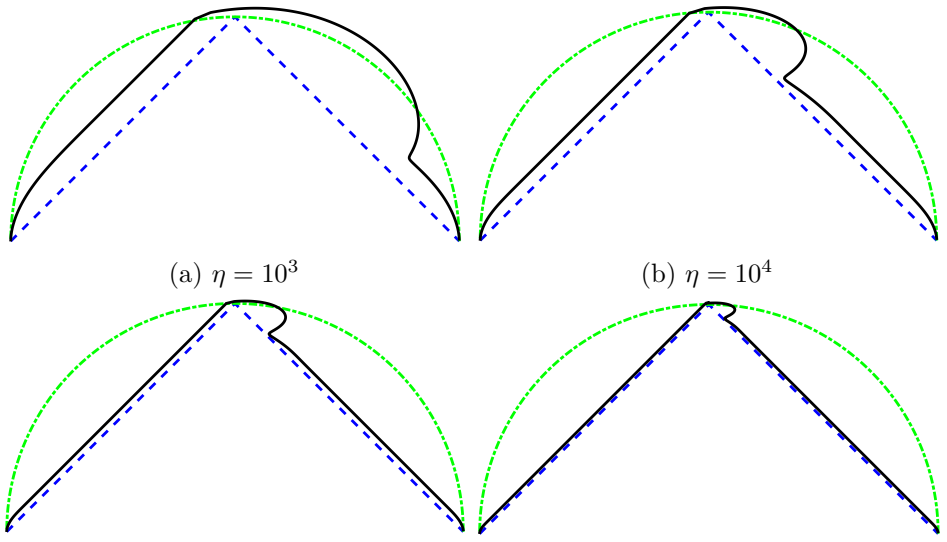

(a) $\eta = 10^3$ (b) $\eta = 10^4$ (c) $\eta = 10^5$ (d) $\eta = 10^6$

Figure 7.10: Folding paths for the different values of *weight-to-stiffness-ratio* η.

7.3 Folding Accuracy Experiments

We performed the experiment measuring the quality of the single fold for various garment materials and folding surfaces. The quality of the fold is evaluated by two variables: 1) the slippage e of the lower layer from its initial

position and 2) the displacement d of the planned and real position of the grasped side of the folded garment. The signed displacement is used in a way that positive values are used if the grasped side extends beyond the planned position. The displacements measurement is visualised in Fig. 7.11.

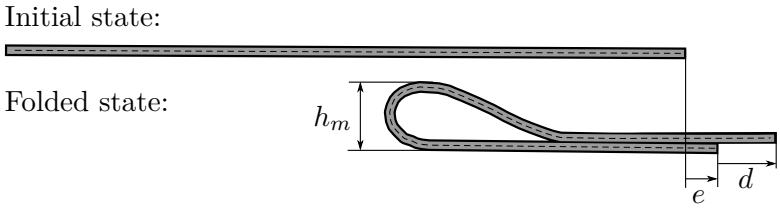

Figure 7.11: The displacement measurement after the fold is performed. The slippage e and the displacement d measure the quality of the fold. The maximal height h_m is used to estimate the material property.

7.3.1 Samples

We tested the folding path accuracy on narrow strips and two towels. The narrow strips were folded by one gripper only. The towels were folded by two grippers, each grasping one corner of the towel.

Two fabrics were used for the strips: synthetic (more flexible) and denim (stiffer). Furthermore, the strips with lower weight to stiffness ratio η were used: the Ethylene Propylene Diene Monomer rubbers with various thicknesses. Different thickness of the strips represents the different η in the experiment. Since the friction between the rubber and the desk is large, we also conducted experiments with the paper sheet inserted between the rubber and the folding surface and denoted them as table/paper surface. Strips slide on the paper-table interface if the horizontal force is larger than the friction force between the paper and the table surface.

The values of the *weight-to-stiffness-ratio* η was not known exactly and was estimated by the operator in advance of folding. The estimation was based on the maximal height of the manually folded garment as visualized in Fig. 7.11. This technique of estimation is called free fold test and was designed in work [Stuart, 1966]. See [Plaut, 2015] for the overview of estimation techniques. In the experiment, the garment was folded manually by the operator, and the maximal height was measured. The manual fold uses the gravity for the garment bending similarly to the robotic folding. No additional force was used to deform the folded shape. The effect of the non-modeled deformation caused by the internal friction is thus minimised during the weight to stiffness estimation. The *weight-to-stiffness-ratio* was then estimated from the experimentally obtained relation between the ratio η and the maximal height h_m. The relation was obtained by the folded state simulation and is visualized in Fig. 7.12. The measured and estimated properties of the used materials are shown in Tab. 7.2.

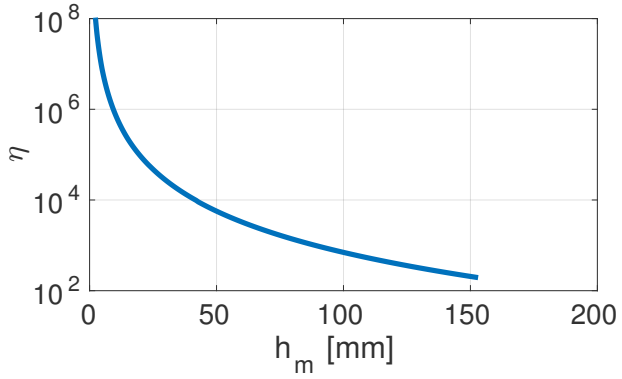

Figure 7.12: The relation between the maximum height h_m and the weight to stiffness ratio η.

	l / b / h [mm]	h_m [mm]	ρ_A [kgm^{-2}]	K [Nm^2]	η [m^{-3}]
synthetic	525 / 57 / 1	10	0.75	$5.3{\cdot}10^{-7}$	800000
denim	525 / 110 / 1	30	0.70	$2.6{\cdot}10^{-5}$	30000
rubber1	995 / 36 / 3	70	3.95	$5.9{\cdot}10^{-4}$	2400
rubber2	995 / 59 / 4	89	5.25	$2.7{\cdot}10^{-3}$	1150
rubber3	995 / 50 / 5	99	6.55	$3.9{\cdot}10^{-3}$	850
towel1	590 / 360 / 1	24	0.30	$1.9{\cdot}10^{-5}$	58000
towel2	560 / 490 / 2	28	0.60	$7.6{\cdot}10^{-5}$	38500

Table 7.2: The properties of used materials. The lengths l, b, h are garment dimensions. The symbol h_m represents the maximal height of the folded garment and symbols ρ_A, K and η stand for the material properties.

7.3.2 Results Evaluation

We design folding paths for the measured lengths and estimated weight to stiffness ratios (Tab. 7.2). The paths were designed such that garment edges should be aligned at the end of the folding. Two folding surfaces were used: a melamine faced chipboard table surface and a table covered by a rough tablecloth. The measured results are shown in Tab. 7.3

Narrow Strips

Table 7.3 indicates that there is a relation between the slippage and displacement of the triangular folding path and the surface friction. The lower slippages/displacements were measured for the higher friction. Furthermore, the lower *weight-to-stiffness-ratio* results in the higher slippage/displacement as well. This fulfils the expectation of the triangular folding path as it was designed for infinitely flexible garments (infinite η) and for infinite surface friction. Based on the oriented displacements, it can be concluded that triangular folding path has a tendency to push the garment in the direction of motion.

On the contrary, the circular path tends to pull the garment. The circular folding path outperformed the triangular path in the situations with low η only.

Our model-based path outperformed both purely geometrical methods: the triangular as well as the circular folding path. There is no relation between the friction and the measured displacement for our path in the experiment. It is a result of the minimization of the horizontal force, which prevents the slipping of the garment in the most cases. We did not observe any slipping in the experiment.

Real Rectangular Garments

Two real towels were folded in order to show that the model is sufficient for rectangular garments folded by two grippers. The towel was grasped by its corners as shown in Fig. 7.2. A single folding path was designed using our one dimensional representation and this path was followed by both grippers simultaneously. We observed that the model error is negligibly small, when folding with two grippers. The measured results are shown in the lower part of Table 7.3. The errors are similar to strips folding: the triangular path

Surface	Garment	μ [-]	Slippage [mm] / Displacement [mm] Folding path		
			Triangular	Circular	Our Model
table	synthetic	0.20	6 / -24	-10 / 46	**0 / -5**
	denim	0.26	15 / -28	-14 / 40	**0 / -1**
	rubber_1	0.57	31 / -46	-21 / 68	**0 / -2**
	rubber_2	0.57	28 / -45	-18 / 47	**0 / 4**
	rubber_3	0.57	30 / -50	-11 / 32	**0 / 5**
table/paper	rubber_1	0.31	39 / -55	-32 / 62	**0 / -3**
	rubber_2	0.31	64 / -82	-35 / 53	**0 / 3**
	rubber_3	0.31	70 / -91	-24 / 37	**0 / 5**
tablecloth	synthetic	0.53	0 / -19	0 / 31	**0 / -7**
	denim	0.81	0 / -10	0 / 28	**0 / -4**
	rubber_1	0.80	23 / -42	-8 / 43	**0 / -2**
	rubber_2	0.80	25 / -46	-8 / 39	**0 / 2**
	rubber_3	0.80	30 / -50	-5 / 22	**0 / 3**
table	towel_1	0.28	17 / -35	-10 / 56	**0 / 5**
	towel_2	0.24	28 / -40	-10 / 43	**0 / 3**
tablecloth	towel_1	1.23	0 / -23	0 / 41	**0 / 4**
	towel_2	1.20	0 / -25	0 / 30	**0 / 3**

Table 7.3: The measured lower layer slippage e and the measured layers displacement d. The upper part of the table shows the displacements for the narrow strips and the rest shows displacements for the real garments. The garments are ordered based on the weight to stiffness ratio η. The measured static friction coefficient is denoted by μ.

outperformed the circular path and the displacement of the triangular folding can be lowered by the higher friction. Our folding path outperformed both of them. The results indicate that our folding path can be used when folding rectangular garment with a dual arm robot without explicitly modeling of two dimensions.

7.4 Folding Accuracy as a Function of Material Properties

The *weight-to-stiffness-ratio* η is estimated accurately in advance. This estimate is used to generate the folding path, which is executed by the robot. In reality, the estimation of the *weight-to-stiffness-ratio* might be inaccurate. As a consequence, the designed folding path is not suitable for the given material. The purpose of these experiments is to analyze the quality of the fold when η_t, used for path generation, differs from the material weight to stiffness ratio η_m. We fold several materials both in simulation and in real robotic folding, and the resulting folds were analyzed based on the displacement d (Fig. 7.11).

In addition, we consider a situation, in which the *weight-to-stiffness-ratio* cannot be measured exactly, but the range of the ratio values is known. We demonstrate that the fixed value of the ratio produces acceptable fold quality for a reasonable range of the ratio values. We show that only four *weight-to-stiffness-ratio* values can be used to fold all typical fabrics varying from a soft (e.g. sateen) to a stiff (e.g. denim) material with the reasonable accuracy. Experiments show that for a given range of the *weight-to-stiffness-ratio* one has to choose the value on the pliable end of the range to achieve acceptable results.

Two undesirable events influence the displacement: the slipping of the strip and the bending behaviour. In this work, the effect of bending behaviour is studied and the slipping is avoided by considering several assumptions. It is assumed, that the friction between the garment and the folding surface is high enough, so the slippage e of the non grasped side is zero. Furthermore, it is assumed that the friction between the garment layers is high enough as well, so the upper layer cannot slip on the lower layer. The slipping of the upper layer is unfavorable because it is hard to predict the amount of the slippage due to the elasticity of the real material and due to the high variance of the soft material friction behavior. Furthermore, it is not decidable in our model whether the upper layer will slip on the lower layer or both layers will slip on the folding surface.

7.4.1 Simulated Displacement

The model used for the path generation above was divided into four neighboring sections. These sections were introduced in order to simulate contacts. This division complicates the simulation of an arbitrary path following. To overcome this complication, we simulate the contact by a nonlinear

force $f(z(s))$, which depends on the element position $z(s)$. The modified model of the string is:

$$\frac{\mathrm{d}}{\mathrm{d}s}\left(\tilde{T}(s)\cos\theta(s) + \frac{1}{\eta}\frac{\mathrm{d}^2\theta(s)}{\mathrm{d}s^2}\sin\theta(s)\right) = 0\,, \tag{7.22}$$

$$\frac{\mathrm{d}}{\mathrm{d}s}\left(\tilde{T}(s)\sin\theta(s) - \frac{1}{\eta}\frac{\mathrm{d}^2\theta(s)}{\mathrm{d}s^2}\cos\theta(s)\right) = 1 - f(z(s))\,. \tag{7.23}$$

The contact force $f(z(s))$, which supports the part of the string laying on the table is modeled as:

$$f(z(s)) = \frac{1}{z^2}10^{-6}\,, \tag{7.24}$$

which implies that the folding surface is horizontal with the zero height. The force is already normalized by the term $\rho_A\, b\, g$. This model can simulate the string with a contact by a single section, i.e. there are six boundary conditions to define the state of the string.

To obtain the simulated displacement, the boundary conditions have to be modified such that the given path $\boldsymbol{u}(\tau) = \left[u_x(\tau)\,,\quad u_z(\tau)\,,\quad u_\theta(\tau)\right]^\top$ can be followed. The slippage of the upper layer is forbidden in the simulation and the displacement cannot be corrected after the layers touch. The simulation is described by the following boundary conditions:

$$\begin{aligned} \theta^- &= 180°, & \tilde{M}^- &= 0, & x^- &= l, \\ \theta^+ &= u_\theta, & x^+ &= u_x, & z^+ &= u_z\,. \end{aligned}$$

The simulation is stopped when the upper layer touches the lower layer and the displacement is computed.

For the purpose of the experiments, 24 different paths were generated. Two of these paths were triangular and circular. Other paths were generated for η_t interpolated logarithmically between the values: 10^3 and 10^6. These paths were then used to fold several materials, which differ in weight to stiffness ratio η_m in a range from 10^3 to 10^6. The measured displacements are shown in Fig. 7.13. It can be seen, that the displacement is zero in the case where $\eta_t = \eta_m$. It represents the situation in which the *weight-to-stiffness-ratio* was estimated accurately before path generation - i.e. the ideal scenario. The displacement is more or less increasing as the estimation is moving away from the ideal scenario. Furthermore, the displacement is not symmetric. For the situation where $\eta_t > \eta_m$, the displacement is lower than for the situations where $\eta_t < \eta_m$. It suggests that one should select the path on the pliable end of the known range of the material weight to stiffness ratio η. It means, that for the given η_m, we should use the larger η_t for the path generation. It will result in the satisfactory folding of all materials in the given range. Moreover, the smaller range will result in smaller displacement.

7.4.2 Real Displacement

We performed a real experiment with the *CloPeMa* testbed, where an industrial arm was used to fold the fabric strips. Strips with different weight to

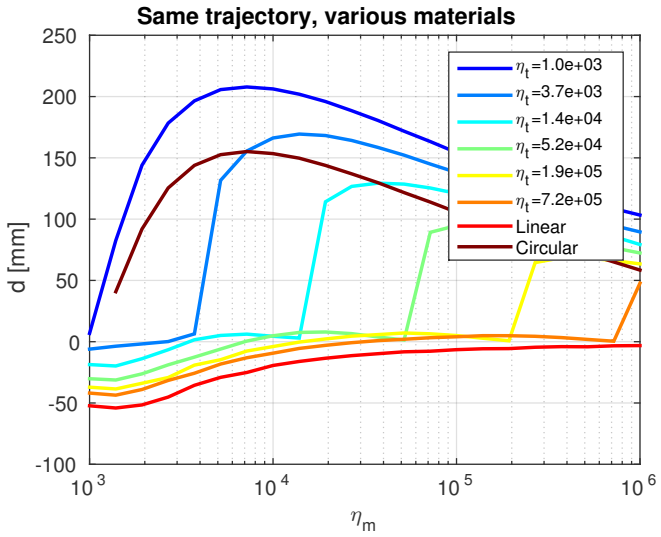

(a) Variable η_m

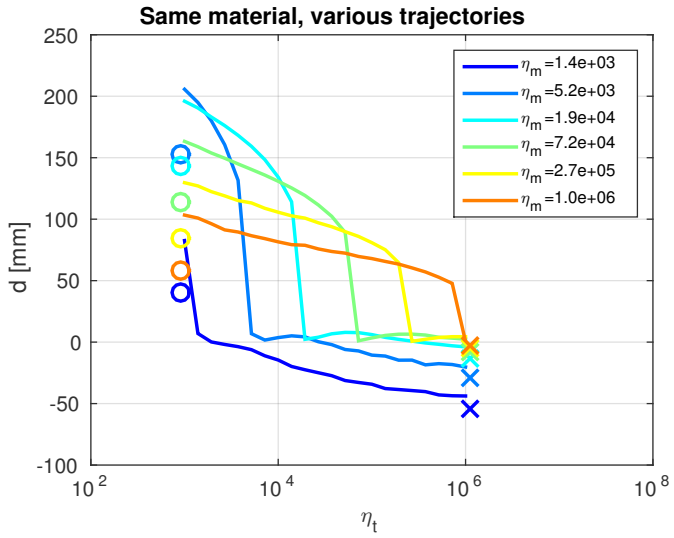

(b) Variable η_t

Figure 7.13: Simulated displacements - two different visualizations of the same experiment. The displacements for the selected paths (generated with η_t) are shown for all simulated materials η_m on the left side. On the right side, the displacements of the selected materials are shown for all paths. The cross and circle marker stand for the triangular and circular path, respectively.

stiffness ratios were folded by each generated path. The weight to stiffness ratios were estimated using the maximal height of the folded strips. To avoid the slipping of the strips on the table, the non grasped side was fixed to the table with the tape. The measured displacements together with simulated displacements for the estimated material are shown in Fig. 7.14. The measurements show, that simulation overestimated the oriented displacement for all situations except one, where $\eta_t = \eta_m$. Nevertheless, the hypothesis that path

on the pliable end should be selected is confirmed for the real displacements too.

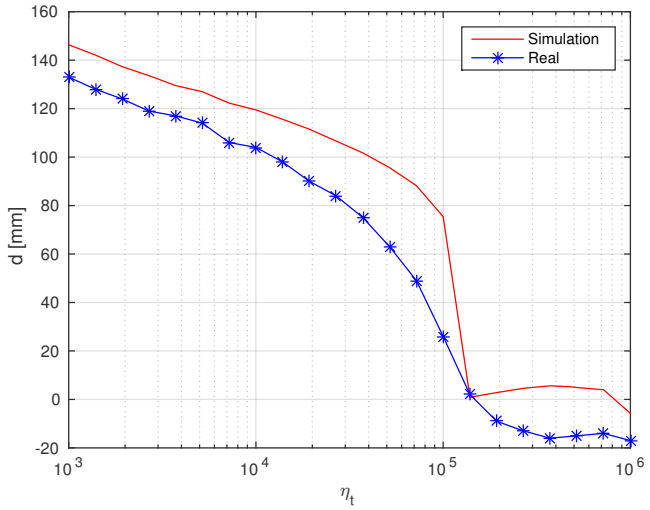

(a) $\eta_m = 1.4 \cdot 10^5$

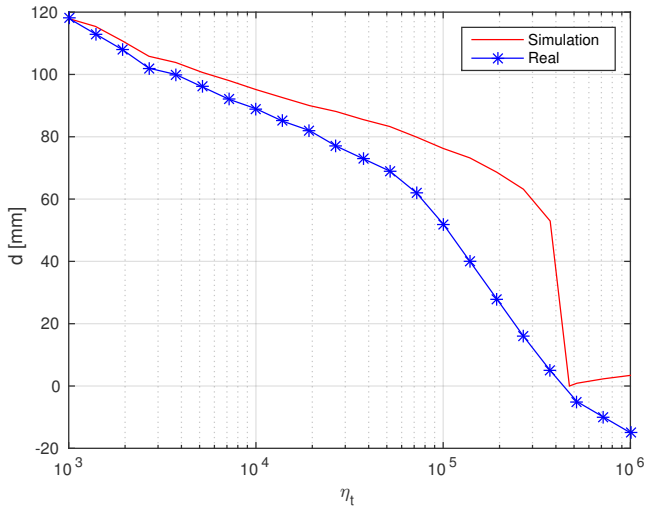

(b) $\eta_m = 4.7 \cdot 10^5$

Figure 7.14: Measured real displacement. The simulation overestimates the oriented displacement for all situations except one, where $\eta_t = \eta_m$. It represents the situation where the *weight-to-stiffness-ratio* is estimated accurately.

7.4.3 Model Inconsistency

The simulated displacements overestimation suggests that there is a systematic error in our model. To analyze it, we performed two experiments: the first to check the repeatability of the real displacement and the second to compare simulated and real shapes of the strips during folding.

The repeatability experiment was performed for one path ($\eta_t = 3.7 \cdot 10^5$) and one strip ($\eta_m = 5.5 \cdot 10^4$). The strip was folded 5 times, and the measured variance of the displacement was 0.5 mm. It shows satisfactory repeatability of the real robotics folding.

The second experiment compared the simulated and real strip states. For the comparison purposes, the camera was added to the testbed, and its field of view was geometrically calibrated. The calibration was used to project the simulated model into the image. The simulated state and the real state were compared visually. We observed that the model is inconsistent in the states shown in Fig. 7.15.

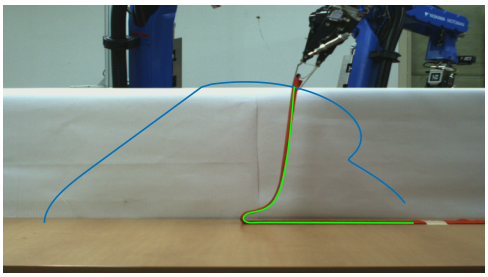

(a) Consistent

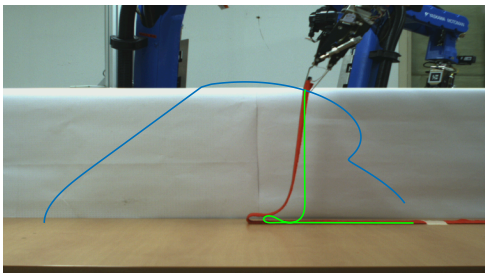

(b) Inconsistency start

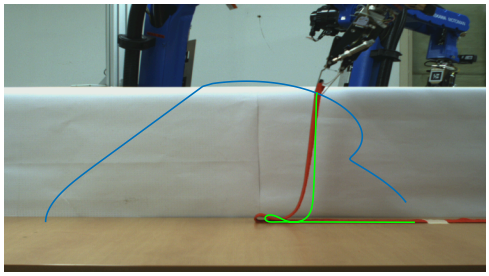

(c) Real touch

Figure 7.15: The systematic error in the model behavior. The real strip is red, the simulated state is shown in green color, and the followed path is blue. The simulation is consistent with the real strip shape in the first part of the path following (a). The difference appears when the situation shown in figure (b) is reached. In the situation (b), the simulated model skips in a single step considerably. The real strip catches up the simulation with a small delay but the touch point is shifted w.r.t. simulated state (c).

This inconsistency is caused by a dynamic movement of the real strip. Before the inconsistency appears, the strip shape can be determined by static analysis. The real strip moves dynamically until it touches the lower layer of the garment. However, our simulation seeks for static equilibrium only. Thus, it cannot follow the dynamic effects, and it finds the closest state which is in static equilibrium. Therefore, there is a discontinuity in the model when following an arbitrary path. Nevertheless, this inconsistency does not occur if the *weight-to-stiffness-ratio* is estimated accurately (i.e. $\eta_m = \eta_t$). Also, it does not influence the selection of the folding path for the known range of fabrics.

7.4.4 Fabric Folding with Limited Number of Paths

Our next experiment measures the displacement for the whole range of typical fabrics, when folded by four paths only. The motivation for this experiment is the reduction of planning time. Instead of the infinite number of paths parametrized by η, we use four paths which are planned offline. Then, according to the methodology described above, we select the path for the given fabric.

We divided the fabric strips into four categories based on the estimated weight to stiffness ratios η_m. For these categories, the path on the pliable end of the range (generated by η_t) is selected, and the folding is performed by the *CloPeMa* robot. The measured displacements are shown in Tab. 7.4. The table shows that displacement is maximally 10 mm for all used fabric strips of length 1000 mm (i.e. ≤ 1 %). For the purpose of robotic garment folding, this is an acceptable displacement. The displacement can be further reduced if more categories are used.

material	h_m [mm]	η_m	η_t	d [mm]
georgette	12	$4.7 \cdot 10^5$	$5.2 \cdot 10^5$	−5
chiffon	14	$3.2 \cdot 10^5$	$5.2 \cdot 10^5$	−9
acetate lining	16	$2.1 \cdot 10^5$	$5.2 \cdot 10^5$	−10
twill	17	$1.7 \cdot 10^5$	$1.9 \cdot 10^5$	−8
wool suiting	18	$1.6 \cdot 10^5$	$1.9 \cdot 10^5$	−6
herringbone pattern	19	$1.3 \cdot 10^5$	$1.9 \cdot 10^5$	−7
coating	20	$1.0 \cdot 10^5$	$1.9 \cdot 10^5$	−9
terry cloth	21	$9.0 \cdot 10^4$	$1.0 \cdot 10^5$	−7
denim	22	$7.7 \cdot 10^4$	$1.0 \cdot 10^5$	−4
plain weave	22	$7.7 \cdot 10^4$	$1.0 \cdot 10^5$	−6
chanel	25	$5.2 \cdot 10^4$	$7.2 \cdot 10^4$	−3

Table 7.4: Measured displacements when only four paths are used for fabric strips folding. The estimated *weight-to-stiffness-ratio* is denoted η_m, and the weight to stiffness ratio η_t was used to generate the folding path. The height of folded strip h_m was used for the estimation.

7.5 Results Evaluation

This chapter described the physics-based path generation method for a rectangular garment. In comparison with state-of-the-art method [Li et al., 2015b], we compute the garment state in each state of the folding path. Thus, the optimisation in the state space of paths is not necessary.

Our formulation minimizes the horizontal force and is able to fold the garment on a low friction surface. We demonstrated the accuracy of our approach in the real robotic garment folding. Furthermore, we analyzed the folding accuracy as a function of material property estimation. Based on the analysis we designed a methodology for the folding path selection in a

scenario where the material property is not known exactly but the range of its values is known.

However, the model we used is limited to one-dimensional garments. It can be used to fold narrow strips or rectangular garments in case of folding line aligned with garment edges. The next chapter generalizes the path generation method to be able to fold more complex garment shapes.

Chapter 8

Physics-Based Shell Folding Path

The direct extension of *Euler-Bernoulli* beam theory is *Kirchoff-Love* shell theory described in a series of works written by Simo et al. [Simo and Fox, 1989, Simo et al., 1989, Simo et al., 1990]. This theory is applicable for the fabric modelling too. In this chapter, the *Kirchoff-Love* shell model is employed for the single arm folding path generation task. One grasping point is used in the single arm folding task.

8.1 Garment Model

Thick and thin shells are modeled differently in the classical shell theory [Oñate, 2013]. Thick shells are described by *Reissner-Mindlin* theory, where transverse shear deformations are taken into account. For thin shells, the *Kirchhoff-Love* theory, which neglects the transverse shear deformations, is used. The finite element method (FEM) is usually used for calculating the shell model parameters.

8.1.1 State of the Art

Applying the *Reissner-Mindlin* theory for thin shells in FEM results in a phenomenon called *shear locking* [Oñate, 2013]. If the locking occurs, the predicted behavior is more stiff than the observed behavior. It makes the theory hard to use for the garment folding prediction as the garments are thin typically. The *Kirchoff-Love* theory does not suffer from the locking phenomena, but it is more difficult to derive its finite element formulation. The reason is that basis function for FEM requires to be C^1 continuous for *Kirchoff-Love* theory. This section provides an overview of methods developed to solve this continuity issue.

The derivation of *Kirchoff-Love* shell theory was described in a series of works [Simo and Fox, 1989, Simo et al., 1989, Simo et al., 1990]. This theory was utilized for rectangular fabric folding prediction in [Eischen et al., 1996].

The simulation of non-rectangular fabric according to *Kirchoff-Love* shell theory was achieved in [Cirak et al., 2000]. Author ensures the C^1 continuity by using a subdivision-surface concept for the shell modeling. The method was used to simulate garments with wrinkles in [Thomaszewski et al., 2006].

Another method applying the *Kirchoff-Love* theory FEM was proposed in [Noels and Radovitzky, 2008]. Authors utilize a discontinuous *Galerkin* finite element method weakly assuring C^1 continuity. The formulation was derived for nonlinear elastic shells later in work [Noels, 2009]. This method was used in computer graphics to simulate detailed cutting of shells [Kaufmann et al., 2009, Kaufmann, 2013].

Both formulations [Cirak et al., 2000, Noels and Radovitzky, 2008] assume small shell deformation only. To use the models for large deformations, a *corotational* formulation [Müller and Gross, 2004] can be used. In the *corotational* formulation, the rotation of the element is extracted, and the forces are computed for an un-rotated element. The computed forces are rotated back to the original element orientation.

A geometrically nonlinear finite element formulation was proposed in [Kiendl et al., 2009]. In geometrically nonlinear formulation the *corotational* formulation is not required. The geometric exactness was achieved by using NonUniform Rational B-Splines (NURBS) as basis functions. The method was used for garment simulation in works [Zheng, 2013, Lu and Zheng, 2014]. We use approach [Kiendl et al., 2009] in our analysis too.

8.1.2 *Kirchoff-Love* Shell Geometry

The formulation in this section follows work [Kiendl et al., 2009]. The *Kirchoff-Love* theory is based on the following assumptions:

- The thickness of the shell is assumed constant and small with respect to its overall size.
- The perpendicular cut to the shell remains planar after the deformation.

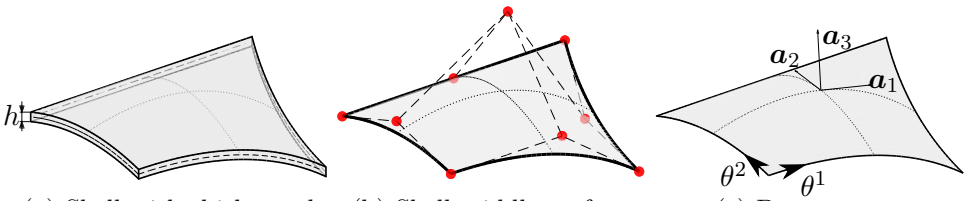

(a) Shell with thickness h (b) Shell middle surface and control points (c) Base vectors

Figure 8.1: The *Kirchoff-Love* shell (a) with the thickness h can be represented by its middle surface (b) and (c). The deformation of the middle surface is controlled by the finite amount of control points (red dots). The base vectors $(\boldsymbol{a}_1, \boldsymbol{a}_2, \boldsymbol{a}_3)$ can be evaluated at any point on the surface parametrized by the coordinates θ^1 and θ^2.

Complying with the *Kirchoff-Love* assumptions, the shell geometry is described by its middle surface (Fig. 8.1). Two shell configurations are distinguished: the reference (i.e. undeformed, strain-free) one and the deformed one. Both configurations are described by NURBS surface with the control points $\boldsymbol{P}_i$ and $\boldsymbol{p}_i$ for the reference and the deformed configuration, respectively.

The position of a material point in the reference configuration is computed as

$$\boldsymbol{X}(\theta^1,\theta^2) = \sum_i N_i(\theta^1,\theta^2)\,\boldsymbol{P}_i\,, \tag{8.1}$$

where θ^1 and θ^2 represents curvilinear coordinates of the shell, and $N_i(\theta^1,\theta^2)$ is i-th NURBS basis function [Hughes et al., 2005]. Analogously, the position in deformed configuration is

$$\boldsymbol{x}(\theta^1,\theta^2) = \sum_i N_i(\theta^1,\theta^2)\,\boldsymbol{p}_i\,. \tag{8.2}$$

The displacement of the material point is defined as: $\boldsymbol{u}(\theta^1,\theta^2) = \boldsymbol{x}(\theta^1,\theta^2) - \boldsymbol{X}(\theta^1,\theta^2)$. The covariant base vectors are computed for both configurations

$$\begin{aligned}
\boldsymbol{a}_1 &= \frac{\partial \boldsymbol{x}}{\partial \theta^1}, & \boldsymbol{a}_2 &= \frac{\partial \boldsymbol{x}}{\partial \theta^2}, & \boldsymbol{a}_3 &= \frac{\boldsymbol{a}_1 \times \boldsymbol{a}_2}{\|\boldsymbol{a}_1 \times \boldsymbol{a}_2\|},\\
\boldsymbol{A}_1 &= \frac{\partial \boldsymbol{X}}{\partial \theta^1}, & \boldsymbol{A}_2 &= \frac{\partial \boldsymbol{X}}{\partial \theta^2}, & \boldsymbol{A}_3 &= \frac{\boldsymbol{A}_1 \times \boldsymbol{A}_2}{\|\boldsymbol{A}_1 \times \boldsymbol{A}_2\|}.
\end{aligned}$$

These base vectors are used to compute the membrane strain $\varepsilon_{\alpha\beta}$ and changes in curvature $\kappa_{\alpha\beta}$, where indices α and β take the values $\{1,2\}$

$$\varepsilon_{\alpha\beta} = \frac{1}{2}\left(\boldsymbol{a}_\alpha \cdot \boldsymbol{a}_\beta - \boldsymbol{A}_\alpha \cdot \boldsymbol{A}_\beta\right), \qquad \kappa_{\alpha\beta} = \frac{\boldsymbol{A}_\alpha}{\partial\theta^\beta} \cdot \boldsymbol{A}_3 - \frac{\boldsymbol{a}_\alpha}{\partial\theta^\beta} \cdot \boldsymbol{a}_3. \tag{8.3}$$

Representing equations (8.3) in Voigt notation leads to

$$\boldsymbol{\varepsilon} = \begin{pmatrix}\varepsilon_{11}, & \varepsilon_{22}, & 2\,\varepsilon_{12}\end{pmatrix}^\top, \qquad \boldsymbol{\kappa} = \begin{pmatrix}\kappa_{11}, & \kappa_{22}, & 2\,\kappa_{12}\end{pmatrix}^\top. \tag{8.4}$$

8.1.3 Equilibrium Equation

We restrict our analysis to an isotropic elastic material. Such material is described by Young's modulus E, Poisson's ratio ν, area mass density ρ, and thickness h. The static equilibrium equation is given by [Kiendl, 2011]:

$$\begin{aligned}
\delta W &= \int_\Omega \delta\boldsymbol{u}^\top \rho\,\boldsymbol{g}\,\mathrm{d}A - \int_\Omega \left(\frac{h\,E}{1-\nu^2}\,\delta\boldsymbol{\varepsilon}^\top D\,\boldsymbol{\varepsilon} + \frac{h^3\,E}{12\,(1-\nu^2)}\,\delta\boldsymbol{\kappa}^\top D\,\boldsymbol{\kappa}\right)\mathrm{d}A\\
&= 0,
\end{aligned} \tag{8.5}$$

where δW represents the virtual work, Ω is a NURBS knot span [Hughes et al., 2005], $\mathrm{d}A$ is the differential area of the surface, $\boldsymbol{g}$ represents the gravitational acceleration, and $\delta\boldsymbol{u}$ is the variation of the displacement of $\mathrm{d}A$. The material matrix D depends on the Poisson's ratio and represents the isotropic material properties [Kiendl et al., 2009]. Its form for the isotropic material is a symmetric matrix:

$$D = \begin{pmatrix}
(A^{11})^2 & \nu A^{11}A^{22}+(1-\nu)(A^{12})^2 & A^{11}A^{12}\\
\nu A^{11}A^{22}+(1-\nu)(A^{12})^2 & (A^{22})^2 & A^{22}A^{12}\\
A^{11}A^{12} & A^{22}A^{12} & 0.5\big((1-\nu)A^{11}A^{22}+(1+\nu)(A^{12})^2\big)
\end{pmatrix}, \tag{8.6}$$

where $A^{\alpha\beta}$ are the contravariant components of the surface matrix tensor obtained by:

$$\begin{pmatrix} A^{11} & A^{12} \\ A^{21} & A^{22} \end{pmatrix} = \begin{pmatrix} A_{11} & A_{12} \\ A_{21} & A_{22} \end{pmatrix}^{-1}, \tag{8.7}$$

where $A_{\alpha\beta}$ are covariant components of the surface matrix tensor computed as:

$$A_{\alpha\beta} = \boldsymbol{A}_\alpha \cdot \boldsymbol{A}_\beta, \quad \alpha, \beta \in \{1, 2\}. \tag{8.8}$$

The material matrix D is derived from a more common form of the material matrix:

$$D^{iso} = \begin{pmatrix} 1 & \nu & 0 \\ \nu & 1 & 0 \\ 0 & 0 & 0.5(1-\nu) \end{pmatrix} \tag{8.9}$$

by transforming the quantities into the local Cartesian coordinate system. The derivation is described in the thesis [Kiendl, 2011].

According to Lu and Zheng [Lu and Zheng, 2014], the parameters h, E, and ν used in the Equation (8.5) are not suitable for the fabric simulation due to the internal fabric structure. They proposed to model the membrane stiffness and the bending stiffness by two independent functions. In our analysis, we approximate them by linear functions specified by the constant membrane and bending stiffnesses. By introducing *weight-to-membrane-stiffness* ratio:

$$\eta_m = \left(1 - \nu^2\right) \frac{\rho}{h\, E}$$

and *weight-to-bending-stiffness* ratio:

$$\eta_b = 12 \left(1 - \nu^2\right) \frac{\rho}{h^3\, E},$$

Equation (8.5) reads:

$$\begin{aligned} \delta W &= \int_\Omega \delta \boldsymbol{u}^\top \boldsymbol{g} \, \mathrm{d}A - \int_\Omega \left(\frac{1}{\eta_m} \delta \boldsymbol{\varepsilon}^\top D\, \boldsymbol{\varepsilon} + \frac{1}{\eta_b} \delta \boldsymbol{\kappa}^\top D\, \boldsymbol{\kappa} \right) \mathrm{d}A \\ &= 0. \end{aligned} \tag{8.10}$$

The fabric model characterised by η_m and η_b is rather phenomenological description of the fabric behaviour avoiding the details of threads and yarns interactions. The model is thus parametrized by the garment shape described by NURBS and by the material properties given by the Poisson's ratio and two *weight-to-stiffness* ratios.

The integration in Equation (8.10) is computed numerically according to Gaussian quadrature rule:

$$\begin{aligned} &\int_\Omega f \, \mathrm{d}x \, \mathrm{d}y = \int_I f(\phi(\theta_1, \theta_2)) \, |J_\phi| \, \mathrm{d}\theta_1 \, \mathrm{d}\theta_2 \\ &\simeq \sum_{i=1}^{n} \sum_{j=1}^{m} f(\phi(\psi_i, \psi_j)) \, |J_\phi(\theta_i, \theta_j)| \, \omega_i \, \omega_j \,, \end{aligned} \tag{8.11}$$

where ϕ represents the mapping of the area Ω into the square $I = [-1, 1] \times [-1, 1]$, J_ϕ is Jacobian matrix of the mapping, ψ_i and ψ_j are the integration points, and ω_i and ω_j are weights associated with the integration points. The integration points values are listed, e.g. in [Hughes et al., 2010].

8.1.4 Model State

Finding the model state leads to seeking for the displacement of control points such that Equation (8.10) is satisfied for an arbitrary variation of the displacement variable

$$\delta W = \frac{\partial W}{\partial u_r} \delta u_r = 0, \tag{8.12}$$

where u_r represents the displacement variable of the r-th degree of freedom. For NURBS surface, the degrees of freedom correspond to the positions of the control points. The nonlinear system of Equations (8.12) is linearized and solved by Newton-Raphson method iteratively:

$$\frac{\partial W}{\partial u_r} + \frac{\partial^2 W}{\partial u_r \partial u_s} \Delta u_s = 0. \tag{8.13}$$

Introducing the residual force vector $\boldsymbol{R}$ and the stiffness matrix $\boldsymbol{K}$ yields to:

$$\boldsymbol{K} \Delta \boldsymbol{u} = -\boldsymbol{R}. \tag{8.14}$$

The more detailed explanation of $\boldsymbol{K}$ and $\boldsymbol{R}$ computation was provided in [Kiendl, 2011].

The different states of the model are distinguished by boundary conditions. The boundary condition restricts the selected NURBS control point to be at the specific position. The conditions are implemented by directly adjusting quantities in (8.14). For example, to fix the i-th NURBS point we use the following modification:

$$R_i = 0, \tag{8.15}$$

$$K_{ii} = 1, \quad K_{ij} = 0, \quad K_{ji} = 0, \quad \forall j \neq i. \tag{8.16}$$

The example is shown in Fig. 8.2a, where the garment is grasped at a single corner. The holding simulates the robotic grasping: the corner position, as well as orientation, are fixed by the gripper. The orientation is constrained by fixing the NURBS point next to the boundary as described in [Kiendl et al., 2009].

Contact Modelling

To generate a folding path, a contact with a folding desk needs to be modeled. The desk is assumed to be horizontal. Since the NURBS control points may not lie on the surface, the contact constraints are enforced on the integration points (Equation (8.11)) of the surface via the penalty method

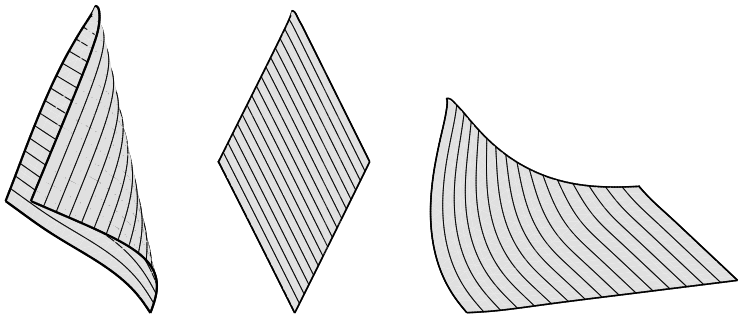

(a) Hanging (b) Hanging (c) In a partial contact with a desk

Figure 8.2: The model state examples of a garment held at a single corner. Three cases are distinguished: (a) the flexible ($\eta_b = 10^5\ \mathrm{m}^{-4}\,\mathrm{s}^2$) garment hanging in the air, (b) the stiff ($\eta_b = 10^4\ \mathrm{m}^{-4}\,\mathrm{s}^2$) garment hanging in the air, and (c) the state where the stiff garment is in a partial contact with a desk.

as described in [Kopacka et al., 2012]. The contact of the garment with the desk is frictionless. The example of the garment held by a corner with partial frictionless contact with the desk is shown in Fig. 8.2c. However, the friction is required for the folding process to be successful. The horizontal forces, which simulate the friction and are required for the path generation, are treated individually via boundary conditions.

8.2 Path Generation

A single arm is used for the folding. Thus, we omit an index in the grasping point notation, i.e. $\boldsymbol{x}_g \equiv \boldsymbol{x}_g^1$. The grasping point position is denoted:

$$\boldsymbol{x}_g(\tau) = \Big(x_g(\tau), \quad y_g(\tau), \quad z_g(\tau)\Big)^\top . \tag{8.17}$$

The force acting by the gripper in the grasping point is denoted

$$\boldsymbol{f}_g(\tau) = \Big(f_x(\tau), \quad f_y(\tau), \quad f_z(\tau)\Big)^\top . \tag{8.18}$$

Further, we specify a set of holding points - points which simulate the frictional forces. The holding points are selected garment parts, which are not expected to move while folding. Because we use NURBS parametrization, holding points are selected from a set of NURBS control points. The i-th holding point is denoted:

$$\boldsymbol{x}_h^i(\tau) = \Big(x_h^i(\tau), \quad y_h^i(\tau), \quad 0\Big)^\top , \tag{8.19}$$

where zero z-coordinate indicates that the point lies on the desk. For the path generation, all holding points are fixed to their initial positions. The holding forces $\boldsymbol{f}_h^i(\tau)$, required to hold the points in their positions, are analyzed later to check that the garment does not slip. The holding points for rectangular garment are shown in Fig. 8.3.

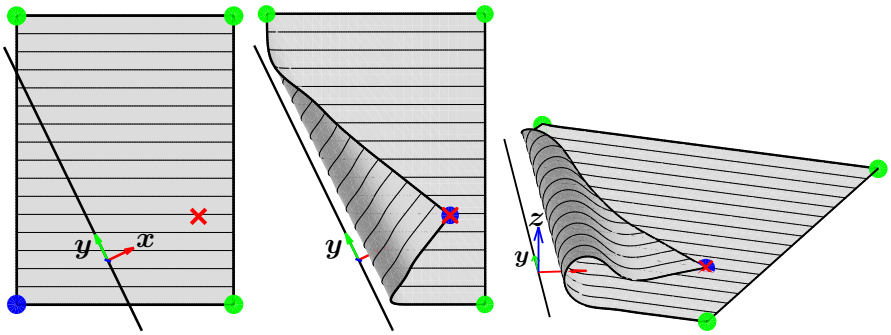

(a) Initial state (b) Folded state (c) Folded state, 3D view

Figure 8.3: The initial and folded state visualization. The holding points, simulating the frictional forces, are shown as the green circles. The blue circle represents the grasping point, and the red cross shows the final grasping point position. The folding line is shown in black.

8.2.1 Folded State

Our folding path generation procedure starts with the folded state computation. The folded state depends on the material properties, and we require it to evaluate the folded state touchdown point as shown in Fig. 8.4. That point is used to guide the path generation procedure to finish in the desired folded state. The touchdown point lies in the plane ϱ, which is perpendicular to the desk and passes through the points $\boldsymbol{x}_g(\tau_s)$ and $\boldsymbol{x}_g(\tau_e)$. Our path generation procedure requires the touchdown position to be equal to the folded state touchdown position. To achieve that, a point on the shell (denoted $\boldsymbol{x}_d(\tau)$) is computed such that:

- The position of the point in the folded state $\boldsymbol{x}_d(\tau_e)$ is not in contact with the desk.
- The point $\boldsymbol{x}_d(\tau_e)$ is the closest point to the folded state touchdown position.

Forcing the coordinate $z_d(\tau)$ to the value $z_d(\tau_e)$ causes the touchdown point position to be fixed.

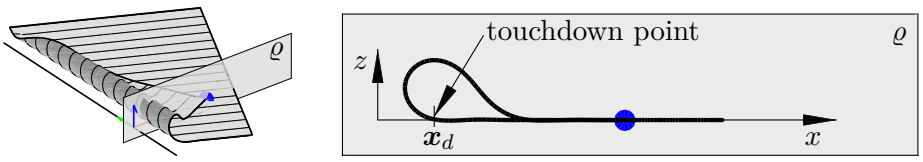

(a) The plane perpendicular to the folding line (b) The folded state touchdown point

Figure 8.4: The folded state touchdown point position. The point $\boldsymbol{x}_d$ is used to fix the touchdown point position.

Finding a state in a finite element analysis corresponds to solving a set of nonlinear equations. The solution is typically not unique. To select the

appropriate one, one has to specify the start state, which is close to the desired solution. In the case of folded state computation, we start from the spread garment state and follow a circular path, which is generated for the grasping point. The circular folding path is not optimal. However, it provides a correct estimation of the folded state if three conditions are satisfied:

- The holding forces $\boldsymbol{f}_h^i(\tau)$ could be arbitrarily large.
- There is no friction between the garment layers.
- The grasping point is constrained to the circular path during the whole movement and in the folded state too.

The first condition prevents the garment from slipping on the desk. The second condition enables sliding of the upper garment layer on the top of the lower garment layer. Sliding is required for the correction of the upper layer position after both layers touch each other. All conditions are satisfied in our model, and the folded state is visualized in Fig. 8.3.

With the computed folded state, we are able to determine which parts of the surface remain fixed. This information is used to verify that the selected holding points do not move while the path is executed. If the verification fails, new holding points are selected, and the folded state is recomputed. The new holding points are further away from the folding line in the x-axis direction.

8.2.2 Path Generation

Each garment state on the path is used to compute the gripper pose expressed by its orientation and the reference point position. The reference point position is equal to the grasping point position $\boldsymbol{x}_g(\tau)$. The gripper orientation is computed from the garment normal at the grasping point as shown in Fig. 8.5. In the real robotic grasping, the grasping point is not located at the gripper tip precisely. In such a case, the orientation computed from the tangent plane minimizes the influence of the gripper on the garment state.

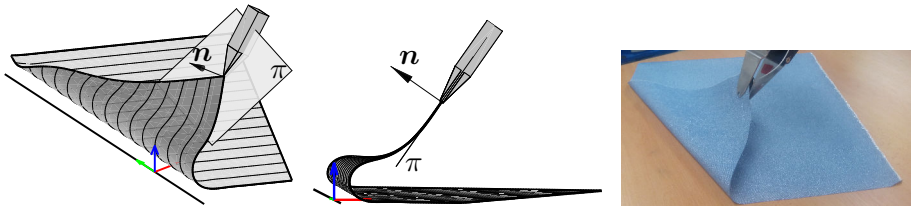

(a) (b) (c)

Figure 8.5: The gripper grasps the garment at the grasping point such that the gripper orientation is computed from the tangent plane π. The orientation around the plane normal $\boldsymbol{n}$ is arbitrary but has to be fixed for all states on the path. It corresponds to the azimuth relaxation.

The garment surface normal at the grasping point is not constrained during the garment state computation. It corresponds to a zero moment boundary condition. The real gripper with the orientation following the garment normal does not apply moment on the garment.

The grasping point is restricted to lie in the plane ϱ, which is perpendicular to the desk and passes through the points $\boldsymbol{x}_g(\tau_s)$ and $\boldsymbol{x}_g(\tau_e)$ (Fig. 8.4). With the coordinate system specified above, the boundary condition restricting the position to be on the plane is: $y_g(\tau) = y_g(\tau_s)$.

Different boundary conditions are used for different path *phases* to compute the coordinates $x_g(\tau)$ and $z_g(\tau)$. We divide the path into three phases such that the boundary conditions in a particular phase differ in a single variable only. This boundary condition is controlled by a control variable $\delta_j(\tau)$, which is a monotonic function of τ for the *Phase j*. The phases are shown in Fig. 8.6 and their boundary conditions are shown in Tab 8.1.

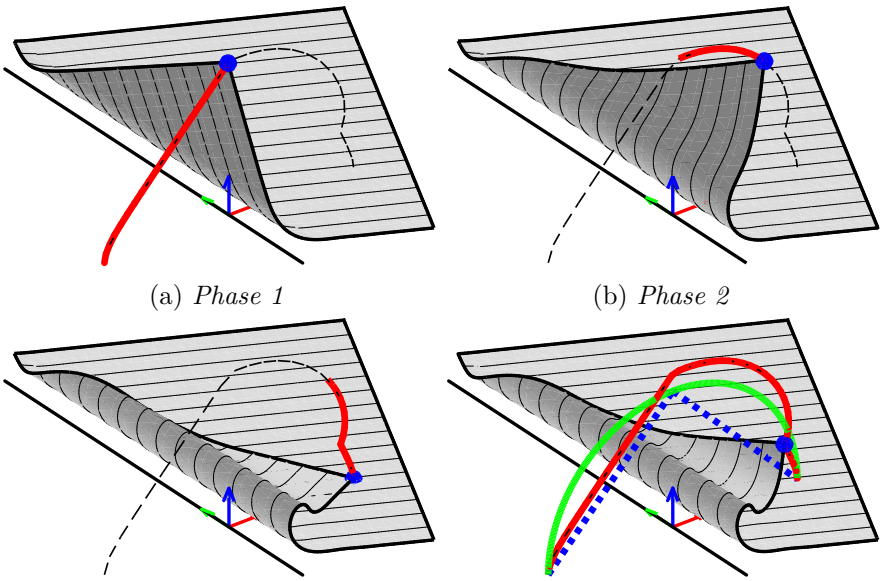

(a) *Phase 1* (b) *Phase 2*

(c) *Phase 3* (d) The whole path

Figure 8.6: The paths (bold red line) for the individual phases (a)-(c) with the visualization of the garment shape at the end of each phase, and the whole trajectory (d) with the state where the upper layer touches the lower layer for the first time. The blue and green curves (d) corresponds to the triangular and circular paths.

Phase 1

The *Phase 1* (Fig. 8.6a) starts from the garment initial state. The grasping point is lifted up with the force $f_x(\tau) = 0$. The control variable $\delta_1(\tau) \equiv z_g(\tau)$ controls the lifting and starts from the zero value. It increases linearly with τ until the touchdown point (Fig. 8.4) reaches its final position, which is evaluated on the folded state.

Phase 2

In *Phase 2* (Fig. 8.6b), the garment should rather bend than be lifted. To achieve that, the control variable is $\delta_2(\tau) \equiv x_g(\tau)$ and starts from the last

	Phase 1	*Phase 2*	*Phase 3*
f_x	0	×	×
f_y	×	×	×
f_z	×	×	×
x_g	×	$\delta_2(\tau)$	×
y_g	0	0	0
z_g	$\delta_1(\tau)$	×	$\delta_3(\tau)$
x_d	×	×	×
y_d	×	×	×
z_d	×	$z_d(\tau_e)$	$z_d(\tau_e)$
$\boldsymbol{f}_h$	×	×	×
$\boldsymbol{x}_h$	$\boldsymbol{x}_h(\tau_s)$	$\boldsymbol{x}_h(\tau_s)$	$\boldsymbol{x}_h(\tau_s)$

Table 8.1: The boundary conditions for the individual phases. The symbol × indicates that variable is not constrained. The variable δ_j parametrizes the *Phase j*.

value computed in *Phase 1*. The force $f_x(\tau)$ cannot be zero anymore. Instead, the touchdown point is fixed, which is achieved by constraining the position z_d. Note, that there is no additional force acting on the touchdown point. It is a purely geometrical constraint used to select the solution from the space of all admissible solutions. The control variable increases linearly with τ as long as $\Delta x_g > -\Delta z_g$, where Δ represents differences between subsequent states.

Phase 3

In *Phase 3* (Fig. 8.6c), the touchdown point is fixed as in the *Phase 2*. The control variable is $\delta_3(\tau) \equiv z_g(\tau)$, and the position x_g is not constrained. The phase ends when $\delta_3(\tau) = 0$, which corresponds to the folded state.

8.2.3 Folding Limitations

Our path generation procedure assumes that the folded state is stable, i.e. the garment remains fixed after the gripper releases the garment at the end of the folding. The stability means here that the garment remains in the same configuration as it was when the gripper stopped holding it. The stability is affected by the distance between the folding line and the initial grasping point position, and by the material properties. The stiffer material requires the greater folding line distance. The example of the instable folded state is shown in Fig. 8.7a.

Another example of the folding limitation is the motion of the garment towards the grasping point as shown in Fig. 8.7b. This garment movement results in the collapsed folded state. The collapse is caused by a movement of the part of the garment although the gripper remains static.

Both limitations have the origin in the physical behavior of the garment. It is not a limitation of our folding path generation method. The single arm folding path, which folds such garments, does not exist. The collapse could

be avoided if an additional robotic arm is used. However, the stability of the folding has not been analyzed yet, and it is the subject of our future work.

(a) Fold too small (b) Fold too big

Figure 8.7: Scenarios in which the folding is not possible. In the scenario (a), the folded state is not stable. After the gripper releases the garment, the garment returns into the spread state. The scenario (b) shows the collapsed state of the garment. It occur, when the garment edge measured between the gripper and the desk is too long. The forces acting on the garment causes that the edge moves towards the grasping point although the gripper remains static. It results in the collapsed state at the end.

8.3 Experiments

8.3.1 Comparison with the 1D Case

The first experiment compares the proposed method to the one-dimensional method presented in Chapter 7. If our two-dimensional method provides a folding path equal to the one-dimensional path for the same material, the accuracy measured in Chapter 7 will hold for our method too. The paths equality is expected since our model is a direct two-dimensional extension of the one-dimensional model. For the comparison, we generated paths for the 1 m long strips with the η_b set to value from 10^3 to 10^6 $\mathrm{m}^{-4}\,\mathrm{s}^2$. The folding line was placed into the middle of the strip.

In order to describe an inextensible material with the two-dimensional model, we set the *weight-to-membrane-stiffness-ratio* to the small value. The other material and geometrical properties were set to be equal to those in the one-dimensional path generation method. The generated paths are shown in Fig. 8.8. It can be seen that both methods provide similar results. Small differences are caused by the inextensible string approximation with a small weight-to-membrane-stiffness ratio. The two-dimensional path approaches the one-dimensional path with decreasing weight-to-membrane-stiffness ratio. However, due to the numerical imprecision, the inextensible string cannot be represented exactly by our model.

The generated path for the more flexible materials (bigger η_b) is closer to the triangular path. It is caused by approaching the infinite flexibility assumption, which was used to derive triangular path. The larger motion produced for stiffer materials in the *Phase 2* and *Phase 3* is caused by the selected boundary conditions for the phases. It is the motion, which is required to keep the touchdown point fixed.

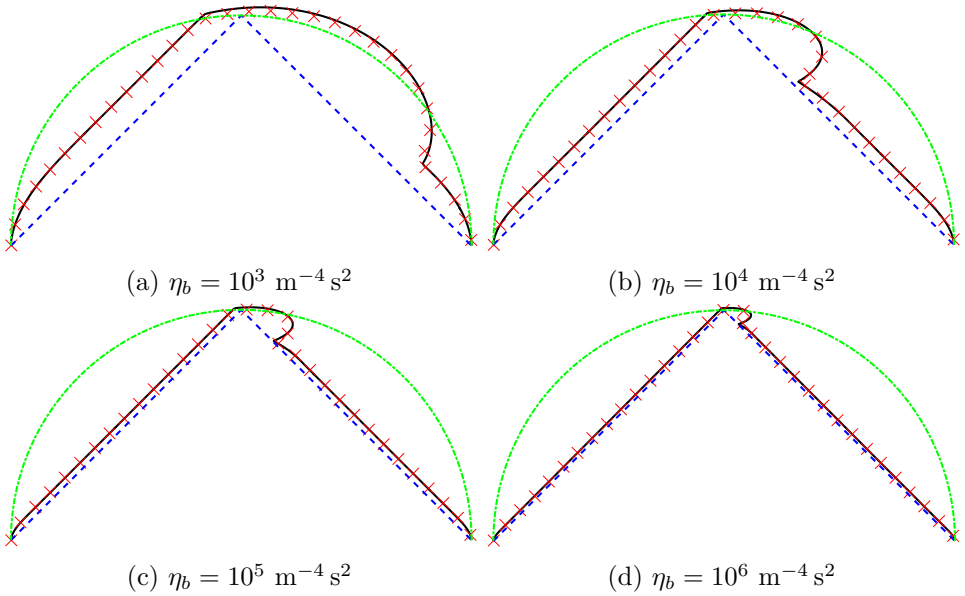

(a) $\eta_b = 10^3$ m^{-4} s^2 (b) $\eta_b = 10^4$ m^{-4} s^2

(c) $\eta_b = 10^5$ m^{-4} s^2 (d) $\eta_b = 10^6$ m^{-4} s^2

Figure 8.8: The comparison of trajectories for a narrow strip folding. The black line shows the path generated by the two-dimensional method. The red crosses visualize the path generated by the one-dimensional method. The triangular (blue) and circular (green) paths are shown as a reference.

8.3.2 Robotic Experiments

We used three garment samples of rectangular shape with dimensions: 500 × 500 mm. Three representatives of the commonly used fabrics were selected for the samples: lining, chanel, and denim. To measure the accuracy of the folding, we generated the folding paths for various folding lines. We parametrized the folding line by its distance to the initial corner position and by the angle between the x-axis and the garment axis of symmetry, which passes through the grasping point initial position as shown in Fig. 8.9a. The folding path was performed by the robot, and the positions of all corners in the folded state were measured. We used a melamine faced chipboard desk surface for all experiments. The same accuracy measurement was performed for the triangular and circular paths.

Material Properties Estimation

Our path generation method requires material properties to be known. We estimated the weight-to-stiffness-ratios η_b and η_m before folding by comparing manually and virtually folded garment. One corner of the rectangle was folded around the folding line with parameters: $\alpha = 45°$ and $d = 250$ mm (Fig. 8.9b). Two quantities were measured on the real folded state: the maximal height h_m and the overhang h_o as shown in Fig. 8.10. The relations between these quantities and the weight-to-stiffness-ratios were obtained by the simulation and are shown in Fig. 8.11. The measured and estimated quantities of our samples are shown in Table 8.2.

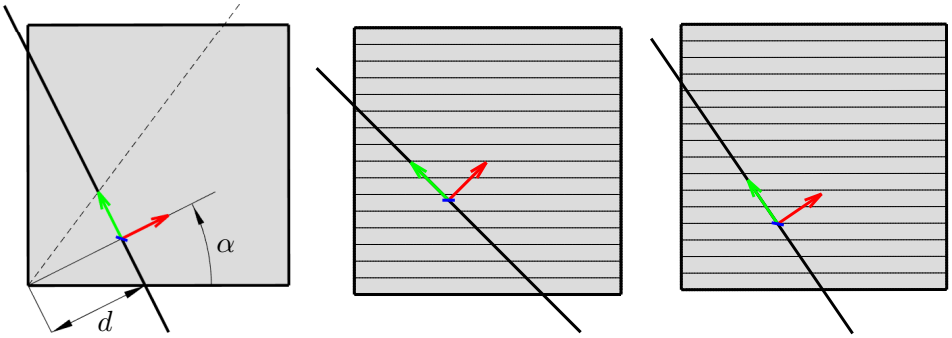

(a) Parametrization (b) $\alpha = 45°, d = 250$ mm (c) $\alpha = 35°, d = 220$ mm

Figure 8.9: The folding line parametrization (a), and the folding lines used in the experiments (b-c). The folding line is parametrized by its distance to the initial grasping point position, and by the angle α measured between the x-axis and the garment axis of symmetry (dashed line), which passes through the grasping point initial position.

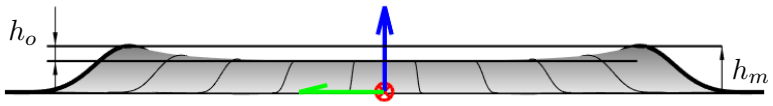

Figure 8.10: Material properties estimation from the folded state. The maximal height h_m and the overhang h_o are measured on the folded state and are used for the estimation. The view direction is incident with the direction of the x-axis.

Our material is further described by a Poisson's ratio ν. However, for the relatively small *weight-to-membrane-stiffness-ratios* of our samples, the Poisson's ratio has negligible influence on the generated path. We used constant value $\nu = 0$ for all materials in our experiment.

	h_m [mm]	h_o [mm]	η_m [$\mathrm{m}^{-2}\,\mathrm{s}^2$]	η_b [$\mathrm{m}^{-4}\,\mathrm{s}^2$]	ν[−]
lining	16.8	3.5	$2.51 \cdot 10^{-3}$	$2.60 \cdot 10^{5}$	0
chanel	27.7	6.6	$2.99 \cdot 10^{-3}$	$6.39 \cdot 10^{4}$	0
denim	33.8	1.3	$1.72 \cdot 10^{-4}$	$2.43 \cdot 10^{4}$	0

Table 8.2: The material properties of used materials.

Results

The robot performed folding for all materials from Tab. 8.2 for different folding line positions. Two folding line positions were tested: (a) with distance 250 mm and angle 45°, and (b) with distance 220 mm and angle 35°. The folding scenarios specification are shown in Fig. 8.9 and the generated paths are shown in Fig. 8.12. We measured displacements of all garment corners from their expected positions in the folded state. One corner corresponds to the grasping point, and the others were used as the holding points. Ideally, all displacements would be zero.

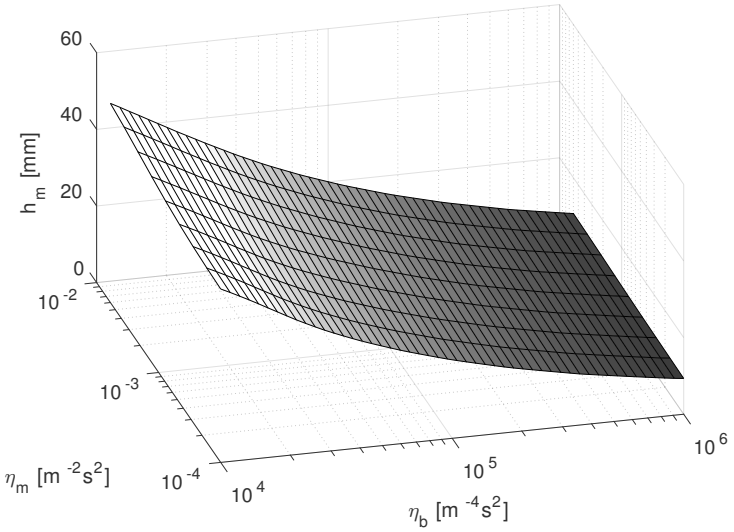

(a) Maximal height

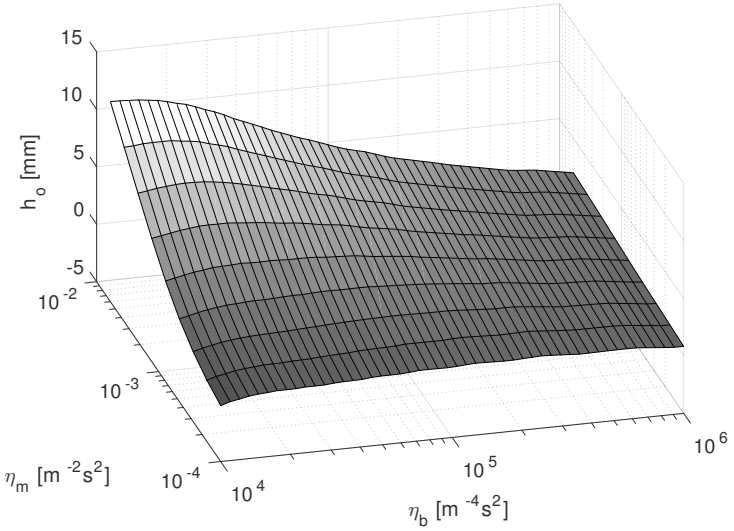

(b) Overhang

Figure 8.11: The relations between the weight-to-stiffness-ratios η_m and η_b and the maximal height h_m and the overhang h_o measured on the folded state.

The measured displacements of the grasping point from its expected positions are shown in Table 8.3. Our path outperformed the triangular and circular paths in all experiments because the displacement caused by our path was smaller than the displacement caused by other paths. The displacement of the triangular path is higher for stiffer material which corresponds to the violation of the infinite flexibility assumption. The circular path shows the opposite relation: the displacement is lower for the stiffer material.

The holding points displacement was zero for the triangular path as well as for our path. The friction between the garment and the desk was thus sufficient. The displacement for the circular path was non-zero which was

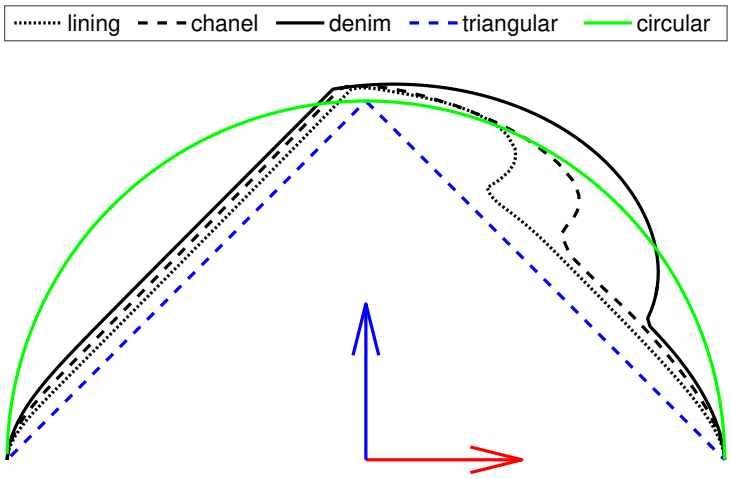

(a) $\alpha = 45°, d = 250$ mm

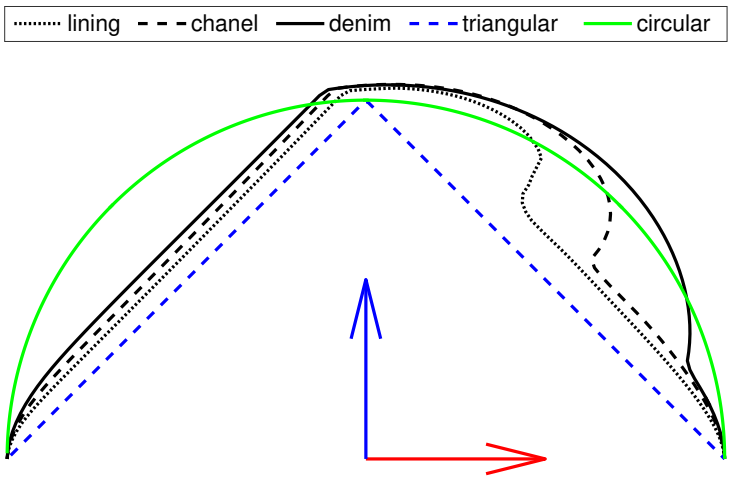

(b) $\alpha = 35°, d = 220$ mm

Figure 8.12: The paths used in the experiment for the first (a) and the second (b) scenario. The cut in the plane $y = 0$ is visualized.

caused by the garment slipping. The holding point displacements for the circular path was less then 10 mm in all experiments.

8.3.3 Generated Paths Discussion

All generated paths (Fig. 8.12) start and finish in the same point. Ideally, considering no friction between the garment layers and with infinite friction between the garment and the surface, the grasping point displacement would be zero. However, realistic scenario results in a non zero displacement.

In a case of the triangular path, both garment layers touch each other sooner than required as shown in Fig. 8.13a. Since the touchdown point is not in its final position, the consequent motion will pull it towards the final position. In case of no friction between layers, the pulling ends in the final position. In a realistic scenario, several cases could be observed: (a) the

Folding Line	Material	Grasping point displacements in [mm] Triangular x	Triangular y	Circular x	Circular y	Proposed x	Proposed y
$\alpha = 45°$ $d = 250$ mm	lining	20	0	-62	10	3	1
	chanel	16	2	-25	1	3	0
	denim	26	7	-7	4	-2	0
$\alpha = 35°$ $d = 220$ mm	lining	20	4	-40	22	10	0
	chanel	21	1	-19	4	1	3
	denim	28	5	-5	3	-3	-2

Table 8.3: The measured grasping point displacements from the expected position. Two folding line positions were tested for three different materials: the lining, chanel, and denim.

garment will slip on the table; (b) the top layer will slide on the bottom layer; (c) the top layer will stretch (no touchdown point movement); (d) the layers will wrinkle; (e) or the combination of any of above.

The circular path shows an opposite behavior. The touchdown point position after both layers touch each other is behind its final position (Fig. 8.13b). The layers sliding is required to correct its position.

The virtual prediction of the grasping point displacement is a difficult task in the case of a layer sliding. Without accurate prediction, the planned path does not result in a zero grasping point displacement. The avoidance of the touchdown point movement simplifies the prediction task significantly. Our boundary conditions are chosen such that the touchdown point position is fixed. Thus, our path outperformed the triangular and the circular paths in the real folding experiment.

8.3.4 Holding Forces Analysis

In the performed robotic experiments only the circular path results into the garment slipping. The slipping is caused by large force acting on the holding points. In order to compare the garment slipping tendency for different paths, we estimated the required holding force by simulation for the scenario with $\alpha = 45°$. The estimated forces are shown in Fig. 8.14. The holding forces in the *Phase 1* for our path are smaller than the corresponding forces for the triangular and circular path. It is a consequence of the zero x-component of the force acting by the gripper.

The holding forces in the *Phase 2* and *Phase 3* are almost equal for all paths. It is caused by missing friction modeling between the touching layers of the garment. The triangular and circular paths result in the sliding of the top layer on the bottom layer. The real force would be thus higher. Our path does not result in the top layer sliding and thus the simulated force would correspond to the real one. The smaller holding forces of our path reduce the risk of garment slipping.

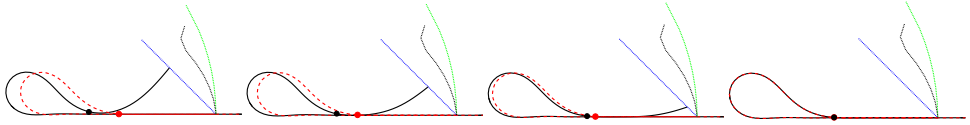

(a) Triangular path - the top layer slides as gripper pulls the garment

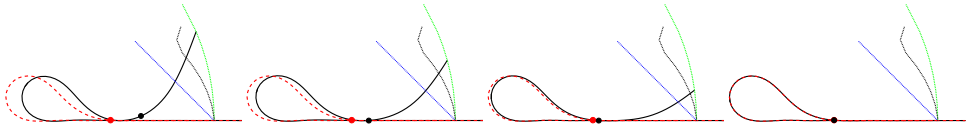

(b) Circular path - the top layer slides as gripper pushes the garment

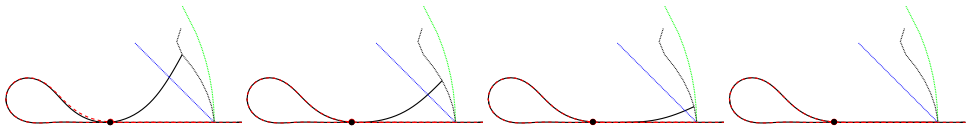

(c) Proposed path - the top layer does not slide

Figure 8.13: The evolution of ideal states for the (a) triangular, (b) circular, and (c) proposed paths. The evolution is shown for the cut in the plane $y = 0$ for the scenario with $\alpha = 45°$. The final garment state (red dashed line) is shown together with actual garment state (black line). The red and black circles are fixed point on the garment used to indicate the garment layers sliding. The evolution shows the sliding of the top layer on the bottom layer due to the absent friction modeling. The sliding is visualized by black point moving towards the fixed red point. In reality, the sliding is constrained by the friction, which results in an inaccurate fold - i.e. the grasping point displacement is non zero.

8.4 Conclusion

This chapter extends the strip path generation method to two-dimensional shapes. The two-dimensional shell model was used, and the boundary conditions were designed for the new model. The states in static equilibrium were found, and the folding path was computed from these states.

We demonstrated the accuracy of our method by: (a) comparing with the one-dimensional method in case of the narrow strips, and (b) by real robotic rectangular garment folding. In the former case, our generated path is almost identical to the path designed in Chapter 7, which was experimentally confirmed to be accurate. The latter case demonstrated the accuracy for folding scenarios, which are not possible with the one-dimensional method. Our experiments confirmed the accuracy of the generated path and showed that our method outperforms the triangular [van den Berg et al., 2010] and circular [Petrík et al., 2015] paths.

The reported work designed a folding path for a garment of given shape and material properties. The shape can be easily measured automatically by e.g. a camera before the folding is performed. On the other hand, the material properties are measured manually by the operator. The next chapter proposes the algorithm for the estimation of the material properties in the course of folding.

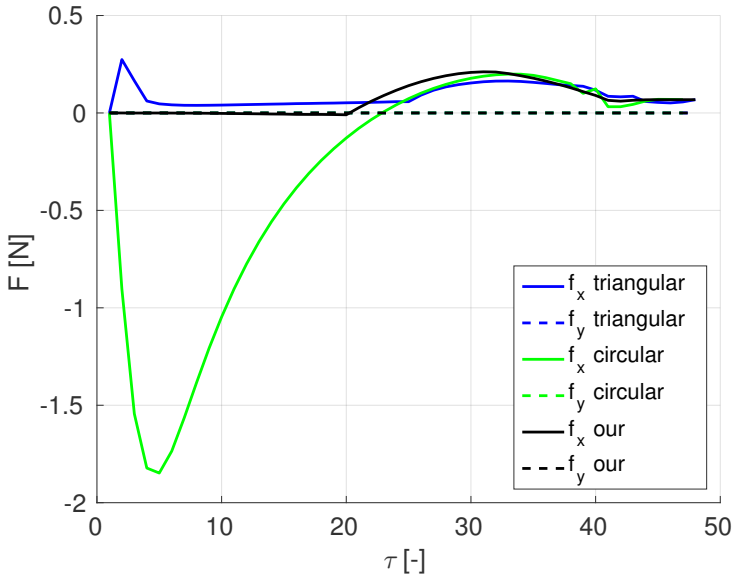

(a) Holding point 1

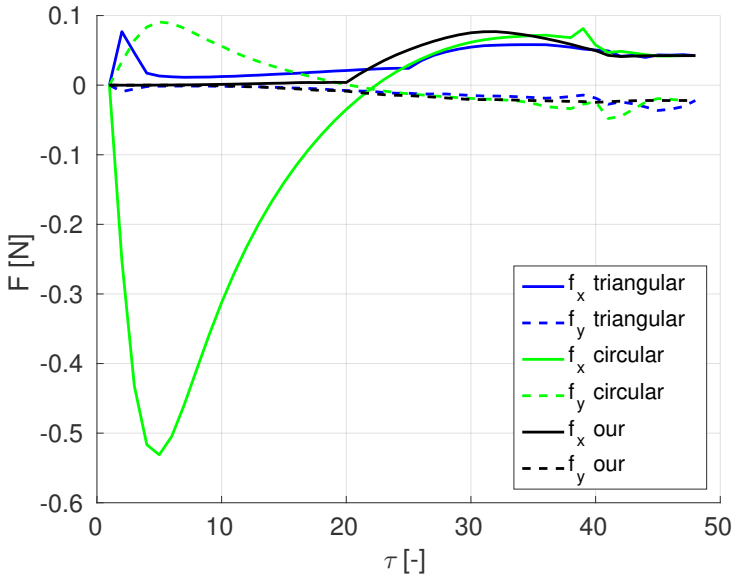

(b) Holding point 2

Figure 8.14: Holding points forces for the folding scenario with $\alpha = 45°$. The holding point 1 stands for the corner, which is opposite to the grasping point. The holding point 2 represents one of the other corners. Due to the zero folding line angle, the other holding points have the same forces except that the y-forces have opposite direction.

Chapter 9

Fabric Properties Estimation

All presented physics-based methods require the material properties to be known. The state-of-the-art methods estimate the properties manually before the folding is performed. To the author knowledge, the automatic estimation of the material properties for the folding purposes has not been addressed yet.

This chapter describes the automatic material properties estimation for the physics-based model, which we used for the folding path design in Chapter 8. The estimation is based on the measurements acquired by the 2D laser range finder. It measures the shape of the garment in a single plane cut. The measurement is used to formulate the optimization task for the material properties estimation. The estimation itself is done in the course of folding. It provides a rough estimation at the beginning of the folding, which is, however, accurate enough to prevent the garment slipping on the slippery folding desk. The estimation is refined iteratively with new measurements obtained. We demonstrate the proposed estimation procedure using a robotic testbed with the laser range finder shown in Fig. 9.1. In a real household scenario, a humanoid robot capable of measuring a point cloud (e.g. a PR2 robot) can be used.

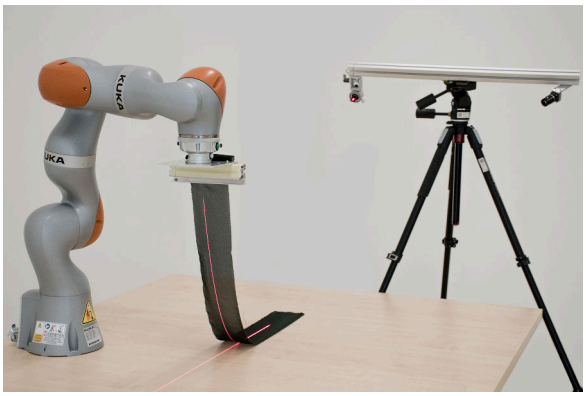

Figure 9.1: Robotic testbed used for the demonstration of the proposed estimation algorithm. The testbed consists of a single-arm *KUKA LBR iiwa 7* robot and a laser range finder. The range finder consists of the camera and the laser plane projector mounted on a tripod. The robot, camera, and projector are calibrated with respect to each other.

9.1 Garment Model

The garment model in this chapter is the same as the model used for folding path design in the Chapter 8. Let us denote the garment model state with a gripper grasping the known part of the garment (e.g. a corner of a towel) as:

$$\mathcal{S}(T_g, \eta_m, \eta_b, \nu)\,, \tag{9.1}$$

where T_g is a gripper pose, η_m is *weight-to-membrane-stiffness-ratio*, η_b is *weight-to-bending-stiffness-ratio*, and ν is Poisson's ratio. Parameters η_m, η_b, and ν represent material properties of the garment. The model state is represented by a garment surface geometry position, i.e. the function (9.1) returns a garment surface for the given gripper pose and material properties.

9.1.1 Path Design

The design of the folding path requires the material properties to be known in advance. The path is computed from the sequence of garment states, which is found as described in Chapter 8. The individual garment states are constrained by a partially known gripper pose. The unknown pose parameters are computed such that the folding constraints are satisfied. For example, at the beginning of the folding, the gripper z-coordinate is fixed while the rest of the gripper pose is computed such that horizontal force is minimal. It results in a state:

$$s_i = \mathcal{S}_1(z_i, \eta_m, \eta_b, \nu), \tag{9.2}$$

where z_i represents the gripper pose z-coordinate. The parameter z_i increases monotonically with time resulting in the garment lifting. The function (9.2) represents the *Phase 1*.

The folding path for the robot is computed from the found sequence of states. We denote the operation of the gripper pose computation from the know state s as:

$$T_g = P(s). \tag{9.3}$$

Applying the operator to all states results in the folding path as visualized in Fig. 9.2.

9.1.2 Material Properties Influence

The garment model depends on three properties. The first property, *weight-to-membrane-stiffness-ratio* η_m, represents the elasticity of the garment. During the folding, the garment is stretched by its own weight only. However, typical garments are small and exhibit little to none stretch during the folding. For example, the stretch of our 1 m long strips of different materials used in the experiments was less than 3 mm, when stretched by its own weight. We can thus approximate the *weight-to-membrane-stiffness-ratio* η_m by a small value,

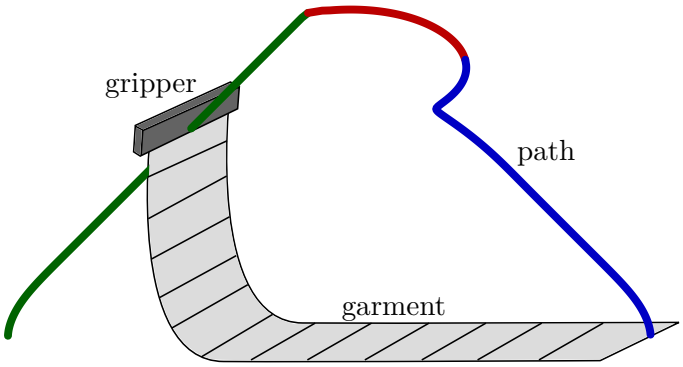

Figure 9.2: The folding path divided into individual phases: *Phase 1* is green, *Phase 2* is red, and *Phase 3* is blue. The garment model (gray) is divided into the elements according to [Kiendl et al., 2009].

which represents almost inextensible material. Such an approximation has a negligible influence on the designed folding path.

Poisson's ratio ν represents the amount of material compression in a direction perpendicular to the garment extension direction. With the small *weight-to-membrane-stiffness-ratio* η_m there is almost none extension, which results in almost none material compression in the perpendicular direction. The influence of Poisson's ratio on the folding is thus negligible too.

9.2 Properties Estimation

The estimation is done during the *Phase 1* of the folding path. As a robot is lifting the garment, new measurements are obtained and the estimation accuracy is improved.

At the beginning, the garment is lifted into the gripper pose T_0 computed from the garment state s_0:

$$s_0 = S_1(z_0,\, \eta_m,\, \eta_b^0,\, \nu), \tag{9.4}$$

$$T_0 = P(s_0), \tag{9.5}$$

where S_1 represents *Phase 1* and an operator $P(\cdot)$ stands for the gripper pose computation from the garment state. The value η_b^0 is an initial guess for the *weight-to-bending-stiffness-ratio* η_b. Properties η_m and ν are constant.

After the robot reaches the computed pose T_0, the new measurement of the garment shape Z_0 is obtained. The estimation assumes the measurement in form of the point cloud consisting of points: $\boldsymbol{z}_i$, $i = 1, \ldots, N$. Based on the measurement, the new value for η_b is estimated:

$$\eta_b^1 = \arg\min_{\eta_b} J(T_0, Z_0, \eta_b), \tag{9.6}$$

where $J(\cdot, \cdot, \cdot)$ is a cost function defined as:

$$J(T, Z, \eta_b) = \frac{1}{2} \sum_{\boldsymbol{z} \in Z} d(\boldsymbol{z}, S(T,\, \eta_m,\, \eta_b,\, \nu))^2, \tag{9.7}$$

with a function $d(\boldsymbol{z}, S(\cdot))$ representing the Euclidean distance between the garment surface and measured point. In our implementation, the position of the NURBS surface was evaluated on a fine rectangular grid, and the closest position was used. The new gripper pose T_1 is obtained with the estimated η_b^1 following Equations (9.4, 9.5). The process continues iteratively during the whole *Phase 1.*

The presented estimation process requires the gripper position to be known precisely. In practice, this is however unfeasible due to the robot accuracy. In order to make the estimation process feasible in the presence of this uncertainty, we relaxed the constraints by adding an unknown gripper position offset into the optimization process. This changes the cost function (9.7) into:

$$J(T, Z, \eta_b, T_\delta) = \frac{1}{2} \sum_{\boldsymbol{z} \in Z} d(\boldsymbol{z}, S(TT_\delta,\, \eta_m,\, \eta_b^0,\, \nu))^2, \tag{9.8}$$

where T_δ represents the unknown translation matrix. The properties being estimated are thus: η_b and T_δ. The complete algorithm for iterative parameters estimation is shown in Algorithm 1.

Data: η_m, ν, η_b^0, Δz_g
Result: η_b, T_δ
$T_\delta^0 \leftarrow$ identity
$z_g \leftarrow 0$
for $i \leftarrow 0$ **to** *number of iterations* **do**
  $z_g \leftarrow z_g + \Delta z_g$
  $s_i \leftarrow S_1(z_g,\, \eta_m,\, \eta_b^i,\, \nu)$
  $T_i \leftarrow P(s_i)$
  move robot to pose T_i
  $Z_i \leftarrow$ obtain a new measurement
  $\eta_b^{i+1}, T_\delta^{i+1} \leftarrow \underset{\eta_b, T_\delta}{\arg\min}\, J(T_i, Z_i, \eta_b, T_\delta)$
end

Algorithm 1: Iterative material properties estimation

To summarize, the robot follows the path designed from the current estimate of the material property. The new material property is estimated based on the obtained measurement. This estimation is used to update the following path and the process continues repeatedly. The estimation is rough at the beginning of the folding. However, the paths for a typical range of material property values do not differ significantly at the beginning of the folding. Thus, the garment slipping should not occur. The estimation improves with the garment being lifted. At the end of the *Phase 1* the estimation should be sufficient to fold the garment.

9.3 Experiments

9.3.1 Testbed Description

A single-arm robot *KUKA LBR iiwa 7* was used for the garment manipulation purposes. For the point cloud measurement, we used a monocular camera and a laser plane projector. The robot, camera and projector were calibrated each to other. It allows us to measure the garment shape in the projected plane. The real testbed and the schematic visualisation are shown in Fig. 9.1 and Fig. 9.3.

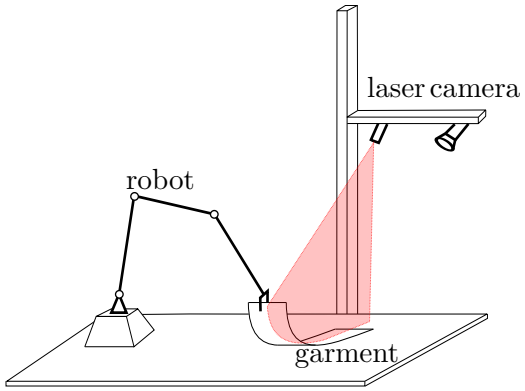

Figure 9.3: Schematic visualisation of the robotic testbed. The robot, laser plane projector, and camera are calibrated with respect to each other. It allows us to measure the garment surface shape.

9.3.2 Manual Reference Properties Measurement

To verify the estimation algorithm, we used narrow fabric strips of different materials. We used single layer materials from the whole spectrum of weaving fabrics used for garment manufacturing. The reference strips *weight-to-bending-stiffness-ratio* η_b are not known a priori. To estimate them, we used a free fold test as described in Chapter 7. The estimation is based on the maximal height h_m of the manually folded garment. We denote the ratio estimation as:

$$\eta_b = \eta_b(h_m). \tag{9.9}$$

Besides the material properties used in our model, the other properties, which reflect the recent history of the particular patch of the fabric such as ironing, washing, bending, storing conditions, moisture content influence the actual bending shape during folding. Therefore, we measured the height multiple times with different free fold test locations and we estimated the reference ratio in a statistical manner. Measured values h_m together with an estimated mean μ_h and $\pm 2\sigma_h$, where σ_h stands for standard deviation, are shown in Fig. 9.4. We visualize the material property uncertainty with

the 4σ interval. From the estimated height statistical values μ_h and σ_h, the expected values of η_b are computed as shown in Tab. 9.1 and Fig. 9.5.

Material	μ_h [mm]	$2\sigma_h$ [mm]	$\eta_b(\mu_h)$ [$m^{-4}\,s^2$]	$\eta_b(\mu_h \pm 2\sigma_h)$ [$m^{-4}\,s^2$]
coating	20	3.4	$8.5 \cdot 10^3$	$5.1 \cdot 10^3$ - $1.6 \cdot 10^4$
chanel	28	3.9	$2.6 \cdot 10^3$	$1.7 \cdot 10^3$ - $4.2 \cdot 10^3$
twill	19	4.6	$8.9 \cdot 10^3$	$4.5 \cdot 10^3$ - $2.3 \cdot 10^4$
denim	23	3.1	$5.2 \cdot 10^3$	$3.4 \cdot 10^3$ - $8.3 \cdot 10^3$
terry cloth	25	2.8	$3.9 \cdot 10^3$	$2.8 \cdot 10^3$ - $5.7 \cdot 10^3$
plain weave	25	3.4	$4.0 \cdot 10^3$	$2.7 \cdot 10^3$ - $6.4 \cdot 10^3$
herringbone	21	2.5	$6.5 \cdot 10^3$	$4.6 \cdot 10^3$ - $9.7 \cdot 10^3$
georgette	15	1.7	$2.4 \cdot 10^4$	$1.6 \cdot 10^4$ - $4.1 \cdot 10^4$
chiffon	13	2.3	$3.5 \cdot 10^4$	$1.8 \cdot 10^4$ - $1.5 \cdot 10^5$
wool suiting	18	1.8	$1.1 \cdot 10^4$	$8.0 \cdot 10^3$ - $1.5 \cdot 10^4$

Table 9.1: Reference material properties.

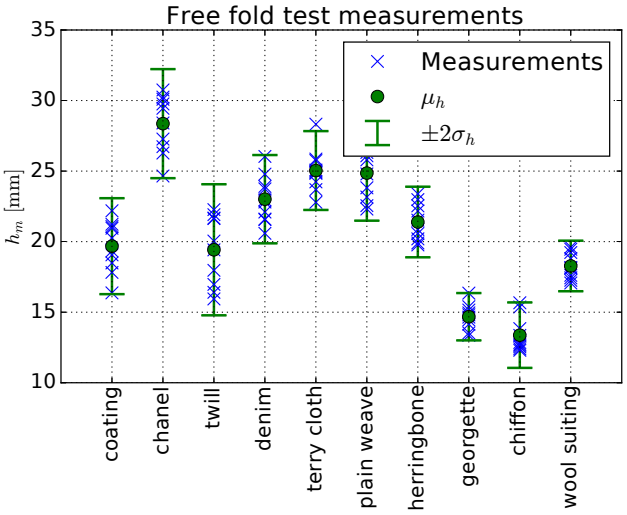

Figure 9.4: Measurements for the free fold test. The mean value and standard deviation are computed from the height measurements.

9.3.3 Strips Properties Estimation

We have observed, that the η_b value for the wide range of materials lies in the range from 10^2 to 10^6 $m^{-4}\,s^2$. We chose an initial guess for the estimated value to be $\eta_b^0 = 10^2$ $m^{-4}\,s^2$. The initial guess value does not seem to influence the resulting estimate. The value of η_b is then updated iteratively following Algorithm 1. The whole *Phase 1* is used, and we divided it into 10 iterations. The values estimated in the last iteration for all tested materials are shown in Fig. 9.5. The path followed by the gripper and the reference path for

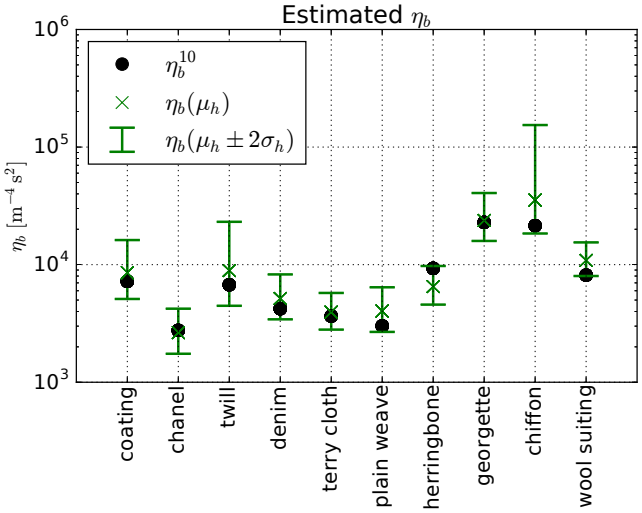

Figure 9.5: The reference η_b estimated by the free fold test (green cross) and the value estimated in the last iteration of the proposed algorithm (black dot). The visualized range represents uncertainty of the reference value estimation.

the selected garment are shown in Fig. 9.6. The estimations for all tested garments are shown in Fig. 9.7.

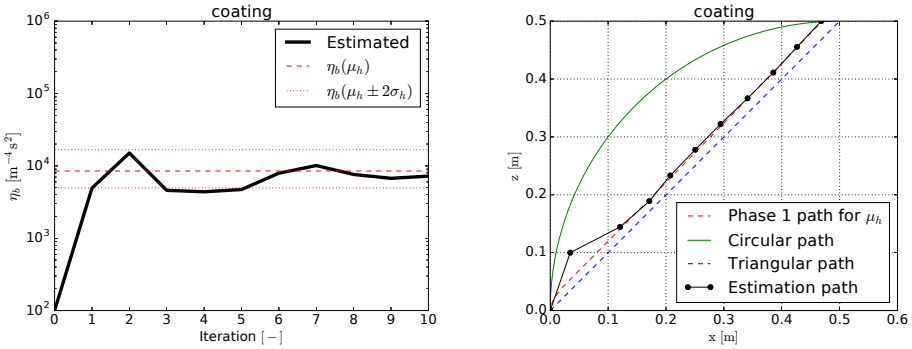

Figure 9.6: The iterative update of the *weight-to-bending-stiffness-ratio* η_b and the gripper position for the selected garment. The red dashed line represents the reference values estimated from the free fold test. The uncertainty of the estimation is represented by red dotted lines. The triangular (blue, dashed) and circular (green) paths are shown as a reference.

The results shown in Fig. 9.7 indicate that the estimation is improved as the garment is lifted. The initial rough estimation was however sufficient to prevent the garment from slipping. We did not observe any slipping during the whole experiment. The value estimated in the last iteration (Fig. 9.5) for all materials was in a range of $\pm 2\sigma_h$.

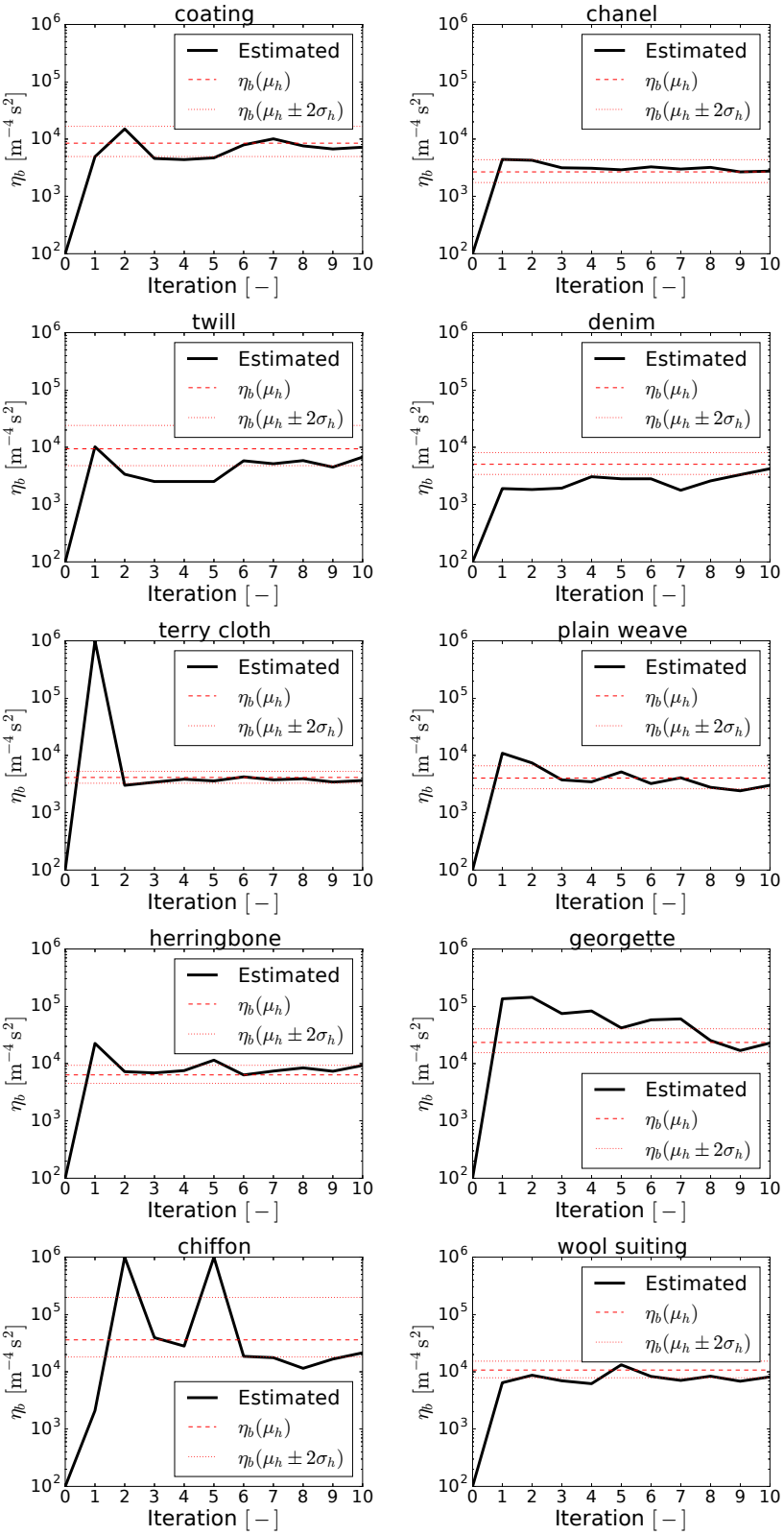

Figure 9.7: The iterative estimation of η_b for all tested materials.

9.4 Conclusion

We presented the algorithm for the estimation of the material properties for the robotic garment folding purposes. The estimation was performed iteratively in the course of folding while updating the folding path. The formulated optimisation task uses the measurement of the garment shape, provided in the form of a point cloud.

We demonstrated the accuracy of our approach experimentally using the robotic testbed with the laser range finder. The 1 m long garment strips of various materials were tested.

The main contribution of the chapter is the automatic estimation of the material properties in the course of folding. The proposed method replaces the manual estimations performed by an operator before the folding. Using our algorithm, the robotic garment folding can be fully automatic and accurate at the same time.

Chapter 10

Conclusion

In this thesis, the path generation methods for the robotic garment folding were studied. This work contributed to the state-of-the-art by path generation method, which folds the garment accurately. The method finds the garment states which are in a static equilibrium of forces such that the folding constraints are satisfied. In the following, the novel contributions of each chapter are briefly summarized.

Chapter 5 proposed circular path as an alternative to the state-of-the-art triangular folding path. It has been demonstrated that the circular path is more suitable for the real-life garments folding. The robotic experiments showed the folding accuracy improvement with circular path. However, both geometrical paths were derived from the extreme underlying physics-based garment models. Our experiments suggested that the path which folds typical garments more accurately should depend on the fabric material properties.

Chapter 7 explored the one-dimensional physics-based model for the purpose of robotic narrow strip folding. The model was parametrized by a single property representing the bending stiffness. The boundary value problem was solved to find the garment state in static equilibrium. The path was computed from the sequence of states. The designed path prevents the garment from slipping when folded on the low friction surface, which results in a better folding accuracy. In robotic experiments, the material property was estimated in advance of the folding manually by an operator. The proposed path outperformed the triangular and circular paths in terms of accuracy.

Chapter 8 extended the proposed one-dimensional model to two dimensions. The method respects the garment shape and material properties by modeling the garment as an elastic shell. We demonstrated the accuracy of the proposed method by: (a) comparing with the one-dimensional method in a case of the one-dimensional strips, and (b) by real robotic garment folding. In the former case, the proposed generated path is almost identical to the one-dimensional method, which was experimentally confirmed to be accurate. The latter case demonstrated the accuracy for folding scenarios, which are not possible with the one-dimensional method. Our experiments confirmed the accuracy of the generated path and showed that the proposed method outperforms the triangular and circular paths.

Chapter 9 presented the algorithm for the estimation of the material properties for the two-dimensional garment model. The estimation is done iteratively in the course of folding while updating the folding path. The formulated optimisation task uses the measurement of the garment shape, provided in the form of a point cloud. It replaces the state-of-the-art estimation technique, which was done manually by an operator. We demonstrated the accuracy of our approach experimentally using the robotic testbed with the laser range finder. The 1 m long garment strips of various materials were tested.

10.1 Ideas for Future Work

The thesis studied the path generation methods for one-layer garments only. In the future work, the proposed approach should be tested with multi-layers garments too. Moreover, the proposed shell-based approach was limited to single arm folding. The multiple arms folding together with the determination of grasping points locations is subject of our future work.

Chapter 8 shows two folding limitations, which have the origin in physics. We would like to predict the situation in which the limiting cases occur by simulation. These limitations could be avoided by using other arms. We believe that the analysis of the shell model will provide the prediction for the other arms locations.

The folding in this thesis was assumed to be slow. Thus, the dynamics effects could be neglected. In order to increase the folding speed, the dynamics needs to be considered in the model too.

Bibliography

[clo, 2015] (2012–2015). Cloth Perception and Manipulation - CloPeMa. `http://clopema.eu/`. 7th Framework Programme for Research and Technological Development.

[Alenyà Ribas et al., 2012] Alenyà Ribas, G., Ramisa Ayats, A., Moreno-Noguer, F., and Torras, C. (2012). Characterization of textile grasping experiments. In *Proc. ICRA Workshop on Conditions for Replicable Experiments and Performance Comparison in Robotics Research*, pages 1–6.

[Baraff and Witkin, 1998] Baraff, D. and Witkin, A. (1998). Large steps in cloth simulation. In *Proceedings of the 25th annual conference on Computer graphics and interactive techniques*, pages 43–54. ACM.

[Bartels et al., 1987] Bartels, R. H., Beatty, J. C., and Barsky, B. A. (1987). *An introduction to splines for use in computer graphics and geometric modeling*, chapter Bézier Curves. Morgan Kaufmann.

[Bellman and Kalaba, 1965] Bellman, R. E. and Kalaba, R. E. (1965). Quasilinearization and nonlinear boundary-value problems. Technical report, RAND Corporation, Santa Monica.

[Bender et al., 2015] Bender, J., Muller, M., and Macklin, M. (2015). Position-based simulation methods in computer graphics. *EUROGRAPHICS Tutorial Notes*.

[Beneš et al., 2014] Beneš, P., Petrík, V., Šika, Z., and Valášek, M. (2014). Calibration using two laser trackers leica AT901 MR. Technical report, Czech Technical University in Prague.

[Chen and Govindaraj, 1995] Chen, B. and Govindaraj, M. (1995). A physically based model of fabric drape using flexible shell theory. *Textile Research Journal*, 65(6):324–330.

[Chen and Govindaraj, 1996] Chen, B. and Govindaraj, M. (1996). A parametric study of fabric drape. *Textile Research Journal*, 66(1):17–24.

[Cirak et al., 2000] Cirak, F., Ortiz, M., and Schroder, P. (2000). Subdivision surfaces: a new paradigm for thin-shell finite-element analysis. *Int. J. Numerical Methods in Engineering*, 47(12):2039–2072.

[Cirio et al., 2014] Cirio, G., Lopez-Moreno, J., Miraut, D., and Otaduy, M. A. (2014). Yarn-level simulation of woven cloth. *ACM Transactions on Graphics (TOG)*, 33(6):207.

[Cockshott and Renaud, 2016] Cockshott, P. and Renaud, K. (2016). Humans, robots and values. *Technology in Society*, 45:19 – 28.

[Collier et al., 1991] Collier, J. R., Collier, B. J., O'Toole, G., and Sargand, S. (1991). Drape prediction by means of finite-element analysis. *J. Textile Institute*, 82(1):96–107.

[Corona et al., 2017] Corona, E., Alenyà, G., Gabas, A., and Torras, C. (2017). Active garment recognition and target grasping point detection using deep learning. *Pattern Recognition*.

[Cusumano-Towner et al., 2011] Cusumano-Towner, M., Singh, A., Miller, S., O'Brien, J. F., and Abbeel, P. (2011). Bringing clothing into desired configurations with limited perception. In *Proc. IEEE Int. Conf. on Robotics and Automation (ICRA)*, pages 3893–3900.

[Dixit and Mali, 2013] Dixit, A. and Mali, H. S. (2013). Modeling techniques for predicting the mechanical properties of woven-fabric textile composites: A review. *Mechanics of Composite Materials*, 49(1):1–20.

[Doumanoglou et al., 2014] Doumanoglou, A., Kargakos, A., Kimand, T.-K., and Malassiotis, S. (2014). Autonomous active recognition and unfolding of clothes using random decision forests and probabilistic planning. In *Proc. IEEE Int. Conf. on Robotics and Automation (ICRA)*, pages 987–993.

[Doumanoglou et al., 2016] Doumanoglou, A., Stria, J., Peleka, G., Mariolis, I., Petrík, V., Kargakos, A., Wagner, L., Hlaváč, V., Kim, T.-K., and Malassiotis, S. (2016). Folding Clothes Autonomously: A Complete Pipeline. *IEEE Transactions on Robotics*, 32(6):1461–1478.

[Drigalski et al., 2017] Drigalski, F. V., Yoshioka, D., Yamazaki, W., Cho, S. G., Gall, M., Eljuri, P. M. U., Hoerig, V., Ding, M., Takamatsu, J., Ogasawara, T., and Beltran, J. (2017). Naist openhand m2s: A versatile two-finger gripper adapted for pulling and tucking textile. In *2017 First IEEE International Conference on Robotic Computing (IRC)*, pages 117–122.

[Eischen et al., 1996] Eischen, J. W., Deng, S., and Clapp, T. G. (1996). Finite-element modeling and control of flexible fabric parts. *IEEE Computer Graphics and Applications*, 16(5):71–80.

[Estevez et al., 2016] Estevez, D., Victores, J. G., Morante, S., and Balaguer, C. (2016). Towards robotic garment folding: A vision approach for fold detection. In *2016 International Conference on Autonomous Robot Systems and Competitions (ICARSC)*, pages 188–192.

[Gan et al., 1995] Gan, L., Ly, N., and Steven, G. (1995). A study of fabric deformation using nonlinear finite elements. *Textile Research Journal*, 65(11):660–668.

[Hamajima and Kakikura, 2000] Hamajima, K. and Kakikura, M. (2000). Planning strategy for task of unfolding clothes. *Robotics and Autonomous Systems*, 32(2):145–152.

[Hou et al., 2017] Hou, Y. C., Sahari, K. S. M., Weng, L. Y., How, D. N. T., and Seki, H. (2017). Particle-based perception of garment folding for robotic manipulation purposes. *International Journal of Advanced Robotic Systems*, 14(6):1729881417738727.

[Hu and Kita, 2015] Hu, J. and Kita, Y. (2015). Classification of the category of clothing item after bringing it into limited shapes. In *IEEE-RAS Int. Conf. on Humanoid Robots (Humanoids)*, pages 588–594.

[Hu et al., 2018] Hu, Z., Sun, P., and Pan, J. (2018). Three-dimensional deformable object manipulation using fast online gaussian process regression. *IEEE Robotics and Automation Letters*, 3(2):979–986.

[Hughes et al., 2005] Hughes, T. J., Cottrell, J. A., and Bazilevs, Y. (2005). Isogeometric analysis: CAD, finite elements, NURBS, exact geometry and mesh refinement. *Computer methods in applied mechanics and engineering*, 194(39):4135–4195.

[Hughes et al., 2010] Hughes, T. J., Reali, A., and Sangalli, G. (2010). Efficient quadrature for nurbs-based isogeometric analysis. *Computer methods in applied mechanics and engineering*, 199(5):301–313.

[Jiménez, 2017] Jiménez, P. (2017). Visual grasp point localization, classification and state recognition in robotic manipulation of cloth: An overview. *Robotics and Autonomous Systems*, 92(Supplement C):107 – 125.

[Kaldor, 2011] Kaldor, J. M. (2011). *Simulating Yarn-Based Cloth*. PhD thesis, Cornell University.

[Kaldor et al., 2008] Kaldor, J. M., James, D. L., and Marschner, S. (2008). Simulating knitted cloth at the yarn level. *ACM Transactions on Graphics (TOG)*, 27(3):65.

[Kaldor et al., 2010] Kaldor, J. M., James, D. L., and Marschner, S. (2010). Efficient yarn-based cloth with adaptive contact linearization. *ACM Transactions on Graphics (TOG)*, 29(4):105.

[Kaufmann, 2013] Kaufmann, P. (2013). *Discontinuous Galerkin FEM in Computer Graphics*. PhD thesis, ETH Zurich, Switzerland.

[Kaufmann et al., 2009] Kaufmann, P., Martin, S., Botsch, M., Grinspun, E., and Gross, M. (2009). Enrichment textures for detailed cutting of shells. *ACM Transactions on Graphics (TOG)*, 28(3):50.

[Kawabata et al., 1973] Kawabata, S., Niwa, M., and Kawai, H. (1973). The finite-deformation theory of plain-weave fabrics part i: The biaxial-deformation theory. *J. Textile Institute*, 64(1):21–46.

[Kiendl et al., 2009] Kiendl, J., Bletzinger, K.-U., Linhard, J., and Wüchner, R. (2009). Isogeometric shell analysis with Kirchhoff–Love elements. *Computer Methods in Applied Mechanics and Engineering*, 198(49):3902–3914.

[Kiendl, 2011] Kiendl, J. M. (2011). *Isogeometric analysis and shape optimal design of shell structures*.

[Kierzenka and Shampine, 2008] Kierzenka, J. A. and Shampine, L. F. (2008). A bvp solver that controls residual and error. *J. Numer. Anal. Ind. Appl. Math (JNAIAM)*, pages 1–2.

[King et al., 2005] King, M., Jearanaisilawong, P., and Socrate, S. (2005). A continuum constitutive model for the mechanical behavior of woven fabrics. *Int. J. of Solids and Structures*, 42(13):3867–3896.

[Kita et al., 2011] Kita, Y., Kanehiro, F., Ueshiba, T., and Kita, N. (2011). Clothes handling based on recognition by strategic observation. In *IEEE-RAS Int. Conf. on Humanoid Robots (Humanoids)*, pages 53–58.

[Kita and Kita, 2002] Kita, Y. and Kita, N. (2002). A model-driven method of estimating the state of clothes for manipulating it. In *Proc. IEEE Workshop on Applications of Computer Vision (WACV)*, pages 63–69.

[Kita et al., 2010] Kita, Y., Neo, E. S., Ueshiba, T., and Kita, N. (2010). Clothes handling using visual recognition in cooperation with actions. In *Proc. Int. Conf. on Intelligent Robots and Systems (IROS)*, pages 2710–2715.

[Kita et al., 2004] Kita, Y., Saito, F., and Kita, N. (2004). A deformable model driven visual method for handling clothes. In *Proc. IEEE Int. Conf. on Robotics and Automation (ICRA)*, pages 3889–3895.

[Kita et al., 2009] Kita, Y., Ueshiba, T., Neo, E. S., and Kita, N. (2009). Clothes state recognition using 3D observed data. In *Proc. IEEE Int. Conf. on Robotics and Automation (ICRA)*, pages 1220–1225.

[Kopacka et al., 2012] Kopacka, J., Kolman, R., Gabriel, D., and Plešek, J. (2012). Frictionless contact of elastic bodies: Comparison of treatment in finite element analysis and isogeometric analysis. *Engineering Mechanics*, page 178.

[Li et al., 2014] Li, Y., Chen, C.-F., and Allen, P. K. (2014). Recognition of deformable object category and pose. In *Proc. IEEE Int. Conf. on Robotics and Automation (ICRA)*, pages 5558–5564.

[Li et al., 2016a] Li, Y., Hu, X., Xu, D., Yue, Y., Grinspun, E., and Allen, P. K. (2016a). Multi-sensor surface analysis for robotic ironing. In *Proc. IEEE Int. Conf. on Robotics and Automation (ICRA)*, pages 5670–5676.

[Li et al., 2016b] Li, Y., Wang, Y., Yue, Y., Xu, D., Case, M., Chang, S., Grinspun, E., and Allen, P. K. (2016b). Model-driven feed-forward prediction for manipulation of deformable objects. *CoRR*, abs/1607.04411.

[Li et al., 2015a] Li, Y., Xu, D., Yue, Y., Wang, Y., Chang, S.-F., Grinspun, E., and Allen, P. K. (2015a). Regrasping and unfolding of garments using predictive thin shell modeling. In *Proc. IEEE Int. Conf. on Robotics and Automation (ICRA)*, pages 1382–1388.

[Li et al., 2015b] Li, Y., Yue, Y., Xu, D., Grinspun, E., and Allen, P. K. (2015b). Folding deformable objects using predictive simulation and trajectory optimization. In *Proc. Int. Conf. on Intelligent Robots and Systems (IROS)*.

[Lu and Zheng, 2014] Lu, J. and Zheng, C. (2014). Dynamic cloth simulation by isogeometric analysis. *Computer Methods in Applied Mechanics and Engineering*, 268:475 – 493.

[Maitin-Shepard et al., 2010] Maitin-Shepard, J., Cusumano-Towner, M., Lei, J., and Abbeel, P. (2010). Cloth grasp point detection based on multiple-view geometric cues with application to robotic towel folding. In *Proc. IEEE Int. Conf. on Robotics and Automation (ICRA)*, pages 2308–2315.

[Man, 2006] Man, X. (2006). *A Mathematical and Computational Multiscale Clothing Modeling Framework*. PhD thesis, The University of Iowa.

[Miller et al., 2011] Miller, S., Fritz, M., Darrell, T., and Abbeel, P. (2011). Parametrized shape models for clothing. In *Proc. IEEE Int. Conf. on Robotics and Automation (ICRA)*, pages 4861–4868.

[Miller et al., 2012] Miller, S., van den Berg, J., Fritz, M., Darrell, T., Goldberg, K., and Abbeel, P. (2012). A geometric approach to robotic laundry folding. *Int. J. Robotics Research (IJRR)*, 31(2):249–267.

[Müller and Gross, 2004] Müller, M. and Gross, M. (2004). Interactive virtual materials. In *Proc. Graphics Interface*, pages 239–246.

[Noels, 2009] Noels, L. (2009). A discontinuous Galerkin formulation of nonlinear Kirchhoff–Love shells. *Int. J. Numerical Methods in Engineering*, 78(3):296–323.

[Noels and Radovitzky, 2008] Noels, L. and Radovitzky, R. (2008). A new discontinuous Galerkin method for Kirchhoff–Love shells. *Computer Methods in Applied Mechanics and Engineering*, 197(33):2901–2929.

[Oñate, 2013] Oñate, E. (2013). Thick/Thin plates. Reissner-Mindlin theory. In *Structural Analysis with the Finite Element Method Linear Statics: Vol. 2. Beams, Plates and Shells*, pages 291–381. Springer Netherlands, Dordrecht.

[Osawa et al., 2007] Osawa, F., Seki, H., and Kamiya, Y. (2007). Unfolding of massive laundry and classification types by dual manipulator. *J. Advanced and Intelligent Informatics (JACIII)*, 11(5):457–463.

[Parsons et al., 2013] Parsons, E. M., King, M. J., and Socrate, S. (2013). Modeling yarn slip in woven fabric at the continuum level: Simulations of ballistic impact. *J. Mechanics and Physics of Solids*, 61(1):265–292.

[Parsons et al., 2010] Parsons, E. M., Weerasooriya, T., Sarva, S., and Socrate, S. (2010). Impact of woven fabric: Experiments and mesostructure-based continuum-level simulations. *J. Mechanics and Physics of Solids*, 58(11):1995–2021.

[Peirce, 1937] Peirce, F. T. (1937). The geometry of cloth structure. *J. Textile Institute Trans.*, 28(3):T45–T96.

[Petrík et al., 2018] Petrík, V., Cmíral, J., Smutný, V., Krsek, P., and Hlaváč, V. (2018). Automatic Material Properties Estimation for the Physics-Based Robotic Garment Folding. In *Proc. Int. Conf. on Robotics and Automation (ICRA)*, Brisbane, Australia. (Accepted for publication).

[Petrík and Smutný, 2014] Petrík, V. and Smutný, V. (2014). Comparison of calibrations for the CloPeMa robot. Res. Rep. CTU–CMP–2014–01, Center for Machine Perception, K13133 FEE Czech Technical University, Prague, Czech Republic.

[Petrík et al., 2015] Petrík, V., Smutný, V., Krsek, P., and Hlaváč, V. (2015). Robotic Garment Folding: Precision Improvement and Workspace Enlargement. In *Annu. Conf. Towards Autonomous Robotic Systems (TAROS)*, pages 204–215, Liverpool, United Kingdom.

[Petrík et al., 2016a] Petrík, V., Smutný, V., Krsek, P., and Hlaváč, V. (2016a). Accuracy of Robotic Elastic Object Manipulation as a Function of Material Properties. In *Int. Workshop on Modelling and Simulation for Autonomous Systems (MESAS)*, pages 384–395, Rome, Italy.

[Petrík et al., 2016b] Petrík, V., Smutný, V., Krsek, P., and Hlaváč, V. (2016b). Physics-Based Model of Rectangular Garment for Robotic Folding. In *Proc. Int. Conf. on Intelligent Robots and Systems (IROS)*, pages 951–956, Daejeon, Korea.

[Petrík et al., 2017] Petrík, V., Smutný, V., Krsek, P., and Hlaváč, V. (2017). Single arm robotic garment folding path generation. *Advanced Robotics*, 31(24-24):1325–1337.

[Plaut, 2015] Plaut, R. H. (2015). Formulas to determine fabric bending rigidity from simple tests. *Textile Research Journal*, 85(8):884–894.

[Potluri et al., 2000] Potluri, P., Ariadurai, S., and Whyte, I. (2000). A general theory for the deformation behaviour of non-plain-weave fabrics under biaxial loading. *J. Textile Institute*, 91(4):493–508.

[Ramisa et al., 2012] Ramisa, A., Alenya, G., Moreno-Noguer, F., and Torras, C. (2012). Using depth and appearance features for informed robot grasping of highly wrinkled clothes. In *Proc. IEEE Int. Conf. on Robotics and Automation (ICRA)*, pages 1703–1708.

[Rasheed et al., 2017] Rasheed, T., Khan, A. A., and Iqbal, J. (2017). Feature extraction of garments based on gaussian mixture for autonomous robotic manipulation. In *2017 First International Conference on Latest trends in Electrical Engineering and Computing Technologies (INTELLECT)*, pages 1–6.

[Šika et al., 2013] Šika, Z., Beneš, P., Valášek, M., Smutný, V., Petrík, V., and Krsek, P. (2013). Calibration research of Robots within CloPeMa Project using RedCaM Arm. Research report, Czech Technical University in Prague.

[Simo and Fox, 1989] Simo, J. C. and Fox, D. D. (1989). On a stress resultant geometrically exact shell model. Part I: formulation and optimal parametrization. *Computer Methods in Applied Mechanics and Engineering*, 72(3):267–304.

[Simo et al., 1989] Simo, J. C., Fox, D. D., and Rifai, M. S. (1989). On a stress resultant geometrically exact shell model. Part II: the linear theory; computational aspects. *Computer Methods in Applied Mechanics and Engineering*, 73(1):53–92.

[Simo et al., 1990] Simo, J. C., Fox, D. D., and Rifai, M. S. (1990). On a stress resultant geometrically exact shell model. Part III: computational aspects of the nonlinear theory. *Computer Methods in Applied Mechanics and Engineering*, 79(1):21–70.

[Sochi, 2016] Sochi, T. (2016). Principles of Differential Geometry. *ArXiv e-prints*.

[Stria et al., 2017] Stria, J., Petrík, V., and Hlaváč, V. (2017). Model-free Approach to Garments Unfolding Based on Detection of Folded Layers. In *Proc. Int. Conf. on Intelligent Robots and Systems (IROS)*, pages 3274–3280, Vancouver, Canada.

[Stria et al., 2014] Stria, J., Průša, D., Hlaváč, V., Wagner, L., Petrík, V., Krsek, P., and Smutný, V. (2014). Garment perception and its folding using a dual-arm robot. In *Proc. Int. Conf. on Intelligent Robots and Systems (IROS)*, pages 61–67, Chicago, Illinois.

[Stuart, 1966] Stuart, I. (1966). A loop test for bending length and rigidity. *British Journal of Applied Physics*, 17(9):1215.

[Sun et al., 2013] Sun, L., Aragon-Camarasa, G., Cockshott, P., Rogers, S., and Siebert, J. P. (2013). A Heuristic-Based Approach for Flattening Wrinkled Clothes. In *Annu. Conf. Towards Autonomous Robotic Systems (TAROS)*, pages 148–160.

[Sun et al., 2015] Sun, L., Aragon-Camarasa, G., Rogers, S., and Siebert, J. P. (2015). Accurate garment surface analysis using an active stereo robot head with application to dual-arm flattening. In *Proc. IEEE Int. Conf. on Robotics and Automation (ICRA)*, pages 185–192.

[Sun et al., 2017] Sun, L., Aragon-Camarasa, G., Rogers, S., Stolkin, R., and Siebert, J. P. (2017). Single-shot clothing category recognition in free-configurations with application to autonomous clothes sorting. In *Proc. Int. Conf. on Intelligent Robots and Systems (IROS)*.

[Sun et al., 2016a] Sun, L., Rogers, S., Aragon-Camarasa, G., and Siebert, J. P. (2016a). Recognising the clothing categories from free-configuration using gaussian-process-based interactive perception. In *Proc. IEEE Int. Conf. on Robotics and Automation (ICRA)*, pages 2464–2470.

[Sun et al., 2016b] Sun, L., Rogers, S., Aragon-Camarasa, G., and Siebert, J. P. (2016b). Recognising the clothing categories from free-configuration using gaussian-process-based interactive perception. In *2016 IEEE International Conference on Robotics and Automation (ICRA)*, pages 2464–2470.

[Thomaszewski et al., 2006] Thomaszewski, B., Wacker, M., and Straßer, W. (2006). A consistent bending model for cloth simulation with corotational subdivision finite elements. In *Proc. ACM SIGGRAPH/Eurographics Symp. on Computer Animation*, pages 107–116.

[Thuy-Hong-Loan Le et al., 2013] Thuy-Hong-Loan Le, M. J., Landini, A., Zoppi, M., Zlatanov, D., and Molfino, R. (2013). On the development of a specialized flexible gripper for garment handling. *J. Automation and Control Engineering*, 1(3).

[Timoshenko, 1953] Timoshenko, S. (1953). *History of strength of materials*. McGraw-Hill, New York.

[Triantafyllou et al., 2016] Triantafyllou, D., Mariolis, I., Kargakos, A., Malassiotis, S., and Aspragathos, N. (2016). A geometric approach to robotic unfolding of garments. *Robotics and Autonomous Systems*, 75:233 – 243.

[Twardon and Ritter, 2015] Twardon, L. and Ritter, H. (2015). Interaction skills for a coat-check robot: Identifying and handling the boundary components of clothes. In *2015 IEEE International Conference on Robotics and Automation (ICRA)*, pages 3682–3688.

[Twardon and Ritter, 2016] Twardon, L. and Ritter, H. (2016). Active boundary component models for robotic dressing assistance. In *2016 IEEE/RSJ International Conference on Intelligent Robots and Systems (IROS)*, pages 2811–2818.

[van den Berg et al., 2010] van den Berg, J., Miller, S., Goldberg, K. Y., and Abbeel, P. (2010). Gravity-based robotic cloth folding. In *Int. Workshop on the Algorithmic Foundations of Robotics (WAFR)*, pages 409–424.

[Vonásek et al., 2012] Vonásek, V., Kulich, M., Krajník, T., Saska, M., Fišer, D., Petrík, V., and Přeučil, L. (2012). Techniques for Modeling Simulation Environments for Modular Robotics. In *Proc. Int. Conf. on Mathematical Modelling*, pages 1–6, Vienna.

[Wang et al., 2010] Wang, L.-z., Yuan, F., Guo, Z., and Li, L.-l. (2010). Numerical analysis of pipeline in j-lay problem. *Journal of Zhejiang University SCIENCE A*, 11(11):908–920.

[Williams, 2010] Williams, R. W. (2010). *Measuring and modeling the anisotropic, nonlinear and hysteretic behavior of woven fabrics.* PhD thesis, University of Iowa.

[Willimon et al., 2011] Willimon, B., Birchfield, S., and Walker, I. (2011). Model for unfolding laundry using interactive perception. In *Proc. Int. Conf. on Intelligent Robots and Systems (IROS)*, pages 4871–4876.

[Yamakawa et al., 2010] Yamakawa, Y., Namiki, A., and Ishikawa, M. (2010). Dynamic folding of a cloth by two high-speed multifingered hands. In *2010 JSME Conference on Robotics and Mechatronics*, volume 2.

[Yamakawa et al., 2011a] Yamakawa, Y., Namiki, A., and Ishikawa, M. (2011a). Dynamic manipulation of a cloth by high-speed robot system using high-speed visual feedback. *IFAC Proceedings Volumes*, 44(1):8076–8081.

[Yamakawa et al., 2011b] Yamakawa, Y., Namiki, A., and Ishikawa, M. (2011b). Motion planning for dynamic folding of a cloth with two high-speed robot hands and two high-speed sliders. In *Robotics and Automation (ICRA), 2011 IEEE International Conference on*, pages 5486–5491. IEEE.

[Yuba et al., 2015] Yuba, H., Arnold, S., and Yamazaki, K. (2015). Unfolding of a rectangular cloth based on action selection depending on recognition uncertainty. In *IEEE/SICE Int. Symp. on System Integration (SII)*, pages 623–628.

[Yuba et al., 2017] Yuba, H., Arnold, S., and Yamazaki, K. (2017). Unfolding of a rectangular cloth from unarranged starting shapes by a dual-armed robot with a mechanism for managing recognition error and uncertainty. *Advanced Robotics*, 31(10):544–556.

[Zeng et al., 2006] Zeng, X., Tan, V., and Shim, V. (2006). Modelling inter-yarn friction in woven fabric armour. *Int. J. Numerical Methods in Engineering*, 66(8):1309–1330.

[Zeng et al., 2014] Zeng, X.-G., Duan, M.-L., and An, C. (2014). Mathematical model of pipeline abandonment and recovery in deepwater. *Journal of Applied Mathematics*, 2014.

[Zheng, 2013] Zheng, C. (2013). *Cloth simulation by isogeometric analysis.* PhD thesis, University of Iowa.

Appendix A
Author's Publications

A.1 Publications Related to the Thesis

A.1.1 Impacted Journal Articles

- Petrík, V., Smutný, V., Krsek, P., and Hlaváč, V. (2017). Single arm robotic garment folding path generation. *Advanced Robotics*, 31(24-24):1325–1337.
[**25%**-25%-25%-25%]

A.1.2 Publications Excerpted by WOS

- Petrík, V., Smutný, V., Krsek, P., and Hlaváč, V. (2015). Robotic Garment Folding: Precision Improvement and Workspace Enlargement. In *Annu. Conf. Towards Autonomous Robotic Systems (TAROS)*, pages 204–215, Liverpool, United Kingdom.
[**70%**-10%-10%-10%]
- Petrík, V., Smutný, V., Krsek, P., and Hlaváč, V. (2016b). Physics-Based Model of Rectangular Garment for Robotic Folding. In *Proc. Int. Conf. on Intelligent Robots and Systems (IROS)*, pages 951–956, Daejeon, Korea.
[**25%**-25%-25%-25%]
- Petrík, V., Smutný, V., Krsek, P., and Hlaváč, V. (2016a). Accuracy of Robotic Elastic Object Manipulation as a Function of Material Properties. In *Int. Workshop on Modelling and Simulation for Autonomous Systems (MESAS)*, pages 384–395, Rome, Italy.
[**55%**-15%-15%-15%]

A.1.3 Other conference publications

- Petrík, V., Cmíral, J., Smutný, V., Krsek, P., and Hlaváč, V. (2018). Automatic Material Properties Estimation for the Physics-Based Robotic Garment Folding. In *Proc. Int. Conf. on Robotics and Automation*

(ICRA), Brisbane, Australia. (Accepted for publication).
[**20%**-20%-20%-20%-20%]

A.2 Additional Publications

A.2.1 Impacted Journal Articles

- Doumanoglou, A., Stria, J., Peleka, G., Mariolis, I., Petrík, V., Kargakos, A., Wagner, L., Hlaváč, V., Kim, T.-K., and Malassiotis, S. (2016). Folding Clothes Autonomously: A Complete Pipeline. *IEEE Transactions on Robotics*, 32(6):1461–1478.
[20%-20%-10%-10%-**10%**-9%-9%-4%-4%-4%]

A.2.2 Publications Excerpted by WOS

- Stria, J., Průša, D., Hlaváč, V., Wagner, L., Petrík, V., Krsek, P., and Smutný, V. (2014). Garment perception and its folding using a dual-arm robot. In *Proc. Int. Conf. on Intelligent Robots and Systems (IROS)*, pages 61–67, Chicago, Illinois.
[50%-10%-10%-10%-**10%**-5%-5%]

A.2.3 Other conference publications

- Stria, J., Petrík, V., and Hlaváč, V. (2017). Model-free Approach to Garments Unfolding Based on Detection of Folded Layers. In *Proc. Int. Conf. on Intelligent Robots and Systems (IROS)*, pages 3274–3280, Vancouver, Canada.
[60%-**20%**-20%]
- Vonásek, V., Kulich, M., Krajník, T., Saska, M., Fišer, D., Petrík, V., and Přeučil, L. (2012). Techniques for Modeling Simulation Environments for Modular Robotics. In *Proc. Int. Conf. on Mathematical Modelling*, pages 1–6, Vienna.
[28%-12%-12%-12%-12%-**12%**-12%]

Appendix B

Citations of Author's Work

- Doumanoglou, A., Stria, J., Peleka, G., Mariolis, I., Petrík, V., Kargakos, A., Wagner, L., Hlaváč, V., Kim, T.-K., and Malassiotis, S. (2016). Folding Clothes Autonomously: A Complete Pipeline. *IEEE Transactions on Robotics*, 32(6):1461–1478
    - Hu, Z., Sun, P., and Pan, J. (2018). Three-dimensional deformable object manipulation using fast online gaussian process regression. *IEEE Robotics and Automation Letters*, 3(2):979–986
    - Corona, E., Alenyà, G., Gabas, A., and Torras, C. (2017). Active garment recognition and target grasping point detection using deep learning. *Pattern Recognition*
- Stria, J., Průša, D., Hlaváč, V., Wagner, L., Petrík, V., Krsek, P., and Smutný, V. (2014). Garment perception and its folding using a dual-arm robot. In *Proc. Int. Conf. on Intelligent Robots and Systems (IROS)*, pages 61–67, Chicago, Illinois
    - Hou, Y. C., Sahari, K. S. M., Weng, L. Y., How, D. N. T., and Seki, H. (2017). Particle-based perception of garment folding for robotic manipulation purposes. *International Journal of Advanced Robotic Systems*, 14(6):1729881417738727
    - Jiménez, P. (2017). Visual grasp point localization, classification and state recognition in robotic manipulation of cloth: An overview. *Robotics and Autonomous Systems*, 92(Supplement C):107 – 125
    - Rasheed, T., Khan, A. A., and Iqbal, J. (2017). Feature extraction of garments based on gaussian mixture for autonomous robotic manipulation. In *2017 First International Conference on Latest trends in Electrical Engineering and Computing Technologies (INTELLECT)*, pages 1–6
    - Drigalski, F. V., Yoshioka, D., Yamazaki, W., Cho, S. G., Gall, M., Eljuri, P. M. U., Hoerig, V., Ding, M., Takamatsu, J., Ogasawara, T., and Beltran, J. (2017). Naist openhand m2s: A versatile two-finger gripper adapted for pulling and tucking textile. In *2017 First IEEE International Conference on Robotic Computing (IRC)*, pages 117–122

- Cockshott, P. and Renaud, K. (2016). Humans, robots and values. *Technology in Society*, 45:19 – 28
- Sun, L., Rogers, S., Aragon-Camarasa, G., and Siebert, J. P. (2016b). Recognising the clothing categories from free-configuration using gaussian-process-based interactive perception. In *2016 IEEE International Conference on Robotics and Automation (ICRA)*, pages 2464–2470
- Estevez, D., Victores, J. G., Morante, S., and Balaguer, C. (2016). Towards robotic garment folding: A vision approach for fold detection. In *2016 International Conference on Autonomous Robot Systems and Competitions (ICARSC)*, pages 188–192
- Twardon, L. and Ritter, H. (2016). Active boundary component models for robotic dressing assistance. In *2016 IEEE/RSJ International Conference on Intelligent Robots and Systems (IROS)*, pages 2811–2818
- Sun, L., Aragon-Camarasa, G., Rogers, S., and Siebert, J. P. (2015). Accurate garment surface analysis using an active stereo robot head with application to dual-arm flattening. In *Proc. IEEE Int. Conf. on Robotics and Automation (ICRA)*, pages 185–192
- Twardon, L. and Ritter, H. (2015). Interaction skills for a coat-check robot: Identifying and handling the boundary components of clothes. In *2015 IEEE International Conference on Robotics and Automation (ICRA)*, pages 3682–3688